



Australian Government
Bureau of Meteorology

The Centre for Australian Weather and Climate Research
A partnership between CSIRO and the Bureau of Meteorology



Development of the Sun-Edwards-Slingo radiation scheme (SES2)

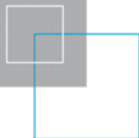
CAWCR Technical Report No. 009

Zhian Sun

December 2008



www.cawcr.gov.au



Development of the Sun-Edwards-Slingo radiation scheme (SES2)

CAWCR Technical Report No. 009

Zhian Sun

Centre for Australian Weather and Climate Research, Australian Bureau of
Meteorology, GPO Box 1289, Melbourne Victoria 3001, Australia.

Enquiries should be addressed to:

Zhian Sun

Centre for Australian Weather and Climate Research:

A Partnership between the Bureau of Meteorology and CSIRO

GPO Box 1289K, Melbourne

Victoria 3001, Australia

z.sun@bom.gov.au

ISSN: 1836-019X

ISBN: 978-1-921424-88-5

Series: Technical report (Centre for Australian Weather and Climate
Research.) ; no. 9.

Also issued in print.

Copyright and Disclaimer

© 2008 CSIRO and the Bureau of Meteorology. To the extent permitted by law, all rights are reserved and no part of this publication covered by copyright may be reproduced or copied in any form or by any means except with the written permission of CSIRO and the Bureau of Meteorology.

CSIRO and the Bureau of Meteorology advise that the information contained in this publication comprises general statements based on scientific research. The reader is advised and needs to be aware that such information may be incomplete or unable to be used in any specific situation. No reliance or actions must therefore be made on that information without seeking prior expert professional, scientific and technical advice. To the extent permitted by law, CSIRO and the Bureau of Meteorology (including each of its employees and consultants) excludes all liability to any person for any consequences, including but not limited to all losses, damages, costs, expenses and any other compensation, arising directly or indirectly from using this publication (in part or in whole) and any information or material contained in it.

Contents

Abstract	1
1. Introduction	2
2. Correlated-k method	3
3. Development strategy.....	8
4. Modifications of GENLN2 and its validation	9
5. Implementation of new absorption data in GenIn2	14
5.1 Ozone data	14
5.2 Molecular oxygen collision induced continuum absorption	18
5.3 Cross-section data of SO ₂ in UV band.....	21
5.4 Cross-section of NO ₂ data	22
6. Solar source function	24
7. Line-by-line calculations of heating rates for important absorbing species	26
8. Correlated k-distribution developed for SES2	32
9. Treatment of gaseous overlapping absorption.....	37
10. Treatments of other quantities in CKD model	39
10.1 Minor species.....	39
10.2 Water vapour continuum	39
10.3 Planck function	40
10.4 Oxygen collision induced continuum.....	40
10.5 Solar source function	40
10.6 Treatment of overlapping absorption of the solar and infrared.....	41
11. Comparisons of SES2 with GENLN2, SES1 and UKMO ES schemes	42
12. Fast scheme for surface radiation budget (SURFLX).....	46
13. Evaluations of SES2 in BMRC Atmospheric Model (BAM).....	47
13.1 Comparison of radiation fields with satellite measurements.....	47
13.2 Ten year AGCM integration	50
13.2.1 Cloud radiative forcing.....	51
13.2.2 Precipitation	59
13.2.3 Zonal mean temperature	59
14. Conclusions	68
References.....	70

List of Figures

Figure 1. Absorption coefficients of water vapour as a function of cumulative probability g for three pressures determined using two sorting methods. The left panel shows the results derived by reordering the absorption spectrum at all three levels. The right panel displays the results determined by reordering the spectrum at 1mb level and then applying this sorting to other two levels.	6
Figure 2. Longwave heating rate errors due to correlated k assumption calculated at line-by-line spectral resolution using SES1 two stream radiative transfer scheme. The calculations are performed for the spectral region $350 - 400 \text{ cm}^{-1}$. The left panel shows the average heating error across the band.	7
Figure 3. Development strategies of radiation schemes.	10
Figure 4. Longwave cooling rates determined using GENLN2 and LBLRTM for three ICRCM test cases: (a) H_2O only; (b) $\text{H}_2\text{O} + \text{continuum}$; (c) $\text{H}_2\text{O} + \text{CO}_2 + \text{O}_3$	10
Figure 5. shortwave heating rates due to absorption by water vapour determined using GENLN2 and GFDL for MLS atmosphere. The calculations assume three solar zenith angles as indicated in the figure and a surface albedo of 0.8.	12
Figure 6. Comparison of measured (red curve) and calculated (green) solar spectral irradiances for a clear sky condition at ARM SGP site on 4 March 2000. Lower panel shows the differences.	13
Figure 7. Comparison of three ozone absorption cross-section datasets. Both the ESA and Malicet results represent the cross-section at a constant temperature of 246 K while the results from Lowtran denote values for averaged temperature. The right panel shows the results in the spectral region 0.5 - 0.7 microns in linear scale to emphasize the differences.	15
Figure 8. The upper panel shows the downward spectral solar irradiances at surface determined using the three O_3 absorption cross-section datasets. The differences (ESA minus Malicet and Lowtran) are displayed in the lower panel. The calculations assume a mid-latitude summer atmosphere, a solar zenith angle of 30° and a surface albedo of 0.2.	16
Figure 9. Solar heating rate in the UV and visible region due to O_3 absorption determined using three absorption cross-section datasets (left panel). The differences (ESA minus Malicet and Lowtran) are shown in the right panel. The calculations assume a mid-latitude summer atmosphere, a solar zenith angle of 30° and a surface albedo of 0.2.	17
Figure 10. Ozone absorption cross-sections as a function of wavelength for five temperatures. The data were obtained from European Space Agency website.	18
Figure 11. Binary cross-section for the absorption continuum in the 1.59 (A), 1.27 (B) and 1.06 (C) μm bands of oxygen for different temperatures derived by Smith and Newnham (2000).	20
Figure 12. Solar irradiances calculated by GENLN2 for the cases with and without oxygen collision induced continuum. Three absorbing gases (H_2O , O_3 and O_2) are included in the calculations with a solar zenith angle of 60° and a surface albedo of 0.1. The lower panel shows difference, i.e. the result without O_4 (red curve) minus that with O_4 (green curve) ..	21

Figure 13. The atmospheric heating rates due to shortwave absorption by water vapour, ozone and oxygen for a clear-sky mid-latitude summer profiles, solar zenith angle of 60° , surface albedo 0.1. The oxygen collision-induced absorption is included in both models and the Rayleigh scattering is included in the SES2 model.	21
Figure 14. Measured sulphur dioxide cross-section in the ultra-violet spectrum. The data are obtained from ESA website.....	23
Figure 15. Measured nitrogen dioxide cross-sections. The data were obtained from ESA website	23
Figure 16. Comparison of different version of the Kurucz solar source functions with that of Labs and Neckel. The lower panel shows the difference between Kurucz 1992 version and that used in AER and UK Met Office.	24
Figure 17. Percentage change in the solar energy in three major solar spectral bands due to the change from the Labs and Neckel solar source function to Kurucz source function.	25
Figure 18. Solar heating rates determined by GENLN2 for 4 solar source functions.....	26
Figure 19. Spectral cooling rate profile for water vapour (no continuum) as a function of pressure of midlatitude summer atmosphere. The upper panel uses a linear scale to emphasize results in the troposphere and the lower panel uses a logarithmic scale to emphasize the results in upper atmosphere. Color scale $\times 10^{-3}$ is in unit of $\text{K day}^{-1} (10 \text{ cm}^{-1})^{-1}$	27
Figure 20. Spectral cooling rate profile for water vapour including self continuum (upper panel) and self-continuum only (lower panel) as a function of pressure for midlatitude summer atmosphere. The color scale $\times 10^{-3}$ is in unit of $\text{K day}^{-1} (10 \text{ cm}^{-1})^{-1}$	28
Figure 21. Shortwave spectral heating rate profile for water vapour as a function of pressure for MLS atmosphere. Color scale $\times 10^{-3}$ is in unit of $\text{K day}^{-1} (10 \text{ cm}^{-1})^{-1}$	29
Figure 22. Shortwave spectral heating profiles for (a) carbon dioxide, (b) methane, (c) nitrous monoxide, (d) oxygen and (e) ozone.	29
Figure 23. Absorption coefficients in each g interval determined using the five methods. The solid curve represents the values at the line-by-line grids and the symbols denote those using 10 g points.	33
Figure 24. Downward irradiances above 100 mb determined using the LBL and SES2 with 4 methods of determinations of absorption coefficients. The calculations use MLS atmosphere with 60 layers. The legend 'sp' means a pressure scaling to the last k term above 3.5 mb.	34
Figure 25. Longwave heating rates (left) and errors (right) determined using LBL code and SES2 with 4 methods of determinations of the absorption coefficients. representative k value in that interval.	35
Figure 26. Comparison of net flux determined for $28750\text{-}50000\text{cm}^{-1}$ using 5 k term with those using 145 k term. The thick curves represent the results from 5 k terms while the thin lines denote those from 145 k term. The left panel shows results determined using method of ESFT and right panel gives the results from fit method. The right most curves show the total band fluxes.	36
Figure 27. Longwave heating profiles determined by GENLN2 and two CKD models: one using 145 g intervals and one using 4 g intervals.	37

Figure 28. The left two panels show the longwave heating rates and difference with and without solar source at the top of the atmosphere. The right panels show the heating rate and difference with and without adding solar tail flux to the last near infrared band.	41
Figure 29. Comparison of radiative heating/cooling rates determined by LBL and SES2 radiation schemes for three atmospheres. The shortwave calculations assume a solar zenith angle of 30° and a surface albedo of 0.2. The left panels show heating/cooling from LBL calculations and the right panels show the errors of SES2 relative to LBL.	43
Figure 30. Comparison of the shortwave results determined using the SES2 with those from the LBL and SES1 for mid-latitude summer atmosphere. The calculations assume a solar zenith angle of 30° and a surface albedo of 0.2.	44
Figure 31. Comparison of shortwave results determined by LBL, SES2 and Edwards-Slingo radiation schemes. The calculations use MLS atmosphere with a solar zenith angle of 30° and surface albedo of 0.2.	45
Figure 32. Comparison of longwave radiative results determined by LBL, SES2 and Edwards-Slingo schemes for MLS atmosphere.	46
Figure 33. Clear sky reflected shortwave flux at the top of atmosphere determined by CERES satellite and BAM model for January 2001. Top left panel: CERES; top right panel: FS; bottom left panel: SES1; bottom right: SES2.	48
Figure 34. Clear-sky OLR determined by CERES satellite and Bam model for January 2001. Top left panel: CERES; top right panel: FS; bottom left panel: SES1; bottom right: SES2.	49
Figure 35. All-sky reflected shortwave flux at TOA determined by CERES satellite and BAM model for January 2001. Top left panel: CERES; top right panel: FS; bottom left panel: SES1; bottom right: SES2.	50
Figure 36. All-sky OLR determined by CERES satellite and BAM model for January 2001. Top left panel: CERES; top right panel: FS; bottom left panel: SES1; bottom right: SES2.	51
Figure 37. Comparisons of the ERBE and SES2 for zonal mean cloud longwave forcing (top panel), shortwave forcing (middle panel) and total forcing (low panel) in January.	53
Figure 38. Same as figure 37 but for July.	54
Figure 39. Horizontal distribution of cloud longwave forcing determined by ERBE and BAM model in January.	55
Figure 40. As for figure 39, but for July.	56
Figure 41. Horizontal distribution of cloud shortwave forcing determined by ERBE and Bam model in January.	57
Figure 42. As for figure 41 but for July.	58
Figure 43. January precipitation for (a) model, (b) observations, (c) model minus observations and (d) zonal mean of model and observations. Units: mm/day	60
Figure 44. As for figure 43, but for July.	61
Figure 45. January, zonal mean temperature for: (a) model, (b) NCEP, and (c) model minus NCEP. Units: °C.	62

Figure 46. Same as figure 45, but for July	63
Figure 47. Verification of MSLP in tropics. Red curve is from the control run; green is from SES2 with cld93 scheme and blue is from the SES2 with prognostic cloud scheme;	64
Figure 48. As for figure 47, but for 850 hPa geopotential height of Southern Annulus.	65
Figure 49. As for figure 47 but for 500 hPa geopotential height of Northern Annulus.....	66
Figure 50. As figure 47 but for 100 hPa geopotential height of Australia	67
Figure 51. As for figure 47 but for 50 hPa geopotential height of tropics	68

List of Tables

Table 1. Division of spectral bands, absorbing species and number of k terms in each band ...	31
---	----

ABSTRACT

This report documents the research and development of radiation studies carried out at the former BMRC. Only unpublished results are included in the report. The main focus is on the work performed to improve the line-by-line radiative transfer model and the development of the second version of the Sun-Edwards-Slingo scheme (SES2).

The GENLN2 line-by-line model, imported from NCAR has been significantly modified for its capability of generating the spectral information necessary for developing a broad-band radiation code and serving as a benchmark for validation of a broad-band model.

A new version of the Edwards-Slingo scheme (SES2) is developed using a new k-distribution method and a new method to deal with the gaseous overlapping absorption in a spectral band. These new techniques make the SES2 more accurate yet efficient. The number of spectral bands and number of absorbing species are both increased for better resolution of the spectral variation of absorbing species, aerosols and clouds, but the computational cost is reduced substantially compared with the previous version of the code.

In addition, a fast scheme for determining the global and net solar radiation at the surface is developed. The work for clear sky conditions has been completed. Inclusion of the effects of clouds and aerosols is still in progress. The purpose for developing such a scheme is to improve the model land surface processes.

In line with the above work, a set of software is developed which can be used for developing a range of radiation schemes for different applications.

1. INTRODUCTION

The SES2 scheme has been developed for application to numerical weather prediction (NWP) and climate models. The purpose in developing SES2 has been to obtain an accurate treatment for molecular gaseous absorptions, Rayleigh and aerosol scattering and include more absorbing species, especially those important for climate applications. SES2 is based on a radiation scheme developed by Edward and Slingo (Edward and Slingo, 1996). The Edward and Slingo scheme has some novel features that are not available in other schemes. The most important one is that it was designed to suit both applications involving reference calculations and weather prediction and climate studies. Therefore the spectral resolution of the code is flexible. This is achieved using a spectral file containing the necessary spectral information such as spectral band limit, absorbing species, and spectral properties of atmospheric constituents required by the radiation code. The spectral file can be pre-built to suit code requirement. This facility enables the user to have a full control of the spectral resolution of the code and the physical processes involved. The second novel feature is that the spectral framework is the same for both the longwave and shortwave components. This makes the code easy to maintain and develop. All these features have been maintained in SES2. In addition, SES2 utilizes the correlated-k method (Lacis and Oinas, 1991 ; Fu and Liou, 1992 ; Mlawer et al., 1997) which is similar to the method of Exponential Sum Fit Transmission (ESFT) used in the first version of SES model (SES1). The correlated-k and ESFT both have advantages of computational efficiency and direct adaptability to multiple-scattering calculations. SES2 development has been based on the line-by-line radiative transfer model (GENLN2) (Edwards, 1992), which provides the absorption coefficients for the relevant k distributions. The accuracy of these absorption coefficients has been established by comparison of GENLN2 with other line-by-line models such as LBLRTM (Clough et al., 1992) and measurements from the Atmospheric Radiation Measurement (ARM) (Stokes and Schwartz, 1994). These validations show with high confidence that GENLN2 is accurate enough for use as the foundation for development of SES2.

In SES2, absorption due to water vapour, carbon dioxide, ozone, methane, nitrous oxide, oxygen, CFC11, CFC12, CFC113, and CFC114 is considered. Other species can be easily implemented into the scheme using interface software developed in this study. Accurate calculation of the radiative effect of these gases requires the spectral regions to be divided into a series of spectral bands, each of which contains strong absorption bands of a limited number of gases. The division of these spectral bands was carefully designed to properly resolve the important spectral absorption signatures of these gases.

The radiative flux and heating/cooling rates determined by SES2 are validated against the same quantities obtained directly from GENLN2. This enables the critical evaluation of the results of the model for each of its spectral bands for a wide range of atmospheric conditions. It is important in evaluating a radiative transfer model to consider not only the flux and heating rate but also their sensitivity to variations in relevant physical quantities.

Based on SES2, a fast scheme for determining the global and net solar radiation at the surface (SURFLX) has also been developed. The reason for developing such a scheme is to enable the surface radiation budget calculation to be carried out at each model integration time step in order to improve the model land surface processes. The input variables to this scheme are total column values of absorbing gas amount, solar zenith angle, surface pressure and albedo. Wide ranges of these quantities have been used in SES2 calculations to cover the range of possible values found in the earth's atmosphere. The results at the surface determined by SES2 were used to develop SURFLX. All variables used in the SURFLX can be obtained from satellite measurements or field experiments and therefore it is easy to validate SURFLX against a wide range of observations. These validations provide a traceable link from SES2 and GENLN2 to observations for a wide range of atmospheric conditions.

In this report, the details of development in GENLN2 and SES2 are presented. The development of SURFLX has been published (Sun et al., 2007) so only a brief summary of that work is given. SES2 has been extensively tested against the Genln2 line-by-line results and earlier version as well as the original Edwards-Slingo radiation code. It has also been validated by comparing modeled radiation at the top of the atmosphere (TOA) with satellite observations. These comparisons are presented in this report. Finally, the performance of SES2 in the BMRC Atmospheric Model (BAM) is evaluated in both climate and NWP modes. The results are also discussed in the report.

2. CORRELATED-K METHOD

The correlated-k distribution (CKD) is an approximate technique for the accelerated calculation of radiation for inhomogeneous atmospheres. Because this method is capable of achieving accuracy comparable with that of line-by-line models with an extreme reduction in the number of radiative transfer calculations, it has been widely adopted in development of new radiative transfer schemes. This method allows the radiative transfer operations for a given homogeneous layer and spectral band to be carried out using a small set of absorption coefficients that are representative of the absorption coefficients for all frequencies in the band. The spectral absorption coefficient varies extremely irregularly with wavenumber and therefore it is hard to find a representative values in each sub-interval. However, by reordering the absorption coefficients in ascending order, the absorption spectrum becomes a smoothly varying function and a representative value can be specified for any segment of the re-ordered spectrum. Mathematically, this operation can be expressed as given below.

Assuming a uniform source of radiation over the frequency interval $\Delta\nu$, gaseous transmittance is given by

$$T(u) = \frac{1}{\Delta\nu} \int_{\Delta\nu} e^{-k(v)u} dv \quad (1)$$

where u is the gaseous absorber amount, and $k(\nu)$ is the gaseous absorption coefficient in frequency space. The absorption coefficient k is a function of pressure and temperature. The transmission function can also be written in k space (Goody and Yung 1989) as

$$T(u) = \frac{1}{\Delta\nu} \int_0^\infty e^{-ku} f(k) dk, \quad (2)$$

where $f(k)$ is the k -distribution function,

$$f(k) = \frac{1}{\Delta\nu} \int_{\Delta\nu} \delta[k - k(\nu)] d\nu, \quad (3)$$

where $\delta[k - k(\nu)]$ is the δ function. $f(k)$ is a Dirac comb (Li and Barker, 2005), because it sums up all absorption lines of the same strength. In (2) and (3), k is still the absorption coefficient, but it is now in k space and thus represents reordered values that are independent of ν . Note that expression for the transmission function in k space and frequency space are related to each other via,

$$\begin{aligned} T(u) &= \int_0^\infty e^{-ku} f(k) dk, \\ &= \int_0^\infty e^{-ku} \frac{1}{\Delta\nu} \int_{\Delta\nu} \delta[k - k(\nu)] d\nu dk, \\ &= \frac{1}{\Delta\nu} \int_{\Delta\nu} \int_0^\infty e^{-ku} \delta[k - k(\nu)] dk d\nu, \\ &= \frac{1}{\Delta\nu} \int_{\Delta\nu} e^{-k(\nu)u} d\nu. \end{aligned} \quad (4)$$

Now consider the cumulative probability function

$$g(k) = \int_0^k f(k') dk' \quad (5)$$

with $g(0) = 0$ and $g(\infty) = 1$. From (5), $dg(k) = f(k)dk$, which when inserted into (2) yields

$$T(u) = \int_0^1 e^{-k(g)u} dg \quad (6)$$

Thus, g forms a cumulative probability space (CPS), in which $k(g)$ is now the absorption coefficient in g space. Scaling CPS into N points G_i ($i = 0, 1, 2, \dots, N$), with $G_0 = 0$, $G_N = 1$, and letting

$g_i = G_i - G_{i-1}$, with $\sum_{i=1}^N g_i = 1$, the integral in (6) becomes

$$T(u) = \sum_{i=1}^N \int_{G_{i-1}}^{G_i} e^{-k(g)u} dg \quad (7)$$

Accurate results for each of the N intervals in (7) can be obtained from line-by-line calculations using all available k values in g space. On the other hand, the results in a k distribution model have to be calculated as

$$T(u) = \sum_{i=1}^N e^{-\langle k(g) \rangle u_i} g_i \quad (8)$$

For each domain g_i , the model absorption coefficient in CPS, $\langle k(g) \rangle$, could be obtained through fitting the line-by-line results of (7) in the same domain for a suitable range of u . The detailed procedure of this approach will be introduced in section 8.

For an inhomogeneous atmosphere, the layers with different pressure and temperature are treated in the same way as described above. Thus, a transmission function between two pressures p_1 and p_2 is given by

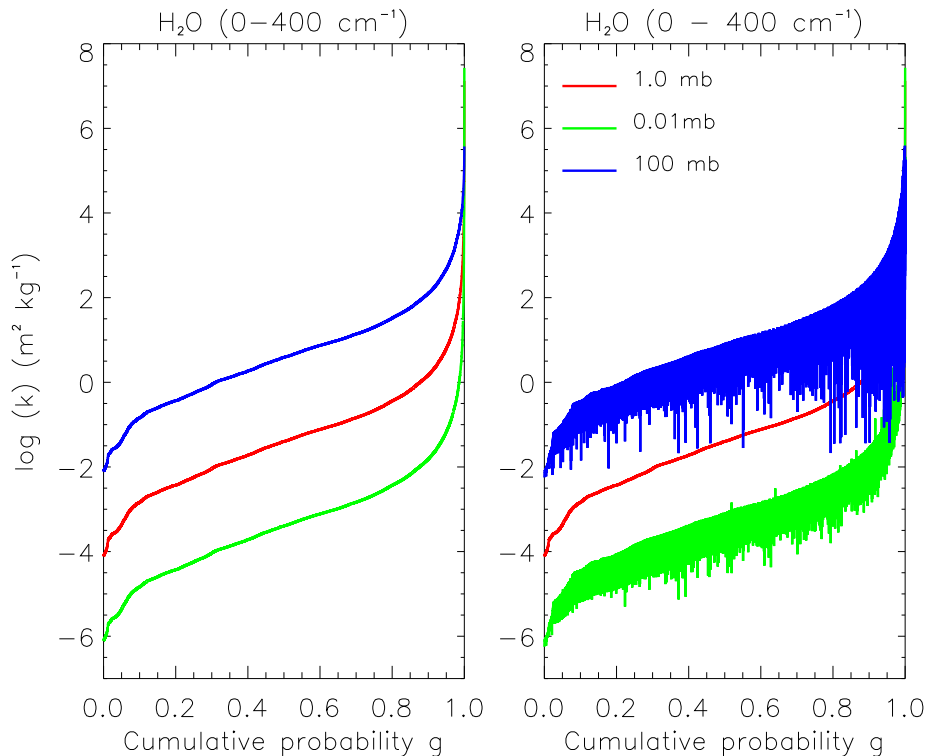
$$T = \sum_{i=1}^N \exp \left[- \int_{p_1}^{p_2} \langle k(g_i) \rangle q(p) \frac{dp}{G} \right] g_i, \quad (9)$$

where $q(p)$ is the mass mixing ratio for the absorber at pressure p , and G is the gravitational constant. This procedure is known as the correlated- k method. It is based on an assumption that the k distribution in a given layer is fully correlated in spectral space with the k distribution in the next layer. This assumption is true for a few special cases (Fu and Liou, 1992). In general, however these conditions do not hold. As pressure, temperature, and relative molecular concentrations change from one layer to another, each $k(\nu)$ value will be affected differently.

As a result, the spectral elements that contribute to a subinterval of the k distribution for one homogeneous layer will not be mapped to the corresponding subinterval for a different atmospheric layer, and therefore performing radiative transfer through the atmosphere for a single subinterval will not correspond to a fixed set of frequencies. This affects the accuracy of the radiance calculation since, for each layer, the transmittance that acts on the incoming radiance in general will not be perfectly matched with that radiance since the two quantities will be associated with different sets of spectral elements. The magnitude of the resulting error is dependent on the extent to which the mapping $\nu \rightarrow g$ for successive atmospheric layers is correlated.

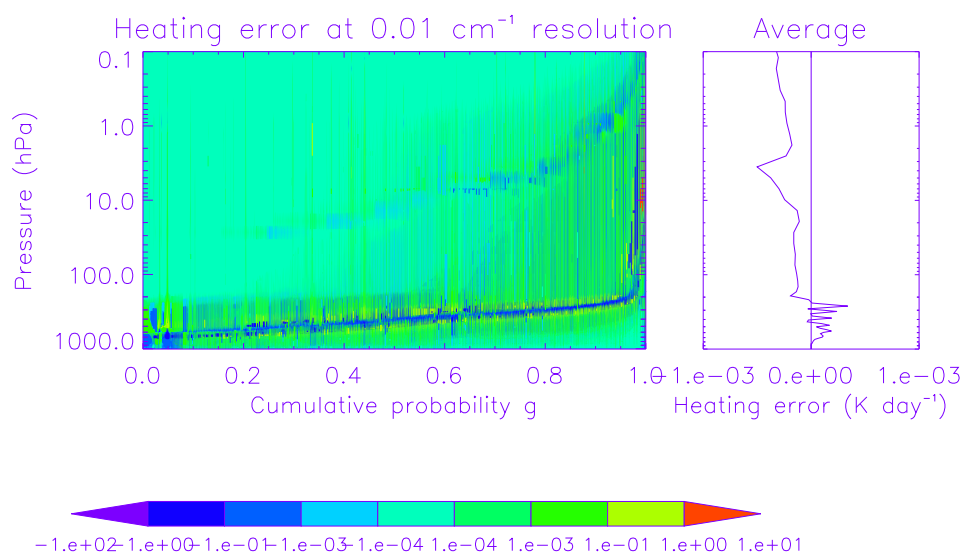
In general, the correlation in sorted absorption coefficients is very strong when two atmospheric layers are close and weak when two layers are too far away (Li and Barker, 2005). In the process of radiative transfer, influences from near-neighbor levels are much more important than from distant levels. For the infrared radiative transfer, all the exchange contributions from outside a layer are represented by the incoming flux at the layer's boundary and flux calculations precede individually layer-by-layer. Only transmissions between any two neighboring levels are needed. Thus, correlation in sorted absorption spectra in CPS is highly guaranteed. For solar radiation, the widely used adding-doubling method (Lacis and Hansen, 1974) also addresses reflection and transmission for each individual layer. These properties can then be linked to generate contiguous layers such that vertical correlation is maximized in the correlated-k method by individually sorting at each pressure level. This may explain the success of this method in radiative transfer calculations.

Figure 1. Absorption coefficients of water vapour as a function of cumulative probability g for three pressures determined using two sorting methods. The left panel shows the results derived by reordering the absorption spectrum at all three levels. The right panel displays the results determined by reordering the spectrum at 1 mb level and then applying this sorting to other two levels.



This issue is further investigated in this study. In Figure 1, we plot re-ordered water vapour absorption coefficients in the spectrum between 0 and 400 cm^{-1} in two ways: one is to perform the $\nu \rightarrow g$ mapping individually for three pressure levels as shown in the left panel; the other is to perform the mapping at a reference level of 1 hPa and apply this mapping to the other two levels. The results are shown in the right panel. Clearly, the results in the left panel are smooth and it is easy to perform the integration in g space, but the frequencies corresponding one g point at three levels in this case are usually not the same and that actually violates the vertical correlation principle. The results in the right panel are not smooth for the pressures 0.01 and 100 hPa but the frequencies at each g point are the same for all three levels. Clearly, it is hard to obtain an accurate integration result for the second case unless a high spectral resolution line-by-line model is used. This figure indicates that the correlation assumption for the absorption coefficients in inhomogeneous atmosphere does not hold. Nevertheless, the distribution trends of the re-ordered spectrum at three levels in the right panel are very similar, which reflects the fact that the absorption coefficients are partially correlated. We further examine the correlated-k approach by performing heating rate calculations for two cases using the two-stream model SES1 (Sun and Rikus, 1999) at a spectral resolution of 0.01 cm^{-1} . One uses the reordered absorption spectrum as shown in the right panel of Figure 1 and thus the results are ‘exact’; the other uses the correlated-k spectrum as shown in the left panel of Figure 1. The difference between the results from these calculations exposes the errors induced by the CKD method. Since these calculations are extremely time consuming using a two-stream model, the calculations were only performed for the spectral band $350 - 400\text{ cm}^{-1}$ and the results are shown in Figure 2. It can be seen that the errors induced by the correlated-k method can be greater than 10 k day^{-1} at high spectral resolution calculations. However, the error is reduced to less than 0.001 k day^{-1} when the results are averaged across the band. The reduction of error in the band averaged results is obviously due to the cancellation of random errors at higher resolution. This cancellation together with the partial correlation of absorption coefficients at different pressure levels may explain the success of correlated-k method to the broad-band radiative transfer.

Figure 2. Longwave heating rate errors due to correlated k assumption calculated at line-by-line spectral resolution using SES1 two stream radiative transfer scheme. The calculations are performed for the spectral region $350 - 400\text{ cm}^{-1}$. The left panel shows the average heating error across the band.



3. DEVELOPMENT STRATEGY

The radiation models used in the BMRC global and regional systems are due to Lacis and Hansen (1974) in shortwave and Fels and Schwarzkopf (Schwarzkopf and Fels, 1991) in the longwave. These models have an advantage in efficiency, especially the shortwave scheme and therefore have been widely used for a couple of decades. However, since the physical processes in these models have been highly simplified to gain the efficiency, their accuracy is generally not good enough for many applications in NWP and climate studies. In particular, since the longwave scheme uses an emissivity approach and the cooling to space approximation, it does not possess detailed information about the absorption coefficient distribution and hence does not readily lend itself to the calculation of radiation transfer for scattering atmosphere, which is highly dependent on the magnitude of local absorption. Approaches to the accelerated calculation of radiative transfer that have detailed dependence on absorption coefficients, such as the correlated-k method used for SES2 and ESFT method used for SES1 are fully compatible with multiple-scattering methods.

There are a number of issues associated with the development of SES2 using the correlated-k method. One of them is the choice of spectral bands and how many sub-intervals or g points are to be used for determining the band average flux. Clearly, the more g points are employed the more accurate result can be achieved, but the code will be more expensive to run. In SES2, a minimum number of g intervals which maintained the accuracy of band average flux and heating rate was found for each band. The detailed method is described in section 8.

The second issue is that each correlated-k model must include a procedure to account for variations in a band's absorption coefficient with pressure and temperature. A common method is to scale a reference set of k_j values by an appropriate function of pressure or temperature. This method is used in the Edwards-Slingo radiation model. Our studies have indicated that this method is not accurate. The errors in the stratosphere and above are particularly large (Sun and Rikus, 1999). Alternatively, SES2 performs linear interpolation using stored sets of k_j values, which are obtained from a k distribution that have been calculated for the full range of atmospheric conditions of interest. Linear interpolation is utilized extensively in SES2, effectively eliminating discreteness effects. This also enables the model to accommodate micro-layering, which is important in modeling atmospheric inhomogeneities associated with surface/atmosphere and cloud/atmosphere interfaces. The reference k values are stored for 59 pressure levels from 1050 – 0.01 hPa with an equal spacing in log pressure as suggested by Mlawer *et al.*, (1997). For each reference pressure, k values are stored for values of temperature T_{ref} , $T_{\text{ref}} \pm 15$ K, $T_{\text{ref}} \pm 30$ K, where T_{ref} is the temperature corresponding to this pressure in the mid-latitude summer profile. The generation of such a large number of k distributions is a significant computational cost involved in the development of SES2 and similar models. The dataset, once established, however, can be repeatedly used in the generation of radiative parameterizations for other applications.

The third critical issue for the model is the method used to perform the radiative transfer for a spectral band with multiple active species. The treatment of overlapping gaseous absorption is a challenge for rapid radiation models, including those using the correlated-k method. This issue is addressed in SES2 following the approach developed by Mlawer *et al.* (1997) that introduces a parameter that allows any combination of two overlapping species to be analyzed accurately and efficiently. Mlawer's method has been modified in this study and our modification has been

been accepted by Mlawer and his group to be used in their model RRTM (Mlawer, personal communication).

The important strategy in this study is not only to develop a radiative transfer model but also a comprehensive package that can be used in many areas in the radiation field. The work which have been done with this system and proved to be useful are the development of an infrared radiance code for simulation of the satellite measurements of the brightness temperature (Sun and Rikus, 2004); a parameterization of global and net solar radiation at the surface, SURFLX (Sun *et al.*, 2007) and SES2 as will be detailed in this report. The fundamental role of GENLN2 in the development of these schemes is shown schematically in Figure 3. Two major components of the relationship between GENLN2 and SES2 are the spectral absorption coefficients determined by GENLN2 and the k distributions converted directly from the spectral absorption coefficients. This establishes a direct traceability from the absorption coefficients used in SES2 to high-resolution validations performed with the calculations of GENLN2 using observational data. The other major component of the relationship between GENLN2 and SES2 is the use of fluxes and heating rates calculated using GENLN2 to validate the results of SES2.

Similarly, the components of the relationship between SES2 and SURFLX are the generation of an empirical scheme for determining the radiative fluxes at the surface based on the results from SES2 and the use of results from SES2 to validate those from SURFLX. The important function of this system is its ability to validate models for a wide range of atmospheric conditions. GENLN2 and SES2 can only be validated against observations for a few cases due to limited data sources. The validation of SURFLX, however, can be done easily with variety available data obtained from field campaigns and satellite measurements and therefore provides backward validation for SES2 and GENLN2.

4. MODIFICATIONS OF GENLN2 AND ITS VALIDATION

Version 3.0 of the GENLN2 model is used in this study. GENLN2 allows users to calculate atmospheric radiances and transmittances and was used to calculate gaseous transmissions required by the Edwards and Slingo code (Edwards and Slingo, 1996). In order to use this model as a reference to validate the accuracy of a broad-band model, it is necessary to modify it to allow the calculations of monochromatic fluxes and heating rates. In the longwave spectrum the modification of GENLN2 followed the approach provided by Clough *et al.* (1992). Four point first moment Gaussian quadrature is used to perform the angular integration. The variation of the Planck function within a layer is taken into account using the linear in τ relationship as suggested by Clough *et al.* (1992). In the short-wave spectrum, the calculations are more complicated due to the effects of scattering. If we ignore the effects of scattering, the irradiance calculations in the short-wave are greatly simplified as the upward and downward irradiance can be calculated separately like those in the long-wave spectrum: downward irradiance is just the direct solar beam traveling from the top of the atmosphere to the Earth's

surface; upward irradiance for a nonzero albedo non-specular surface is the isotropic upwelling diffuse beam. We adopted the formula presented by Ramaswamy and Freidenreich (1991) to perform these calculations. Again we use the four point first moment Gaussian quadrature to perform the angular integration for the upward transmission. The Clough water vapour continuum model (Clough *et al.*, 1989) is used in GENLN2 and it has been updated several times. The current version used in the model is MT_CKD1.00 (Mlawer, personal communication).

Figure 3. Development strategies of radiation schemes.

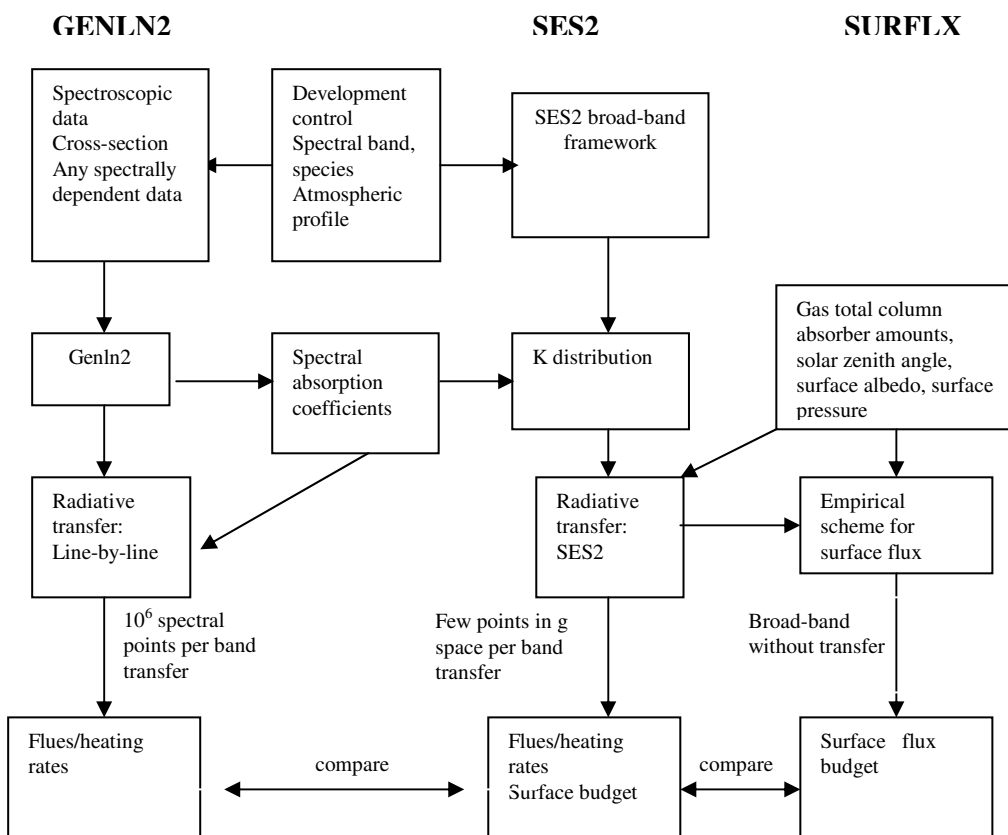
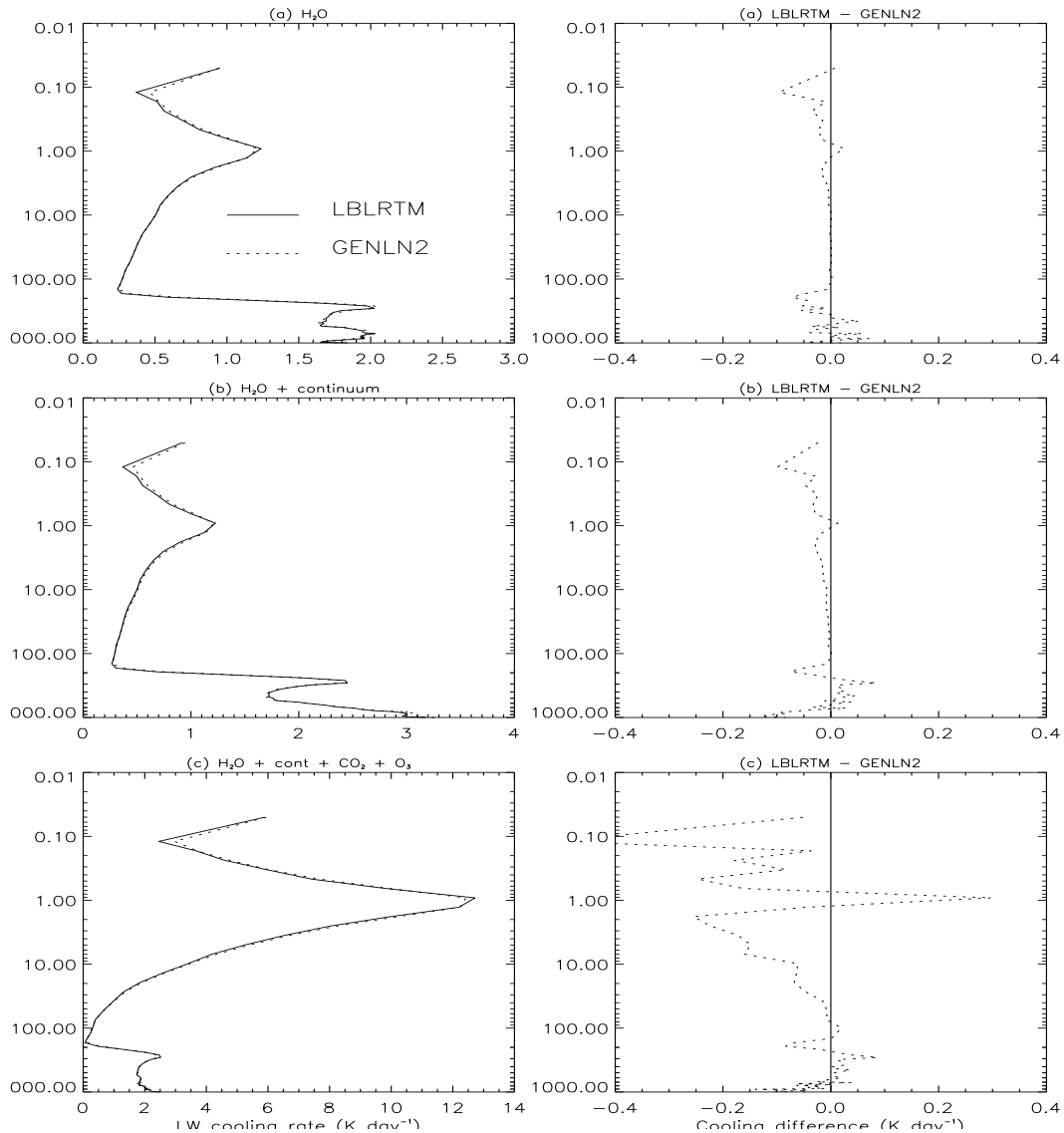


Figure 4. Longwave cooling rates determined using GENLN2 and LBLRTM for three ICRCCM test cases: (a) H₂O only; (b) H₂O + continuum; (c) H₂O + CO₂ + O₃.



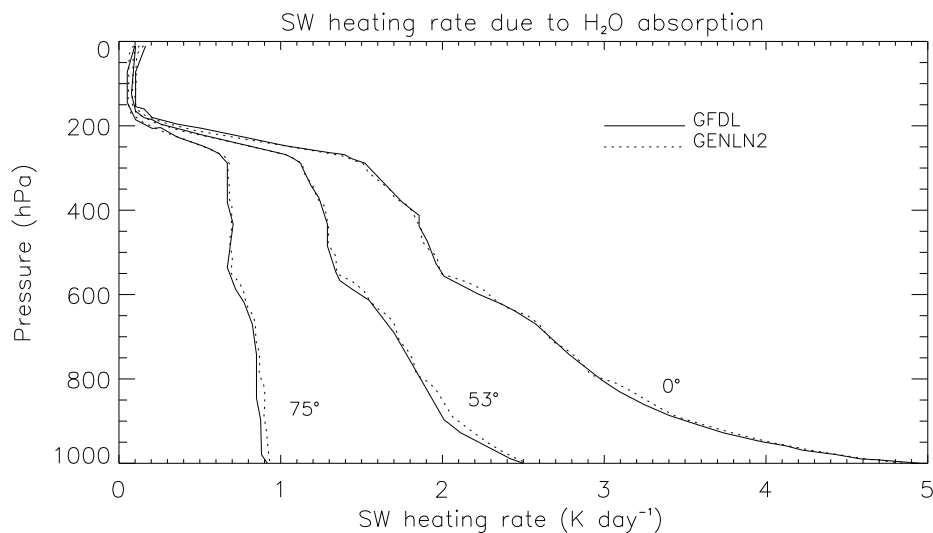
We first compared the longwave cooling rates determined using GENLN2 with those from LBLRTM (Clough et al., 1992). This comparison should be appropriate for the calibration as the flux algorithm and the water vapour continuum scheme used in GENLN2 are essentially the same as those used in LBLRTM. Unless otherwise indicated the results presented in this report are all calculated for the standard mid-latitude summer (MLS) atmosphere. Figure 4 gives a comparison between longwave cooling rates calculated using GENLN2 and the LBLRTM line-by-line models for the three test cases of the Intercomparison of Radiation Codes in Climate Models program (ICRCCM): MLS atmosphere including absorption by water vapour only (Fig 4a), water vapour and its continuum (Fig 4b) and water vapour plus its continuum, plus carbon dioxide and ozone (Fig 4c). It is seen that agreement between two the models is very good. The cooling rate differences for the first two test cases are about 0.1 K day^{-1} throughout the

atmosphere. The cooling differences for the third case are slightly larger for pressure levels above 10 hPa but still less than 0.4 K day^{-1} .

For the shortwave spectrum, we compared the solar heating rates determined by GENLN2 with those determined by the GFDL (Ramaswamy and Freidenreich, 1991) line-by-line model and this is given in Figure 5. The calculations use the MLS atmosphere with a surface albedo of 0.8. Only absorption by water vapour is considered in the calculations without including its continuum and Rayleigh scattering. Agreement between the two models is again very good. The heating rate differences between two models are about 0.1 K day^{-1} .

These comparisons indicate that the accuracy of GENLN2 is compatible with other line-by-line models commonly used in the community and therefore is appropriate to adopt for this study.

Figure 5. shortwave heating rates due to absorption by water vapour determined using GENLN2 and GFDL for MLS atmosphere. The calculations assume three solar zenith angles as indicated in the figure and a surface albedo of 0.8.

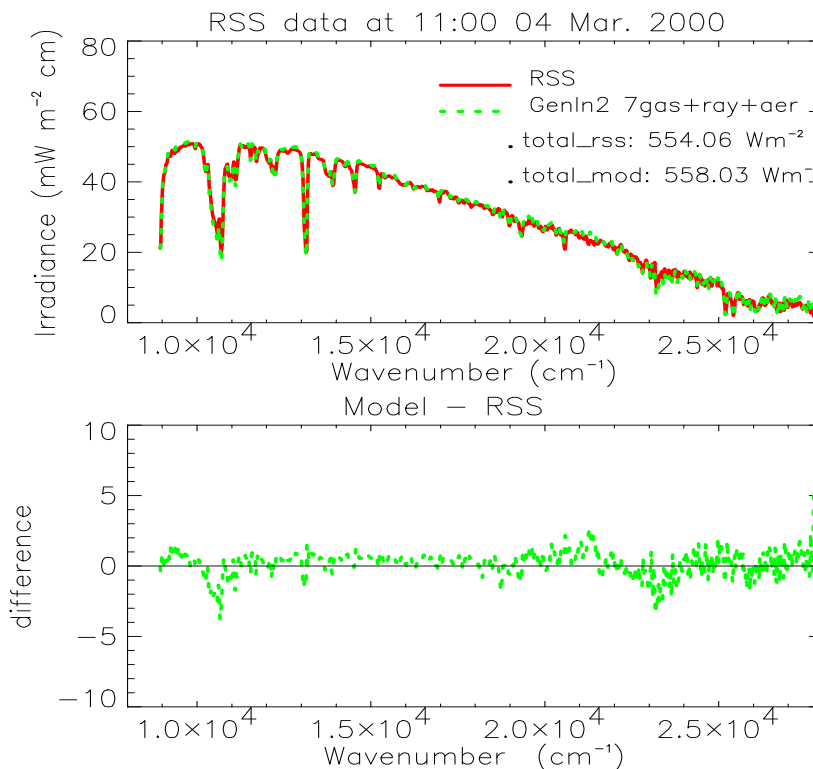


Apart from the above comparisons, Genln2 is further validated using the ARM observational data. The high spectral resolution data measured by the Rotating Shadowband Spectroradiometer (RSS) (Harrison *et al.*, 1999) at the ARM research site at Southern Great Plains for a clear sky condition are used for validation. The RSS provides spectrally-resolved direct-normal, diffuse-horizontal, and total-horizontal irradiances. The data measured by the second-generation instrument with a higher-performance 1024 x 256 CCD arrays are used in this work. The data from the first generation instrument have been used by Mlawer *et al.* (2000) to validate LBLRTM. The data obtained at 11:00 local time (solar zenith angle 43.59°) on 4 March 2000 were used. The pressure, temperature, and water vapour measurements from the radiosonde sounding form the basis of the atmospheric profile are used as an input to the model. The water vapour profile has been scaled to match the total column value measured by a microwave radiometer which provides an accurate determination of total water vapour column.

The mid-latitude summer ozone profile is used and the values are scaled to agree with a total value of 323 Dobson Unit which was obtained from the TOMS measurement nearer to the SGP site on that day. For a comparison with clear sky measurements, the Rayleigh and aerosol scattering must be included in the calculations. Therefore, we further added Rayleigh scattering to the GENLN2 calculations. Aerosol optical depths measured by collocated sun photometers (Min, 2002, personal communication) were interpolated onto the GENLN2 spectral grid and the downward irradiances at the surface were scaled by $e^{-\tau}$ to account for the attenuation by aerosols, where τ is the measured spectra aerosol optical depth. The RSS instrument (slit) response function was applied to the calculated irradiances, yielding a value of irradiance corresponding to each spectral channel of the instrument. 7 absorbing species are included in the calculations. The treatments of some absorbing species are described in next section. The result is shown in Figure 6.

It is seen that the modelled result is in a good agreement with observations. The differences between the measured and calculated irradiances, shown in the lower panel of Figure 6, are small across most of the measured spectrum. The total flux difference between the calculated result and observation is 4 W m^{-2} , which is generally smaller than the instrument uncertainty.

Figure 6. Comparison of measured (red curve) and calculated (green) solar spectral irradiances for a clear sky condition at ARM SGP site on 4 March 2000. Lower panel shows the differences



5. IMPLEMENTATION OF NEW ABSORPTION DATA IN GENLN2

The HITRAN (Rothman *et al.* 2003) spectroscopic database is a major source of absorption coefficients for absorbing species included in radiative transfer models. However, data for some species are not available in the HITRAN database and therefore other sources are required and the extra species need to be treated separately in line-by-line calculations. This section describes the treatment of these absorption coefficients in Genln2.

5.1 Ozone data

Ozone is an important minor constituent of the Earth's atmosphere and is a strong absorber of the solar radiation in the ultraviolet (UV) and weak absorber in the visible wavelengths. Ozone absorption is a major heating source in the middle atmosphere, which provides energy for photochemical reactions (Chou and Lee, 1996). Therefore, the treatment of the solar radiation absorbed by ozone is important in providing accurate heating rates in the middle and upper atmosphere and the radiation budget at the earth surface.

Laboratory measurements of ozone absorption cross-sections are normally used in calculations of the ozone absorption. There are many such measurements available (see Orphal, 2002 for a comprehensive review), but many of these data do not cover the full UV and visible spectral regions and cannot be used in radiative transfer models. There is also a lack of inter-comparison for those cross-section data used in radiative transfer models. In order to fill this gap, three ozone absorption cross-section datasets were examined using the GENLN2 line-by-line model to help select the best data. All these data have a full spectral coverage and are widely recognized in the community. The first set is due to Molina and Molina (1986) and Malicet *et al.* (1995) (hereafter referred to as Malicet). Malicet *et al.* (1995) fitted the temperature dependent of the measured cross-section data in terms of a polynomial function. The fitted coefficients in the spectral region between 195 and 850 nm are provided. The second dataset is that used in Lowtran7 (Kneizys *et al.*, 1988) and is referred to as Lowtran. This dataset has averaged cross-section data mainly from Molina and Molina (1986) but there is no temperature dependence. The spectral resolution of the Lowtran data is 100 cm^{-1} . The third dataset is that measured by Voigt *et al.* (2001) for the European Space Agency (ESA) remote sensing program (Orphal, 2002). This program was assigned to retrieve trace gas distributions from space platforms. This requires absolute absorption cross-sections for all relevant gases as a function of optical frequency for appropriate physical conditions (e.g. pressure, temperature, mixing ratio) and appropriate instrument conditions (e.g. spectral coverage and resolution). They made laboratory measurements of O₃, O₂, NO₂, SO₂ for specified physical and instrument conditions. The ozone cross-sections were measured at five different temperatures in the range 203-293 K and two pressures in the spectral region 230 - 850 nm with a spectral resolution of 5 cm^{-1} . Compared with the previous two datasets, the ESA data have a better temperature dependence and spectral resolution. Following the treatment by Malicet *et al.* (1995), the temperature dependence of the ESA data were fitted to a polynomial function at each wavelength. The pressure dependence was found to be insignificant (Voigt *et al.*, 2001) and is

therefore not considered in this study; the ESA data at 1000 hPa were used. These three datasets were implemented into GenIn2. A spectral resolution of 0.01 cm^{-1} was specified in calculations which used the MLS atmosphere, a solar zenith angle of 30° , and a surface albedo of 0.2. The voigt line profile was used.

Figure 7 shows a comparison of the ozone absorption cross-sections from these three datasets. The results from ESA correspond to a temperature of 246 K and those from Malicet were also determined using this temperature for a consistent comparison. The absorption cross-section data from Lowtran have no temperature dependence. The left-hand panel shows the results in the 200-850 nm regions. It is seen that the results in this figure do not show a significant difference except in the 340-480 nm and the 700-850 nm regions where the cross-section data are not available in the Lowtran data file. The other difference occurs in the region beyond 750 nm where the Malicet cross-section is larger than that from the ESA. The differences in other regions are hard to see because of the scale of the data. The right-hand panel presents the results in the Chappuis band between 500-700 nm with a different scale to explore the difference in this region. One can see that the cross-section from ESA is systematically larger than Malicet. The cross-section from Lowtran which appears to be a step function due to its low spectral resolution is also less than that of ESA.

Figure 7. Comparison of three ozone absorption cross-section datasets. Both the ESA and Malicet results represent the cross-section at a constant temperature of 246 K while the results from Lowtran denote values for averaged temperature. The right panel shows the results in the spectral region 0.5 - 0.7 microns in linear scale to emphasize the differences.

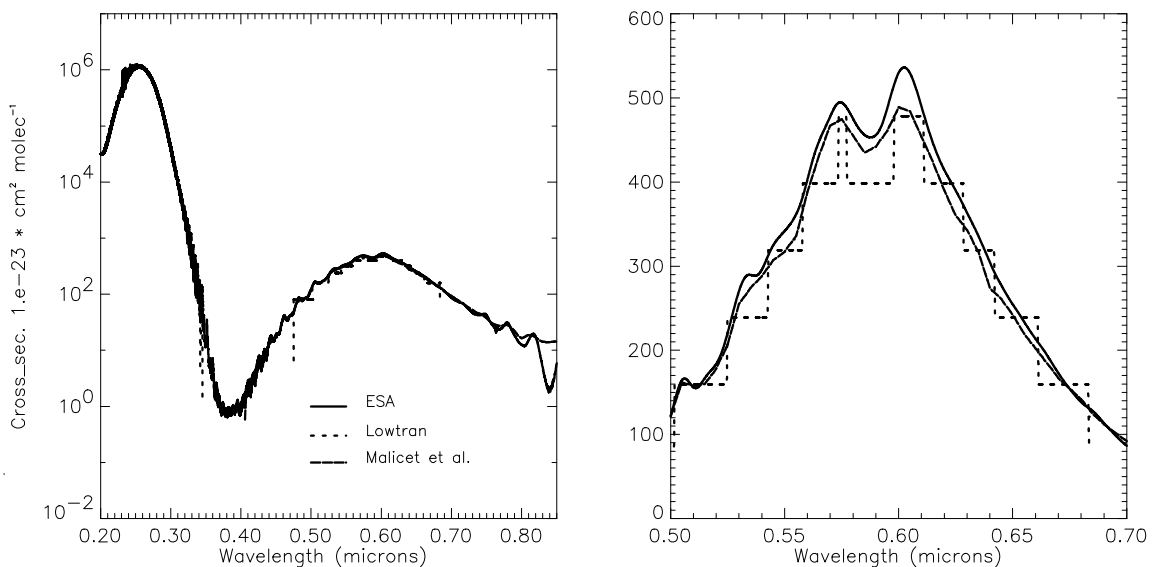


Figure 8 shows a comparison of the downward solar irradiance at the surface determined using these three absorption cross-section datasets. The results have been degraded to 10 cm^{-1} resolution. The differences between the results determined using the ESA data and those with Malicet and Lowtran are shown in the lower panel. It is seen that there is essentially no

difference in the Hartley band due to its strong absorption but differences in the other bands are noticeable. In the spectral region between 450 and 690 nm, the absorption of solar radiation determined using both the Lowtran data and Malicet is less than that determined using the ESA data. The maximum difference can be $0.6 \text{ mW m}^{-2} \text{ cm}$. The total absorption in the region between 200 and 690 nm determined using the three datasets is 37.629 (ESA), 36.211 (Malicet) and 36.730 (Lowtran) W m^{-2} , respectively. Therefore, the use of ESA cross-section data results in an increase of the absorption by 0.899 and 1.409 W m^{-2} relative to the Malicet and Lowtran data.

Figure 8. The upper panel shows the downward spectral solar irradiances at surface determined using the three O_3 absorption cross-section datasets. The differences (ESA minus Malicet and Lowtran) are displayed in the lower panel. The calculations assume a mid-latitude summer atmosphere, a solar zenith angle of 30° and a surface albedo of 0.2.

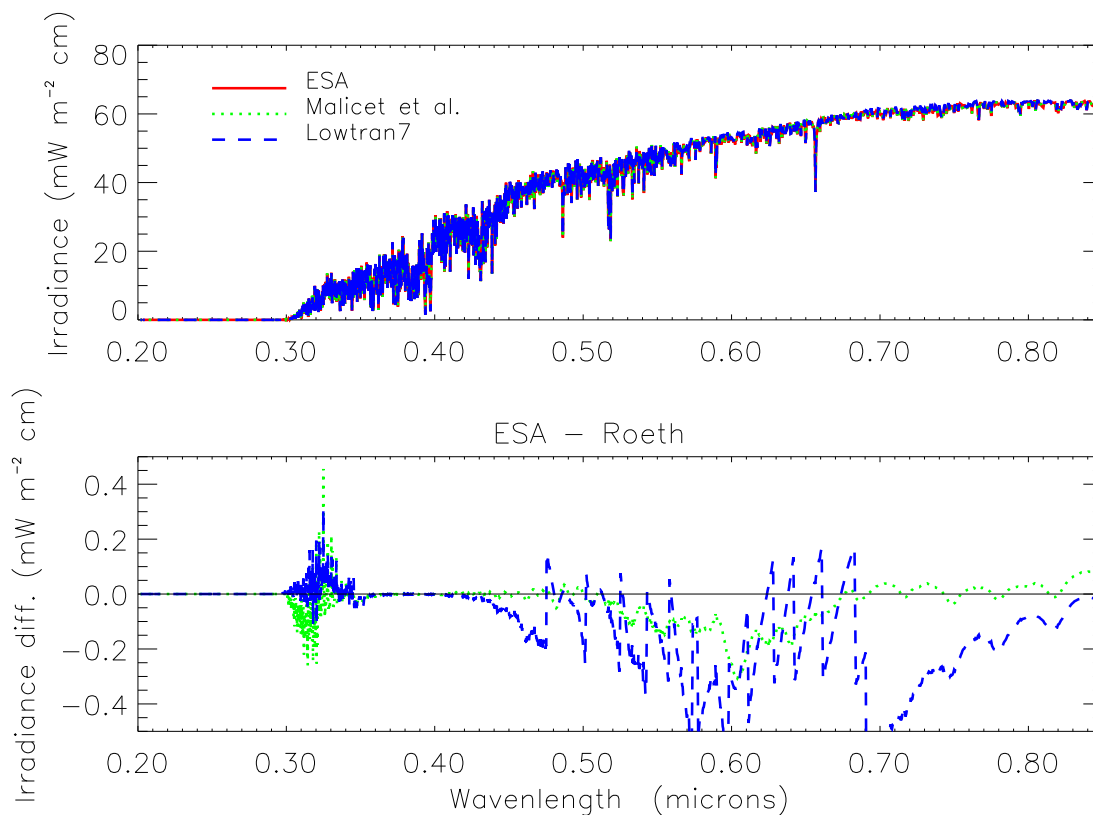


Figure 9 shows the comparison of heating rates determined using the three cross-section datasets. Use of the ESA cross-section data leads to an increase of solar heating rate at around 1 hPa by 0.35 and 0.2 K day^{-1} relative to that of the Lowtran and Malicet data, respectively.

The temperature dependence of the O_3 absorption cross-section is shown in Figure 10. It is seen that the variation of the cross-section with temperature mainly occurs in the Huggins band between 310 and 380 nm and the Wulf band between 700 and 800 nm. The O_3 absorption in

these bands is several orders of magnitude weaker than that in the Hartley band. Since the temperature dependence could not be considered in the previous studies (e.g. Chou and Lee, 1996; Sun and Rikus, 1999; Edwards and Slingo, 1996) due to lack of such data, it is worthwhile to examine its effect. For this purpose, the calculation was performed using the ESA absorption cross-section data determined with a fixed temperature of 250 K and the results were compared with those determined using the full temperature dependence of the ESA cross-section data. The results show that using a constant temperature causes the absorption to increase by 0.15 W m^{-2} , but the heating rate at about 1 hPa to decrease by 0.2 K/day. This is due to the fact that overall the O_3 absorption cross-section increases with temperature. At the 1 hPa level the temperature is higher than 250 K. Therefore using 250 K there leads to an underestimate of absorption. But for the atmosphere as a whole, 250 K is probably too high and results in an overestimate of total absorption. These figures indicate that the temperature dependence of the O_3 absorption cross-section does influence the absorption of solar radiation and should be taken into account.

Figure 9. Solar heating rate in the UV and visible region due to O_3 absorption determined using three absorption cross-section datasets (left panel). The differences (ESA minus Malicet and Lowtran) are shown in the right panel. The calculations assume a mid-latitude summer atmosphere, a solar zenith angle of 30° and a surface albedo of 0.2.

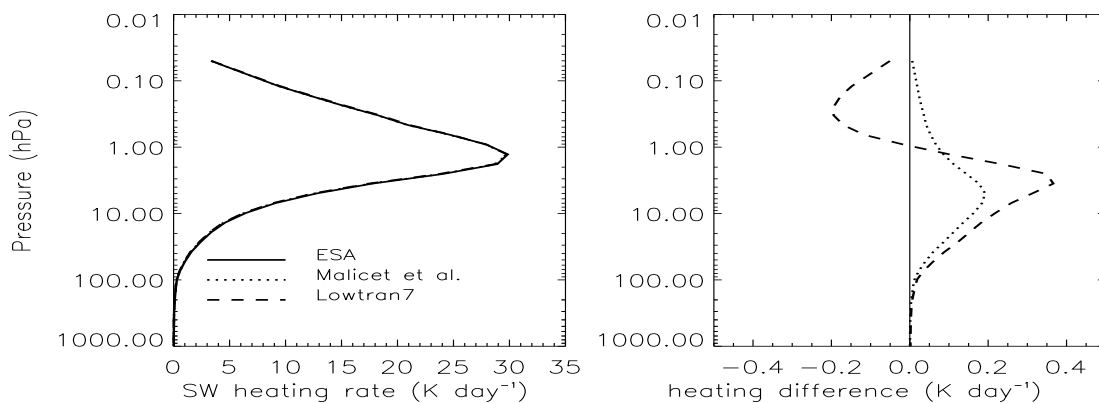
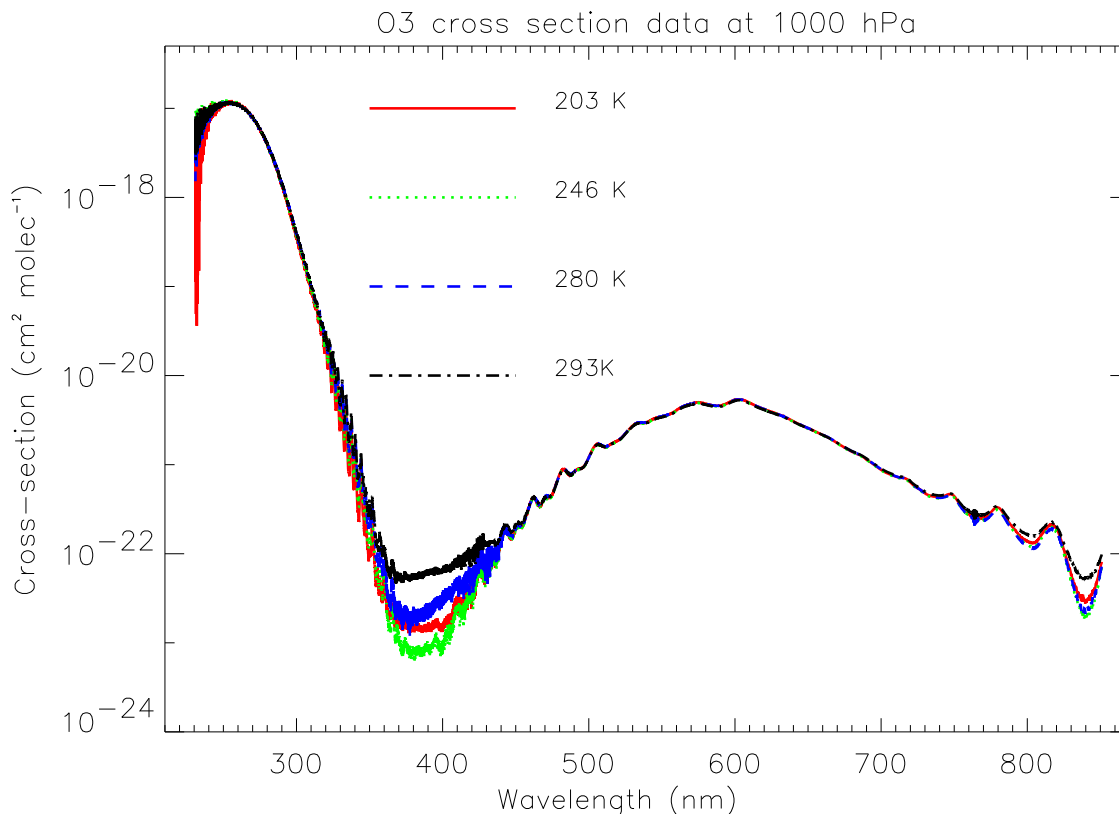


Figure 10. Ozone absorption cross-sections as a function of wavelength for five temperatures. The data were obtained from European Space Agency website.



5.2 Molecular oxygen collision induced continuum absorption

The molecular oxygen has absorption bands throughout the spectrum from infrared to ultraviolet (Newnham and Ballard, 1998). Some of these absorptions appear as continuum features arising from dimmer or collision complexes of oxygen (e.g. O_2-O_2 , and O_2-N_2). The later are described as collision-induced absorption. In the near infrared, the transition in O_2 produces the (0,0) band, centered near 7900 cm^{-1} ($1.27\text{ }\mu\text{m}$), the (1,0) band, centered near 9400 cm^{-1} ($1.06\text{ }\mu\text{m}$), and the (0,1) centered near 69300 cm^{-1} ($1.58\text{ }\mu\text{m}$) (Goldman, 1997). Currently, there is no theoretical solution to deal with these continuum absorptions. An empirical approach has been proposed by Mlawer et al. (1998) to solve the problem with these continuum absorptions. It is similar to the treatment of water vapour continuum. They developed an empirical model based on differences between the observed spectrum and calculations by the line-by-line (LBLRTM). They have shown that the LBLRTM residues have been greatly reduced using this scheme. However, the scheme has disadvantages in that it was not derived

directly from the absorption cross-section measurements and does not have temperature dependence. The later may be important in O₂ continua as shown below.

As mentioned early, the absorption cross-sections of oxygen have been measured by Smith and Newnham (Smith and Newnham, 2000) at the Rutherford Appleton Laboratory (RAL) for the ESA remote sensing program. They have analyzed data to work out the continuum cross-sections by removing the oxygen molecular line structured absorption. The continuum data for all three spectrum regions were generated for several temperatures and these data were implemented in GENLN2 for dealing with oxygen continuum absorptions. The optical depth for oxygen continuum absorption is determined by

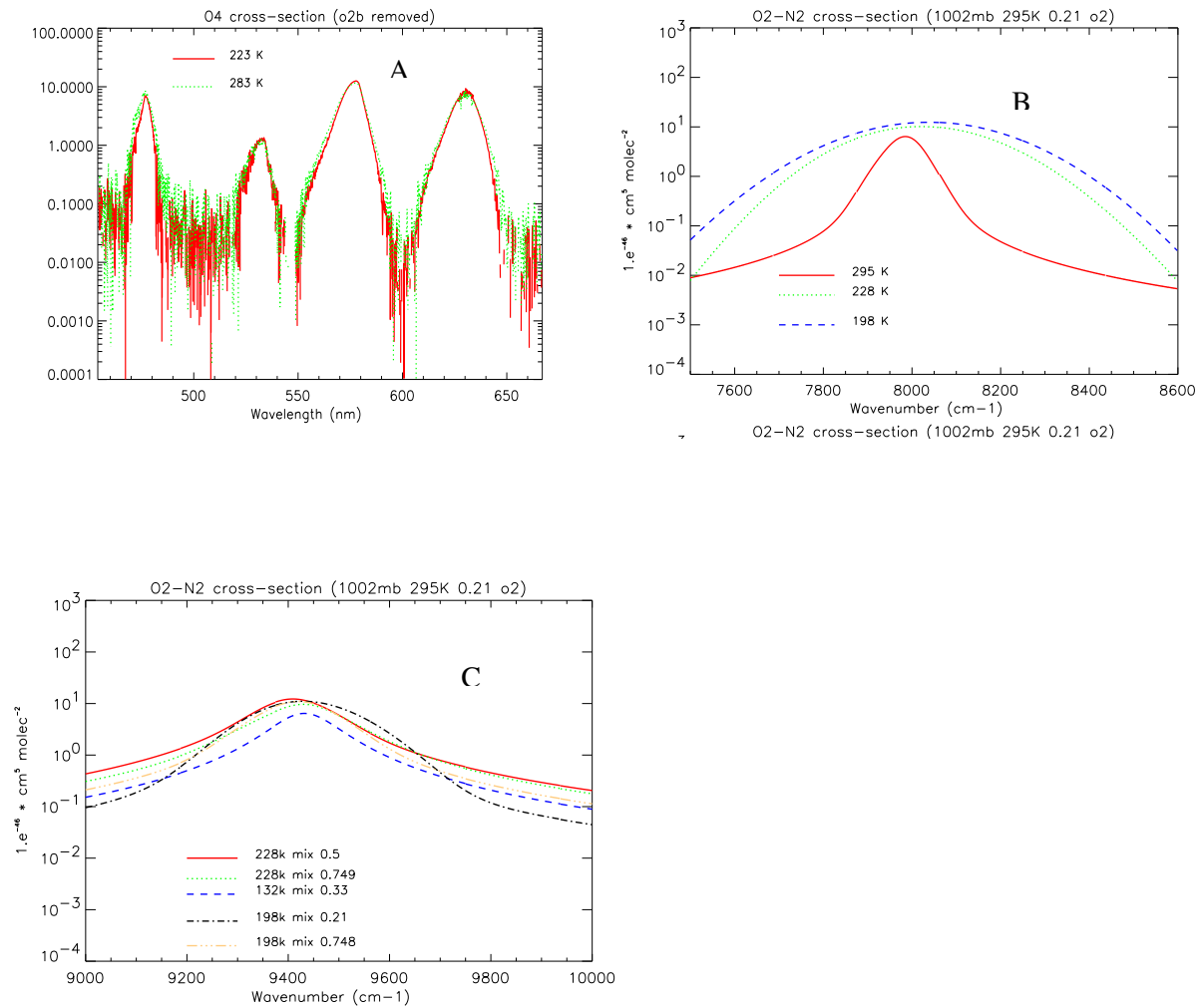
$$\tau_{o_2n_2} = \sigma_{o_2n_2} \rho_{o_2} \rho_{n_2} \Delta z \quad (10)$$

where $\sigma_{o_2n_2}$ is the absorption cross-section due to collision of oxygen and nitrogen, ρ represents the molecular density of oxygen or nitrogen. In the 1.59 μm band, the absorption is due to O₂-O₂ pair collision and therefore the index n_2 in equation (10) is replaced by o_2 . In the bands of 1.27 and 1.06 μm , the cross-section data for mixing ratio 21/79 of oxygen to nitrogen is used.

Figure 11 shows the oxygen continuum absorption cross-sections in the three major bands. It is seen that the temperature dependence of the cross-sections is only significant in the 1.27 μm band. The effect of temperature in the other two bands is not significant. Therefore, we only include the temperature effect in 1.27 μm band. The data in the other two bands are averaged and used in the radiative transfer calculations. In the 1.27 μm band, a linear interpolation is used to determine the cross-sections at different temperatures. For the temperatures outside of the data boundary the values at boundary temperature are used.

The influence of oxygen continuum absorption on the solar flux and heating rate has been investigated by Chagas et al. (2002) using a 220 narrow band shortwave radiation scheme of Slingo and Schrecker (1982). The data they used were derived from the same measurements in RAL but using a different method. They found that inclusion of both 1.06 μm and 1.27 μm continua in the calculations for the mid-latitude summer atmosphere with a solar zenith angle of 60° and a surface albedo of 0.1 leads to an increase of total atmospheric absorption by 1.10 W m⁻². The same calculations were performed in this study using GENLN2 and SES2 (SES2 model will be introduced later). In GENLN2 calculations, only gas absorptions are considered while in SES2 both the absorptions and Rayleigh scattering are included. Therefore, our result determined by SES2 is more compatible with those of Chagas et al. Figure 12 presents the downward spectral solar irradiances at the surface determined by GENLN2. The red curve represents the result without including the oxygen continuum and the green curve denotes that including the O₂ continuum.

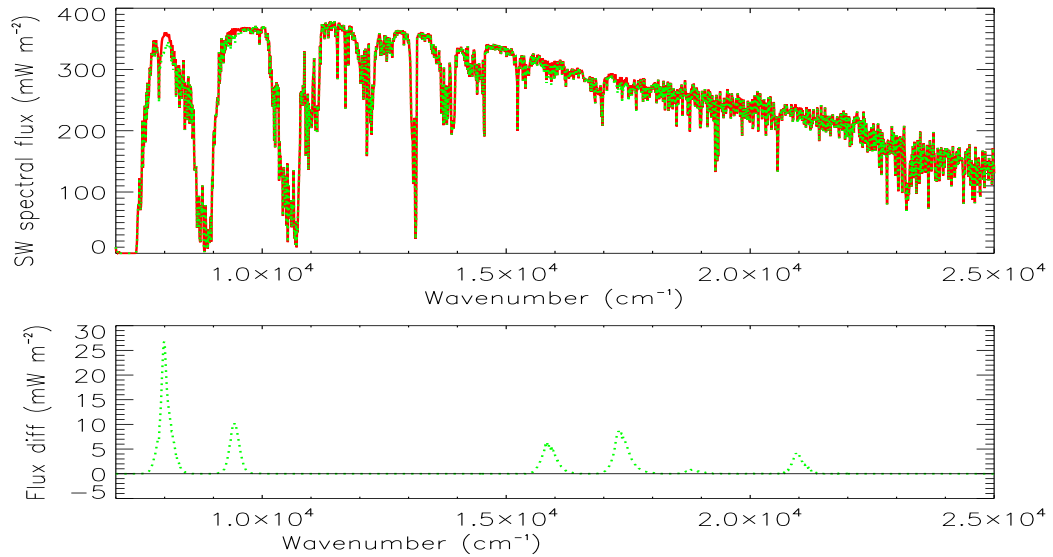
Figure 11. Binary cross-section for the absorption continuum in the 1.59 (A), 1.27 (B) and 1.06 (C) μm bands of oxygen for different temperatures derived by Smith and Newnham (2000).



The difference between the red and green curves plotted in the lower panel clearly shows the contributions from three oxygen continuum absorption bands. The absorption intensity is stronger in the 1.27 μm band than those in the other two bands. The total increased atmospheric absorption due to the effect of oxygen continuum is 1.52 W m^{-2} . This value is larger than that obtained by Chagas et al. (2002). However, the values determined using the SES2 model with and without the Rayleigh scattering are 1.09 and 1.13 W m^{-2} , respectively; which are closer to the Chagas' estimate, particularly for the case when the Rayleigh scattering is included. These comparisons indicate that the results determined with narrow or broad-band models are somewhat underestimated.

Figure 13 compares the solar heating rate with and without oxygen continuum absorption. The results determined using both the GENLN2 and SES2 are given and they are in a good agreement. Both models show that the heating rates in the lower troposphere are increased by about 2% that is consistent with the figure shown in Chagas et al. (2002).

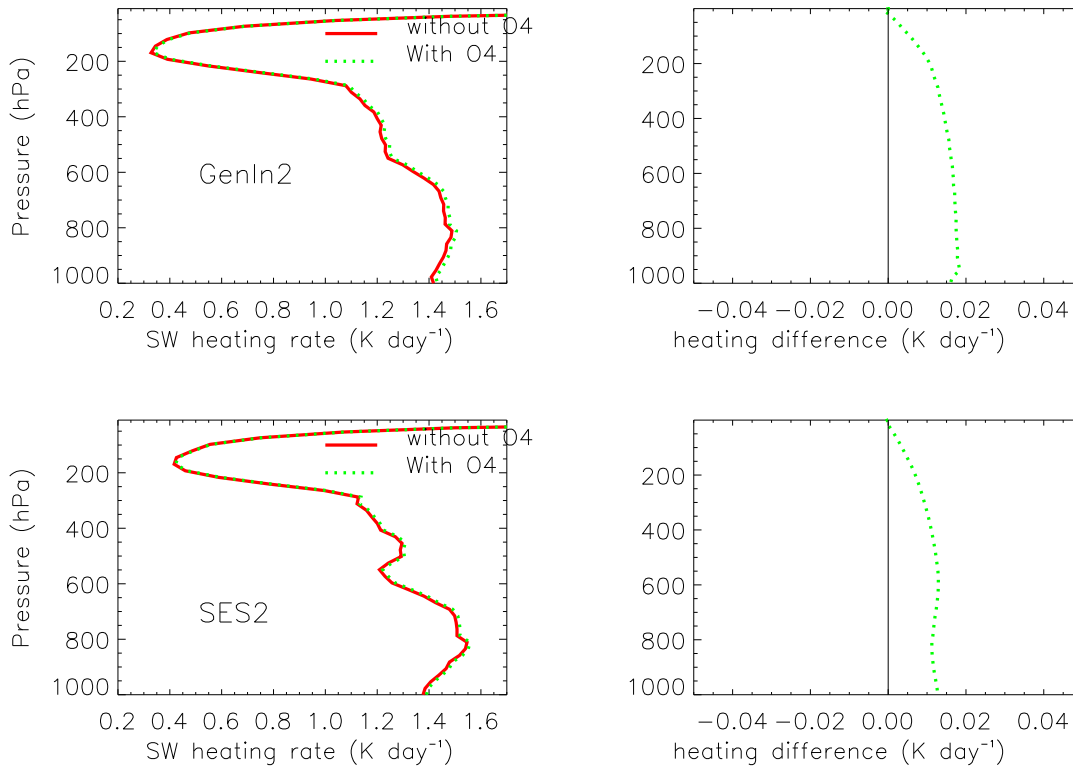
Figure 12. Solar irradiances calculated by GENLN2 for the cases with and without oxygen collision induced continuum. Three absorbing gases (H_2O , O_3 and O_2) are included in the calculations with a solar zenith angle of 60° and a surface albedo of 0.1. The lower panel shows difference, i.e. the result without O_4 (red curve) minus that with O_4 (green curve)



5.3 Cross-section data of SO_2 in UV band

The SO_2 has absorption in the UV spectral band between 260 nm ($38,460 \text{ cm}^{-1}$) and 320 nm ($31,250 \text{ cm}^{-1}$). The data are available at two temperatures (223 and 280 K) and two pressures (100 and 1000 mb). A linear interpolation is used to determine cross-section values at the other pressures and temperatures. Figure 14 shows the measured absorption cross-section spectrum for SO_2 . It is seen that the absorption of the solar radiation by sulphur dioxide in the UV band is highly spectral dependent and therefore needs higher spectral resolution model to resolve the spectral variations. This implementation has made it possible to study the shortwave radiative impact of this greenhouse gas.

Figure 13. The atmospheric heating rates due to shortwave absorption by water vapour, ozone and oxygen for a clear-sky mid-latitude summer profiles, solar zenith angle of 60°, surface albedo 0.1. The oxygen collision-induced absorption is included in both models and the Rayleigh scattering is included in the SES2 model.



5.4 Cross-section of NO₂ data

NO₂ measurements were made at 5 temperatures (223, 246, 269, 280, and 293 K) and two pressures (100 and 1000 mb). The spectral distributions of these data are displayed in Figure 15. The same implementation procedure as those of O₂ and SO₂ was applied to this gas.

Apart from absorbing species described above, Rayleigh extinction has also been added to GENLN2. This is for the sake of validating model against observations as shown in previous section.

Figure 14. Measured sulphur dioxide cross-section in the ultra-violet spectrum. The data are obtained from ESA website.

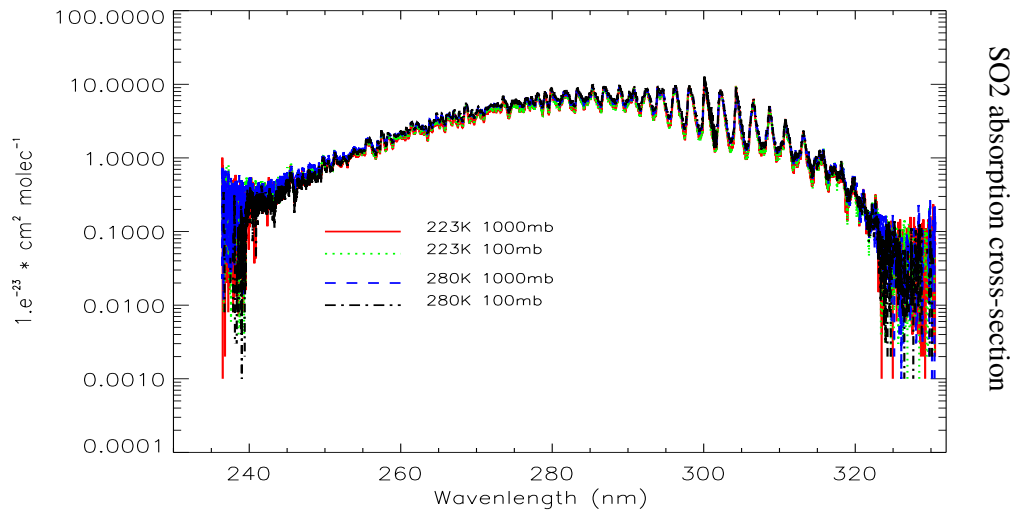
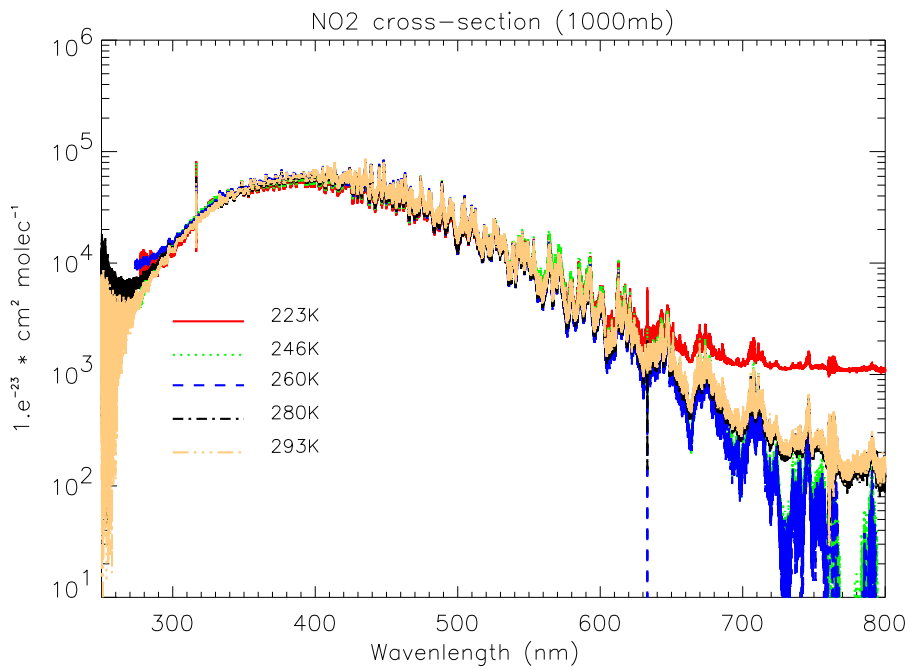


Figure 15. Measured nitrogen dioxide cross-sections. The data were obtained from ESA website



6. SOLAR SOURCE FUNCTION

Solar source function represents a solar spectrum at the top of the atmosphere. It is an energy source driving the general circulation in the earth atmosphere. The solar source function can be measured by satellite. The common source function used in the community is that provided by Labs and Neckel (Neckel and Labs, 1984). Because of instrument limits, the spectral resolution of the measured solar source function is not high enough for some research application. A synthetic solar source function generated by Kurucz (1992) has recently been adopted by community. The Kurucz solar source function is theoretical model result based on the measured results given by Neckel and Labs (1984). Several versions of this function are used in different radiation groups and they lead to quite large difference in the solar heating rate calculations. So far this difference has not been attracted attentions in the community. We are currently working on this issue trying to understand why there is such a large difference caused by using the different solar source function and find out which function provides realistic result.

In order to evaluate these source functions and their impact on radiative transfer calculations four functions collected have been implemented into GenIn2. These are: Kurucz original function in 1992; Kurucz function used in Atmospheric Environmental Research (AER); Kurucz function used in UK Met Office and Empirical College and solar source function of Labs and Neckel.

Figure 16 shows a comparison of these solar source functions. A large difference can be seen between Neckel-Labs and Kurucz functions. The lower panel displays the difference between the different Kurucz source functions (Versions of AER and UK minus Kurucz origin). It is seen that the difference is also significant. Figure 17 shows the percentage difference of the solar energy in three sub-spectral intervals between Neckel-Labs and Kurucz. It is seen that the change from the Neckel-Labs to Kurucz has led to increase of the solar energy in the UV region by 3%. Since the ozone absorption in this region is dominant solar heating source and the solar energy has a peak value in this region, this change results in a large change in solar heating in the upper atmosphere (see below). Even with the Kurucz function itself, different version also shows a significant difference in spectral distribution. Figure 18 shows a comparison of the solar heating determined using these four solar source functions. It is seen that the maximum solar heating difference between Kurucz and Neckel-Labs is about 4 K day^{-1} at 1 hPa. This change is significant. Such a large change in solar heating must have a significant impact on model simulations, especially for the simulations in the upper atmosphere. Unfortunately, no relevant researches can be found in literature, indicating that this issue has not extracted attention in the community. It is therefore necessary to conduct a study to assess this impact on NWP and climate simulations. This assessment will be conducted using the Australian Community Climate Earth Simulator System (ACCESS) model after the implementation of SES2 is completed.

Figure 16. Comparison of different version of the Kurucz solar source functions with that of Labs and Neckel. The lower panel shows the difference between Kurucz 1992 version and that used in AER and UK Met Office.

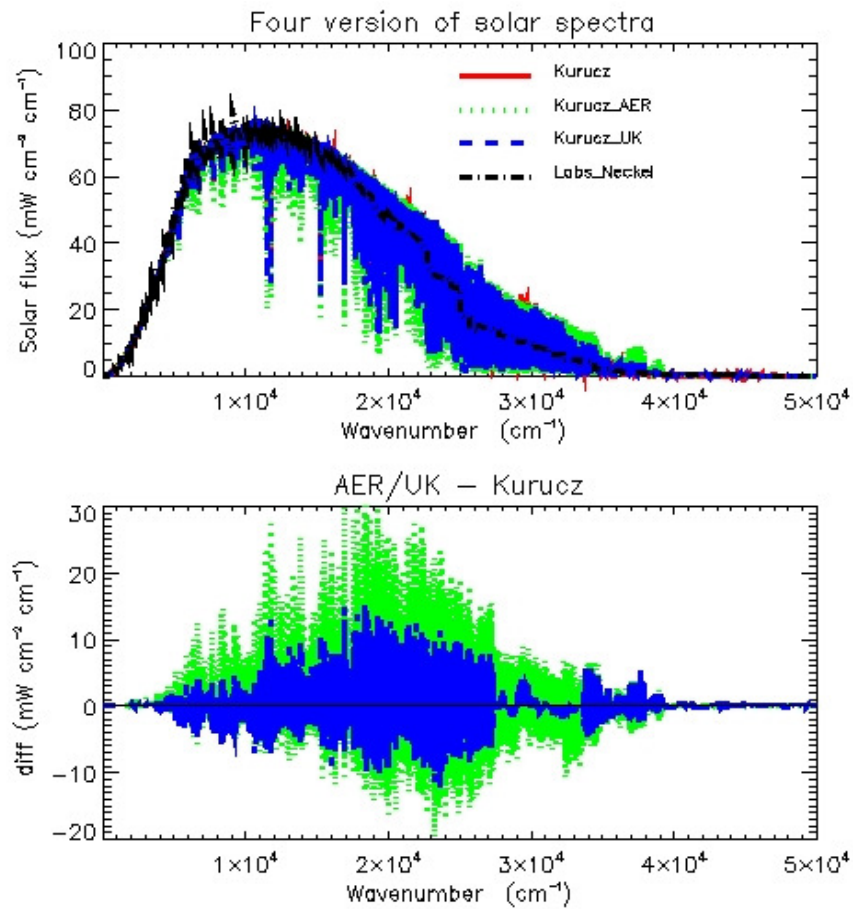


Figure 17. Percentage change in the solar energy in three major solar spectral bands due to the change from the Labs and Neckel solar source function to Kurucz source function.

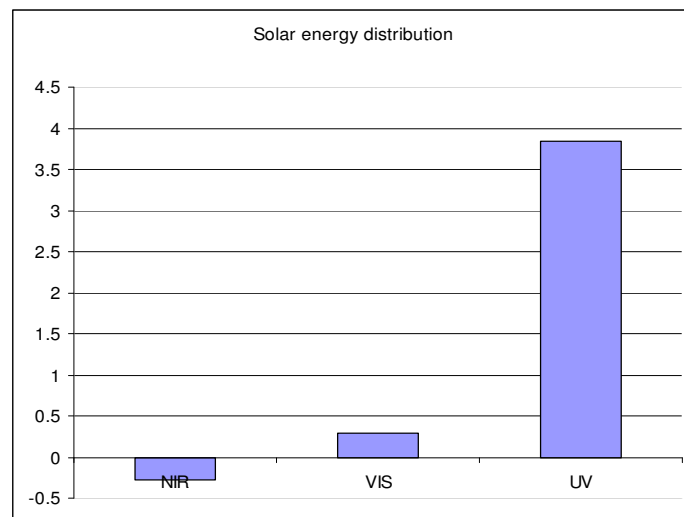
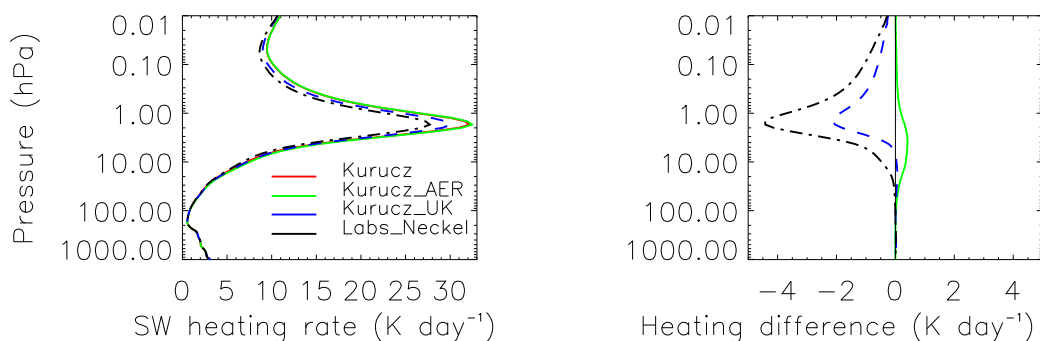


Figure 18. Solar heating rates determined by GENLN2 for 4 solar source functions.



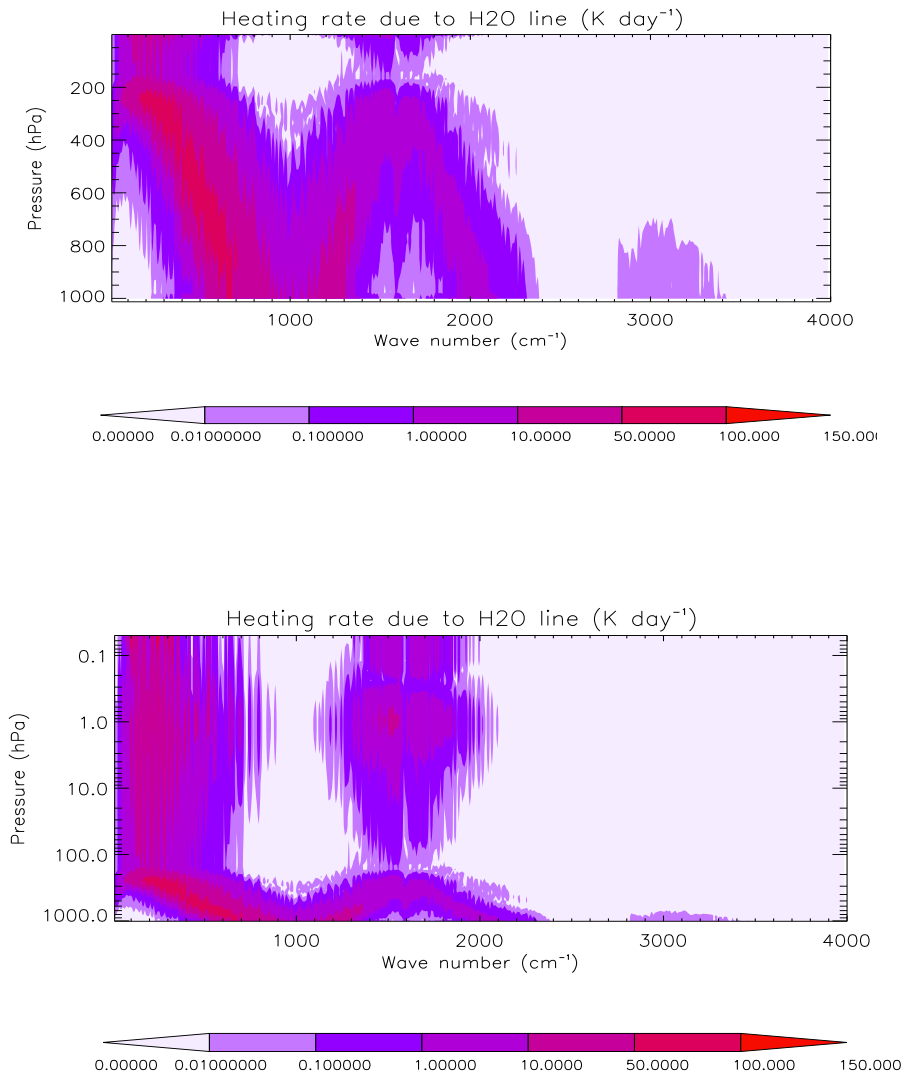
7. LINE-BY-LINE CALCULATIONS OF HEATING RATES FOR IMPORTANT ABSORBING SPECIES

The spectrally integrated fluxes and heating rates are essential radiative information necessary for the treatment of atmospheric processes. However, important insights can be obtained by careful consideration of the spectral distribution of these quantities. This is particularly important for the selection of the spectral bands and inclusion of absorbing species in each band. For this reason, the spectral heating rates are calculated using GENLN2 for a number of important absorbing species and the results are used as physical bases for designing the spectral band structure of SES2.

Figure 19 shows the longwave spectral cooling profile for water vapour without including the continuum absorption. The results are very similar to that presented by Clough et al. (1992) using LBLRTM. The cooling profile has a strong correlation with the absorption spectrum of water vapour shown in Figure 15 in Clough et al. (1992). The strongly absorbing regions of the water vapour spectrum provide the important contributions to the cooling rate at high altitude and weaker regions play the important role in the lower atmosphere. In stratosphere (lower

panel), the absorption of water vapour in the pure rotation band dominates cooling in this region. The absorption in 6.3 μm band ($1200 \sim 2000 \text{ cm}^{-1}$) is also apparent in the stratosphere.

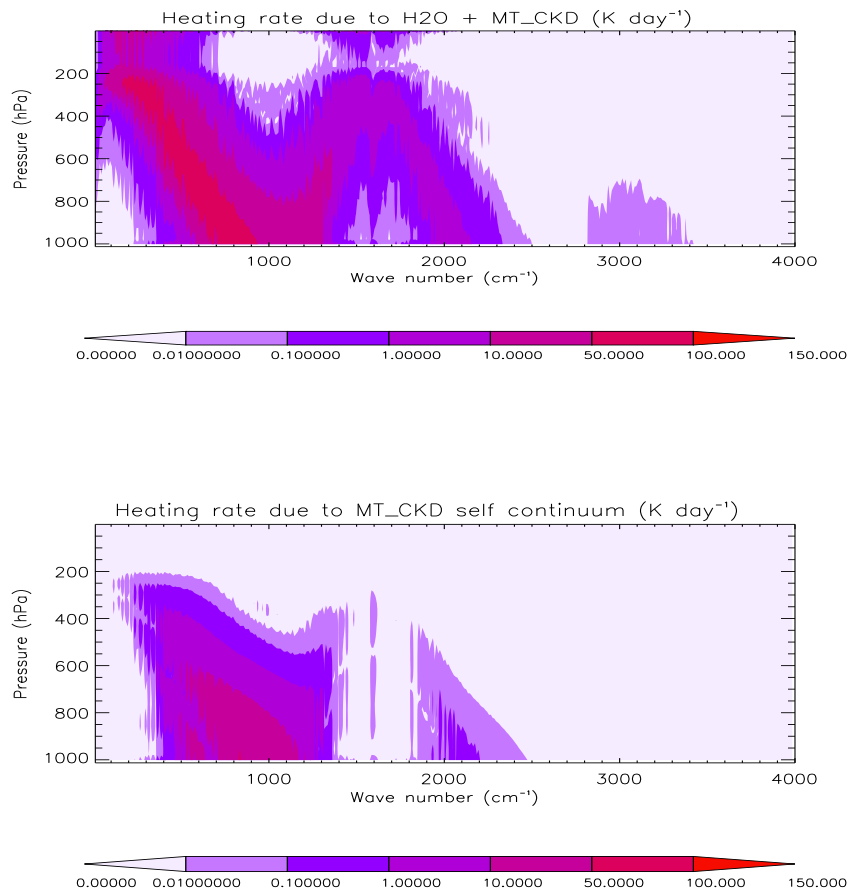
Figure 19. Spectral cooling rate profile for water vapour (no continuum) as a function of pressure of midlatitude summer atmosphere. The upper panel uses a linear scale to emphasize results in the troposphere and the lower panel uses a logarithmic scale to emphasize the results in upper atmosphere. Color scale $\times 10^{-3}$ is in unit of $\text{K day}^{-1} (10 \text{ cm}^{-1})^{-1}$.



The absorption of water vapour self-continuum has an important contribution to the longwave cooling rate in the troposphere. The cooling profile including this component is shown in Figure 20. The difference between this profile and that without including the self-continuum is also shown in this figure. It is seen that the inclusion of the self-continuum absorption increases the cooling rate by one color unit in the spectral regions $500 \sim 1200 \text{ cm}^{-1}$ and $1800 \sim 2500 \text{ cm}^{-1}$ where the absorption due to the water vapour line is relatively weak. The contribution to the

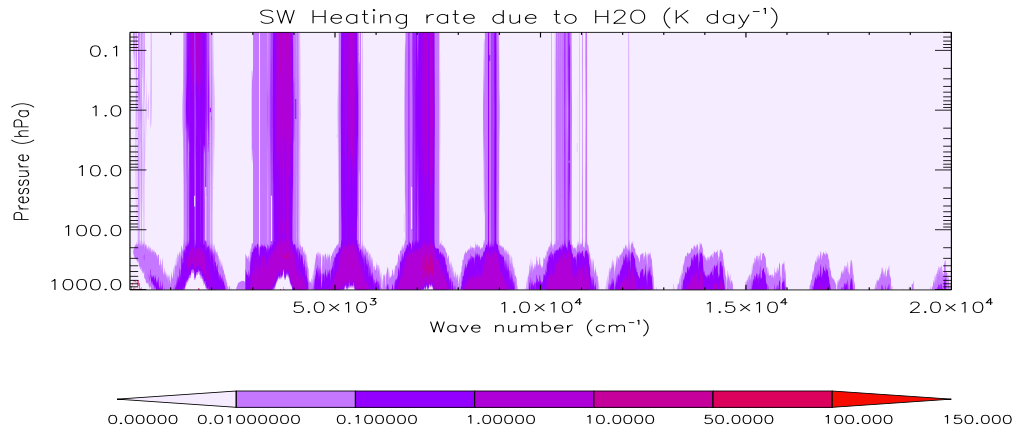
cooling rate due to water vapour self-continuum absorption can be clearly seen in the lower panel of this figure.

Figure 20. Spectral cooling rate profile for water vapour including self continuum (upper panel) and self-continuum only (lower panel) as a function of pressure for midlatitude summer atmosphere. The color scale $\times 10^{-3}$ is in unit of $\text{K day}^{-1} (10 \text{ cm}^{-1})^{-1}$.



The shortwave spectral heating profile for water vapour is shown in Figure 21. The heating rates spread from the infrared to visible regions. Small heating rates even occur in the spectrum $14500 \sim 20000 \text{ cm}^{-1}$ where the water vapour effect is usually ignored in early radiation codes (e.g. Slingo and Schrecker, 1982). The absorption in the shortwave also shows a band structure and the band width is wider in troposphere than in stratosphere. The absorption for spectrum $> 12000 \text{ cm}^{-1}$ can be ignored in stratosphere.

Figure 21. Shortwave spectral heating rate profile for water vapour as a function of pressure for MLS atmosphere. Color scale $\times 10^{-3}$ is in unit of $\text{K day}^{-1} (10\text{cm}^{-1})^{-1}$



The spectral heating rates for other species are all captured in Figure 22. The spectral distributions of heating rates for carbon dioxide, methane, nitrous oxide and oxygen have a similar signature in that they all have narrow absorbing bands. In order to resolve these absorbing properties, the band structures for a radiation code should be carefully designed to capture these characteristics. In comparison, the spectral heating rate for ozone shows a smoothly continuous distribution. This feature indicates that the absorption by ozone can be treated using a relatively wide spectral band. In SES1, for example, we used one band to treat the ozone absorption in the UV spectral region. Nevertheless, the number of spectral bands in SES2 has been increased to 4 in order to better resolve the UV radiation and spectral variation of aerosols.

Based on the spectral heating rate distributions presented above, the spectral band limits for the SES2 are designed and they are shown in Table 1.

Figure 22. Shortwave spectral heating profiles for (a) carbon dioxide, (b) methane, (c) nitrous monoxide, (d) oxygen and (e) ozone.

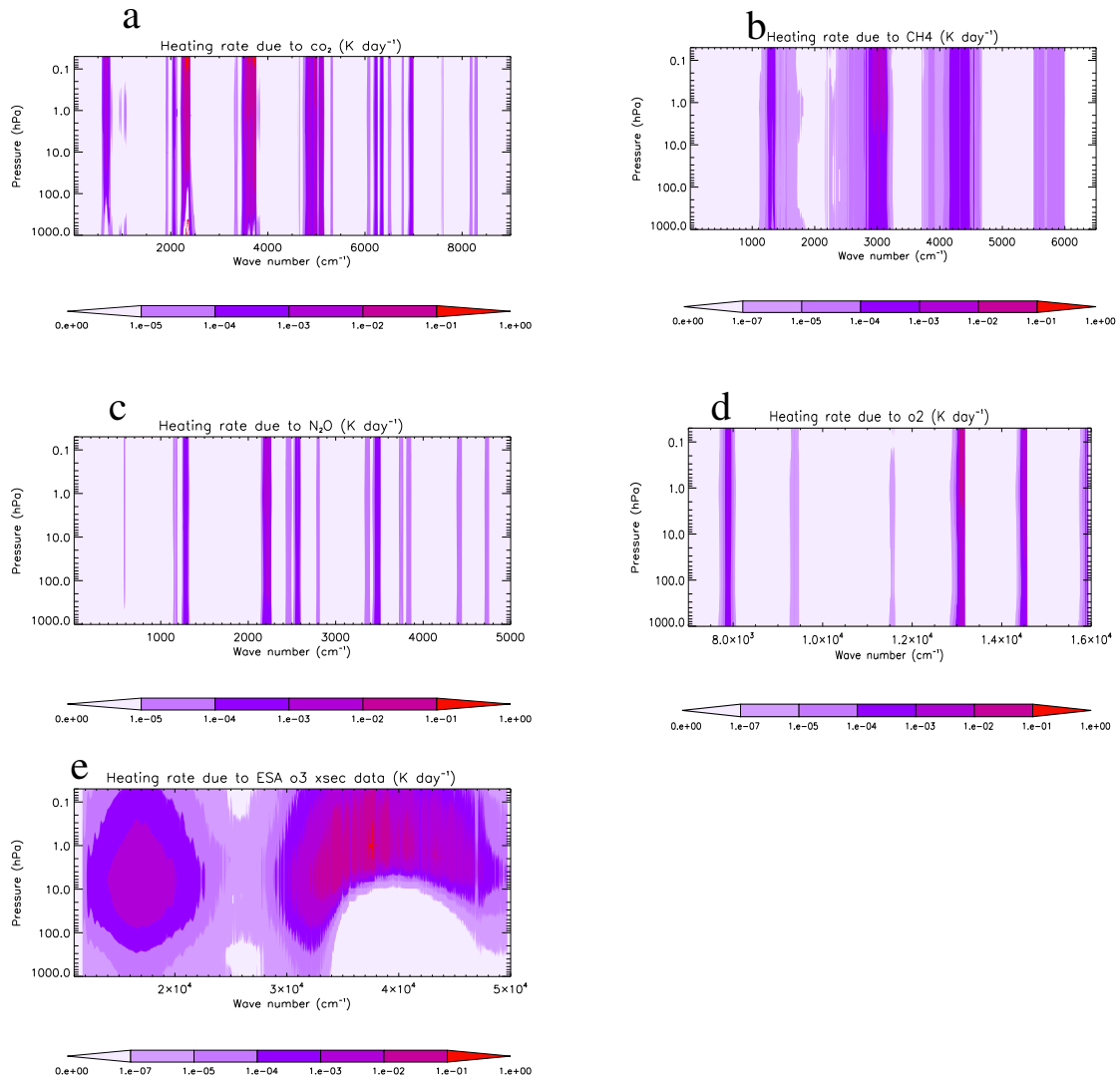


Table 1. Division of spectral bands, absorbing species and number of k terms in each band

Band	SW (μm)	Species	Number k
1	0.20~0.45	O ₃	3
2	0.45~0.50	O ₃	1
3	0.50~0.63	O ₃ , H ₂ O	1
4	0.63~0.70	O ₃ , H ₂ O, O ₂	1
5	0.70~0.83	O ₃ , H ₂ O, O ₂	2
6	0.83~1.18	H ₂ O	4
7	1.18~1.67	H ₂ O, CO ₂ , O ₂	5
8	1.67~2.50	H ₂ O, CO ₂ , CH ₄ , N ₂ O	5
9	2.50~ 5.00	H ₂ O, CO ₂ , CH ₄ , N ₂ O	5
LW	LW (cm^{-1})		
1	25 ~ 250	H ₂ O	4
2	250 ~ 520	H ₂ O	6
3	520 ~ 800	H ₂ O, CO ₂ O ₃ N ₂ O	7
4	800 ~980	H ₂ O, CO ₂ CFC11 CFC12 CFC113 CFC114	2
5	980 ~ 1100	H ₂ O, CO ₂ O ₃ CFC11 CFC12 CFC113 CFC114	3
6	1100 ~ 1400	H ₂ O, CH ₄ , N ₂ O	4
7	1400 ~ 2000	H ₂ O, N ₂ O	2
8	2000 ~ 4000	H ₂ O, CO ₂ , CH ₄ , N ₂ O	3
		Total number	58

8. CORRELATED K-DISTRIBUTION DEVELOPED FOR SES2

The development of k-distribution model has been well established. Any new work in this area should be focused on the issue of efficiency as this is critical to the operational NWP application. There are two issues in this method that affect the accuracy and efficiency. One is the method used to determine the sub-intervals in g space; the other is the method to determine a corresponding k value for each interval that may be representative in this interval. There is no unique method for identifying the optimal number of k terms. It is normally determined by the balance between accuracy and speed. It is found from our experiences that the ESFT method may be superior in limiting the number of k terms to the methods which calculate Δg_i interval from physical principles. This method was also suggested by Cusack et al. (1999). Using the ESFT, the Δg_i and values of k_i at a reference pressure and temperature are determined simultaneously for a given fit accuracy. For a fixed accuracy, the number of k terms determined by the ESFT method depends on the reference pressure at which the transmissions are calculated. At low pressures the Doppler broadening dominates, absorption coefficients are spread over a wide range of order of magnitude that result in more k terms needed in the ESFT fit than when a high pressure is chosen as a reference. Although the ESFT with a high reference pressure can lead to a reduction in the number of k terms, it cannot be used to develop a k-distribution model as the accuracy of radiation at upper atmosphere cannot be guaranteed. The lower reference pressure has to be chosen in the ESFT fit in order to accurately resolve the sharp variation of absorption coefficients for the g interval close to 1. It is almost impossible to obtain accurate fit with only a few k terms (e.g. < 5) if a low reference pressure is used. To solve this problem, we sacrifice the fit accuracy by using a fixed number of k terms in ESFT to determine the values of g interval. The lost of accuracy is then recovered by adjusting the k value in each g interval as introduced below.

For each g interval, a representative k value can be determined by following methods. The simple one is to obtain the representative k by a linear average of all k values across the g interval as used by Mlawer et al. (1997). The second is to use a k value corresponding to the middle point within the g interval. The third method is to calculate average transmissions across the g interval for a set of absorber amounts and fit the results to grey exponential function to determine k . The fourth is to calculate a mean k value weighted by transmission calculated at each g grid across the interval. In Figure 23, we show the k distributions determined using these methods for a spectral band $0 - 250 \text{ cm}^{-1}$. We first use the ESFT to determine the number of g intervals for a reference pressure of 1 hPa and a temperature of 250 K. For an accuracy of 10^{-4} for the band average transmissions, 10 exponential terms was resulted from the ESFT fit. We then used the above methods to determine the k values in each g interval. The solid curve in Figure 23 represents the line-by-line result and the symbols denote the k distributions determined using different methods. The k values determined by ESFT are also shown in the figure. It is seen that there are no significant difference for the k values in the first 7 g intervals (left panel) determined by different method. However, the difference becomes larger for g intervals close to 1 (right panel). Since the k values for g close to 1 dominate the radiative flux and heating rate in the upper atmosphere (Li and Barker, 2005), these differences must lead to a large differences in the radiative transfer calculations. These methods are examined with the radiation code and it is found that if a number of k terms is large enough (e.g. 16 terms as used in Mlawer et al. 1997), the differences in radiative fluxes

and heating rates determined using these methods are not significant. However, if only a few k terms are used (e.g. 7 k terms) a large difference occurs.

Figure 23. Absorption coefficients in each g interval determined using the five methods. The solid curve represents the values at the line-by-line grids and the symbols denote those using 10 g points.

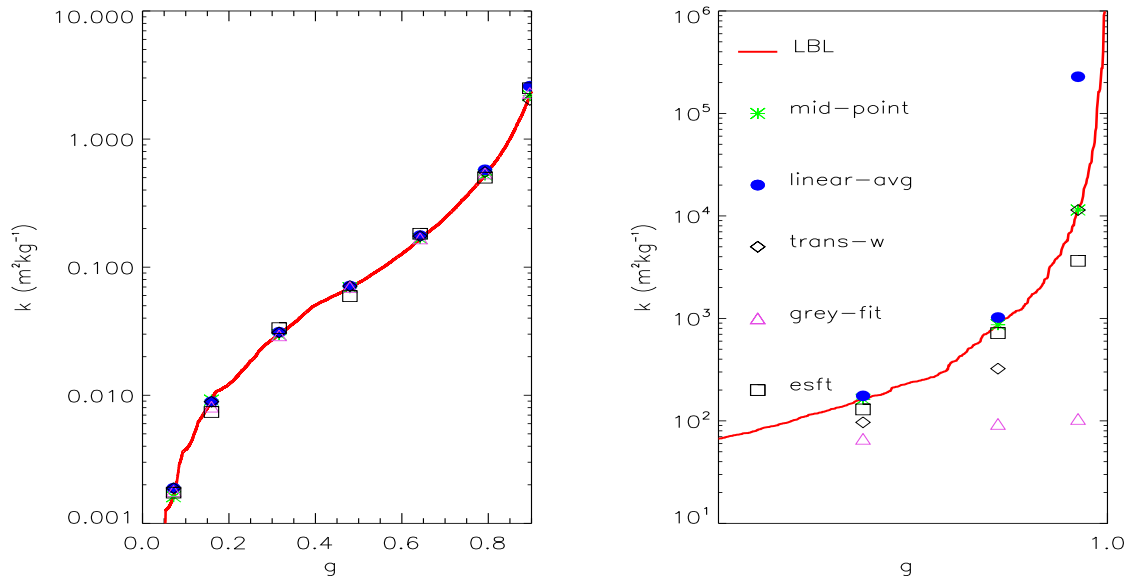
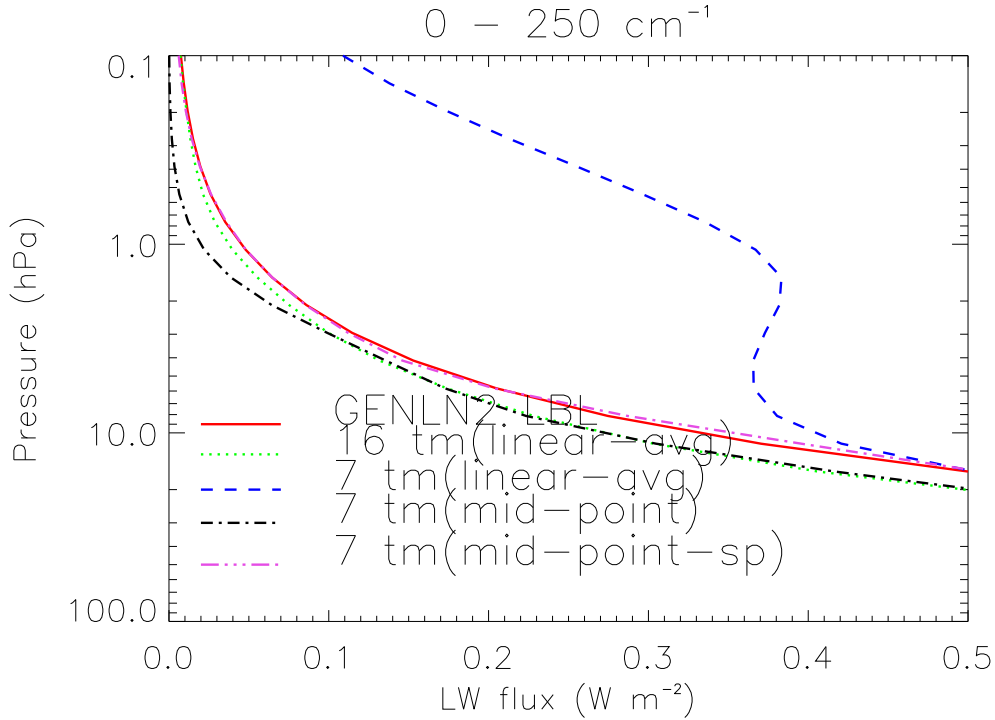


Figure 24 shows the downward fluxes above 100 hPa determined using these methods. One result is determined using 16 k terms and the rests are determined with 7 k terms. The red curve in the figure represents the reference result determined by GENLN2. For Clarence the results from the gray fit and transmission weighting methods are not shown as these are worse than those shown in the figure. It is seen that for the results determined with 7 k terms, the method of linear average generates a larger error for the downward flux. The method using a k value at the middle point within a g interval results in a compatible flux profile with that using 16 k terms. This comparison indicates that the k value at the middle g point may be a better representative if the number of g intervals within a band is small. Although it is superior over the other methods, the result is not as good as that from using 16 k terms. Therefore, we try to find an alternative approach.

As seen above, the problem mainly occur above 100 hPa when g is close to 1, we try to adjust the k values in these intervals. In fact, it is just the last k term that causes the significant fluxes departure from the reference values. Therefore, we used the following function to scale k values in the last g interval.

Figure 24. Downward irradiances above 100 mb determined using the LBL and SES2 with 4 methods of determinations of absorption coefficients. The calculations use MLS atmosphere with 60 layers. The legend 'sp' means a pressure scaling to the last k term above 3.5 mb.



$$k_7' = k_7(p / p_0)^n \quad (11)$$

where p is the pressures above 100 hPa and $p_0=1013$ hPa. Parameter n is determined by minimizing an error equation defined by

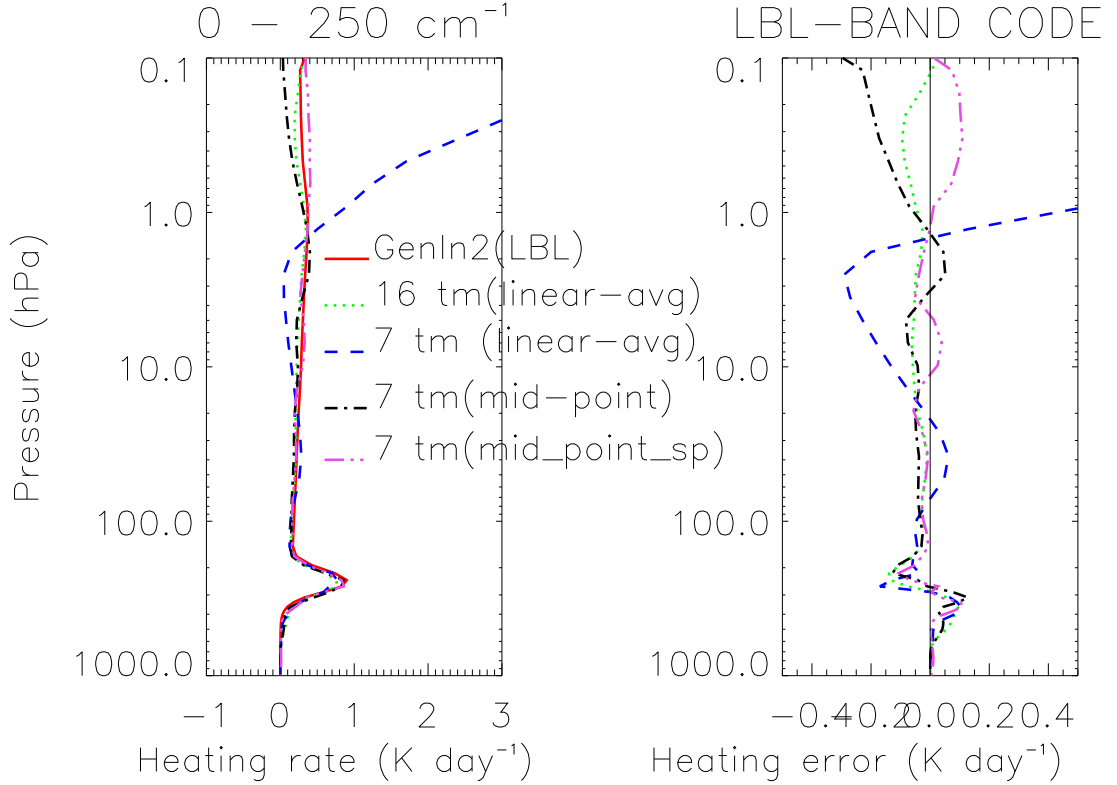
$$\epsilon_i = \sum_{l(p=100)}^{l(p=0.001)} (N_l^{ref} - N_l^i)^2 \quad (12)$$

where N^{ref} represents the net radiative fluxes determined by GENLN2 and N^i denotes the net fluxes from the CKD method. The result determined using this scaling parameter is also shown in Figure 24 which has an almost same accuracy as that from using the 16 k terms. The heating comparison is shown in Figure 25. Again, the accuracy of the heating rate determined using the 7 k terms with the scale equation (11) is compatible with that from using the 16 k terms.

The above exercise indicates that for a fewer number of g intervals the representative k values may be better determined by a numerical fit. This is just what the ESFT does. The difference between the ESFT method and the above approach is that the ESFT adjusts all k values and width of g intervals to get an overall better result by gradually increasing the number of k terms until the satisfactory accuracy is achieved. Our approach is to adjust the last k term only that contributes a large error in radiation calculations in upper levels of the atmosphere. This means that the numerical fit may be better performed for each g interval separately to obtain a best

representative k value in that interval. This will require line-by-line calculations using the re-ordered absorption coefficients so that the flux profiles for each interval can be obtained and used as reference for the fit. This procedure is applicable but too expensive. Alternatively, we proposed the following procedures to achieve the above approach.

Figure 25. Longwave heating rates (left) and errors (right) determined using LBL code and SES2 with 4 methods of determinations of the absorption coefficients. representative k value in that interval.



For each band, we generate a reference CKD code using 145 k terms as suggested by Fu and Liou (1992). The accuracy of radiation calculation determined using such a large number of k terms in the g space can be safely guaranteed. We then use the ESFT to determine the weights for a fixed number of intervals. The representative k value in each interval is determined by minimizing the error function given by

$$\mathcal{E}_i = \sum_{l=m1}^{l=m2} (N_l^{145} - N_l^i)^2 \quad (13)$$

where N^{145} is the net flux in each g interval determined by the reference code, and N^i is the flux determined by the code with single k profile. We start this process with one interval and gradually increase the number of intervals until a satisfactory result is obtained. The k values corresponding to the middle point in the interval are used as initials. The summation in Eq. 13

is from reference pressure level m_1 to m_2 , where m_1 and m_2 are determined by eye from examining the flux and heating rate profiles for each g interval. Therefore, only the k values within these two reference pressure levels are fitted. In general, the values of m_1 and m_2 shift from a high reference pressure regime to a low pressure regime as the g interval moves close to 1. Using this approach, we can limit the number of k values in each band to minimum 1 and maximum 7 while the accuracy of flux and heating rate is well maintained. The number of k terms obtained for each of the SES2 band is listed in the table 1. The total number of k terms for the SES2 is only 58. The same numbers in the SES1 and ES original scheme are 109 and 121, respectively. As a result, the SES2 should be more efficient than SES1 and ES schemes.

Figure 26. Comparison of net flux determined for $28750\text{-}50000\text{cm}^{-1}$ using 5 k term with those using 145 k term. The thick curves represent the results from 5 k terms while the thin lines denote those from 145 k term. The left panel shows results determined using method of ESFT and right panel gives the results from fit method. The right most curves show the total band fluxes.

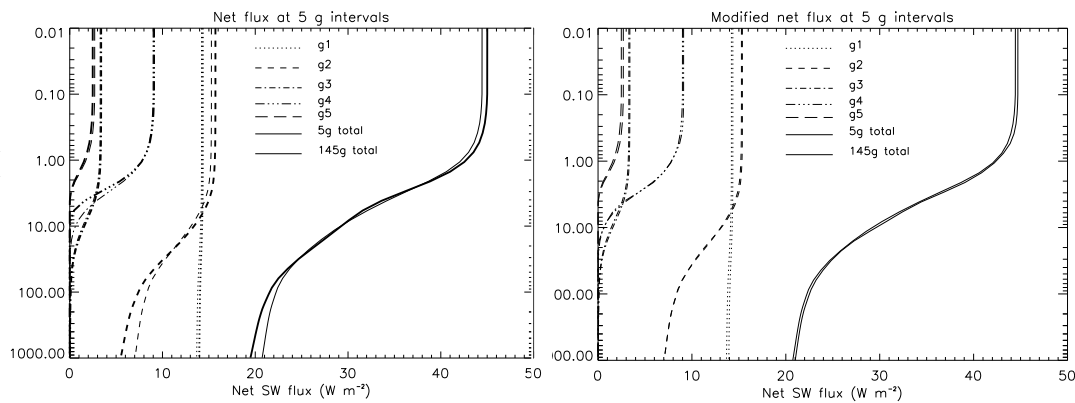
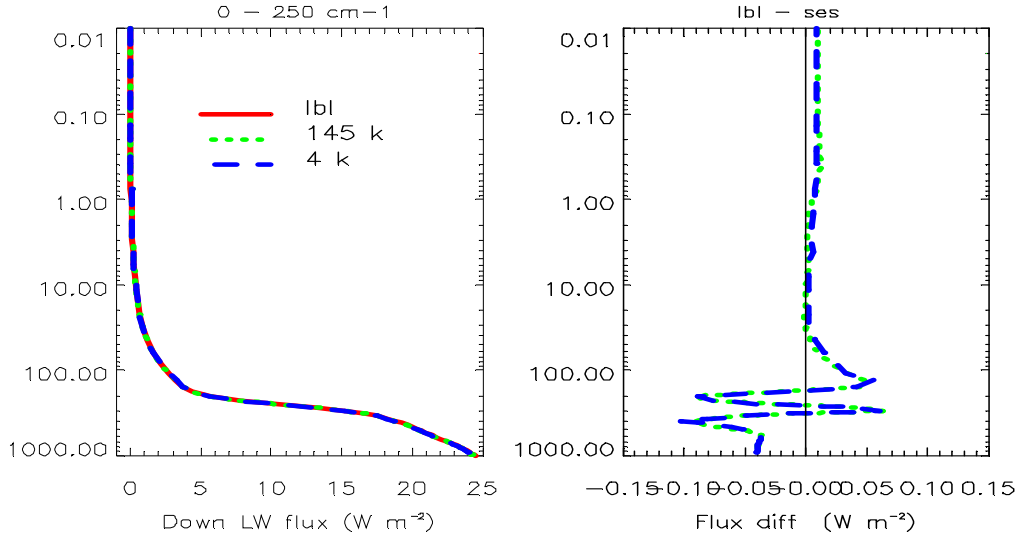


Figure 26 shows the flux profiles in each g interval for the shortwave spectral band $28750\text{-}50000\text{cm}^{-1}$ determined by the reference code using 145 k terms and the code with 5 k terms determined by ESFT with k values taken at the middle point in each interval (left panel) and by the fit method (right panel). The flux biases between reference and ESFT occur in all g intervals, but the values of bias are only larger in the last g interval. These biases are all reduced using the fit method, leading the total band fluxes to be in a good agreement with the reference results. Figure 27 shows heating profiles in a longwave spectral band $0\text{-}250\text{cm}^{-1}$. The fit method with only 4 k terms generates heating rate that is almost the same as that from using 145 k terms.

Figure 27. Longwave heating profiles determined by GENLN2 and two CKD models: one using 145 g intervals and one using 4 g intervals.



9. TREATMENT OF GASEOUS OVERLAPPING ABSORPTION

In some spectral bands, more than one significant absorbing species must be considered. The overlapping absorption by these species is treated in the same way as in the SES1 (Sun and Rikus, 1999) with some modifications necessary to the CKD model. For two absorbing species, the spectral optical depth is calculated by

$$\tau = k_1 u_1 + k_2 u_2, \quad (14)$$

where u_1 and u_2 represent the molecular absorber amounts for each species. In order to treat the two absorbing species as if a single one, we express the above optical depth by

$$\tau = k_m u_m, \quad (15)$$

where k_m represents the effective absorption coefficient for a binary species and u_m is a binary absorber amount defined by

$$u_m = u_1 + f u_2 \quad (16)$$

where f is a tunable parameter that maintains the contribution to the optical depth from u_2 in the same order of magnitude as that from u_1 (Sun and Rikus, 1999). Therefore, f can be simply defined as a ratio of the maximum absorber amounts of the two species, i.e.

$$f = \frac{u_1^{\max}}{u_2^{\max}}. \quad (17)$$

The effective absorption coefficient k_m can then be determined by

$$k_m = \frac{k_1 u_1 + k_2 u_2}{u_1 + f u_2}. \quad (18)$$

The dependence of k_m on the binary absorber amounts is determined by a linear interpolation of a binary parameter η defined by

$$\eta = \frac{u_1}{u_1 + f u_2} \quad (19)$$

For a fixed η value, this equation sets up a constraint that ensures that the absorber amount u_1 is fully correlated with u_2 . The u_m in Eq. (16) is then determined using this relationship to ensure that it is equivalent to a single species. A value of η near zero implies that the second species is dominant, whereas a value near 1 indicates that the first species is dominant. The values k_m for 9 η values equally spaced as 0, 1/8, 2/8, 3/8, ..., 1 are determined for all 59 reference pressures and 5 temperatures at each level and the results are stored as a look-up table for interpolation. To calculate optical depth for a mixture of the two species in a broadband model, one first calculates η from equation (19) and k_m is determined by linear interpolation from the stored values at reference η .

Substituting equation (19) to (18), we can see that

$$k_m = k_1 \eta + k_2 \frac{1 - \eta}{f}. \quad (20)$$

From this equation we obtain that

$$\tau_m = k_1 u_1 \quad \text{if } u_2 = 0$$

$$\tau_m = k_2 u_2 \quad \text{if } u_1 = 0$$

This indicates that the treatment for the binary species overlapping absorption meets the optical depth calculation for either single gas.

The above method is applied to the cases in which both absorbing species have significant absorption in a band, for example, CO₂ band in 15 μm and O₃ band in 9.6 μm. Therefore, the absorbing species in each band must be classified as either key or minor species. The classification of key and minor species in each of the SES2 band is also listed in table 1. The treatment of minor species is described in the next section.

10. TREATMENTS OF OTHER QUANTITIES IN CKD MODEL

10.1 Minor species

The species that has strong absorption in a band is defined as a key species and its effect on radiation is analyzed in detail. The CKD method and the method for dealing with overlapping absorption by the binary species described in the previous section are applied to these key species. Other species that have weak radiative effect are classified as minor species and the overlapping absorptions by these species are treated in a less precise way as suggested by Li and Barker (2005) and Zhang and Shi (2005). The k values for these minor species are sorted at the g space according to the position of that of key species sorted at the reference pressures and temperatures. Thus, the spectral correlation between the key species and minor species is maintained. The overlapping transmission by minor species is then accounted for in terms of a monochromatic way

$$T_{mix} = \sum_{i=1}^m w_i \exp[-(k_i^1 u_1 + k_i^2 u_2)]. \quad (21)$$

The results of radiative fluxes and heating rates are examined against the reference values after adding these minor species. If the differences are not acceptable then the k values for these species are adjusted using the same procedures as that for the key species.

10.2 Water vapour continuum

The water vapour continuum scheme of MT_CKD (Mlawer, personal communication) is used in both GENLN2 and SES2. As a usual practice, the effect of the foreign broadening continuum

absorption is included in the treatment of the water vapour line absorption. The self-continuum is treated separately. The absorption coefficients of the self-continuum component are calculated for 21 reference water vapour pressures ranged from 0 to 50 mbar in 2.5 mbar increment and 5 temperatures (180, 215, 250, 285, 320 K) for each reference vapour pressure. The results are used to determine the absorption coefficient corresponding to the real water vapour pressure and temperature by linear interpolation. Its contribution to the transmission is also treated using equation (21) with k values sorted according to the position of sorted water vapour line spectrum.

10.3 Planck function

The Planck function in the Edwards-Slingo scheme is determined by fitting the band average Planck function to temperature in terms of a polynomial function. In SES2, the band average Planck functions are pre-determined for 161 temperatures ranged from 180 to 340 K with 1 K increment. The Planck value at real temperature is then determined by linear interpolation using these reference values. The results have compared with those determined by polynomial function used in the Edwards-Slingo model and they are in a good agreement. But using the interpolation approach may be more efficient.

10.4 Oxygen collision induced continuum

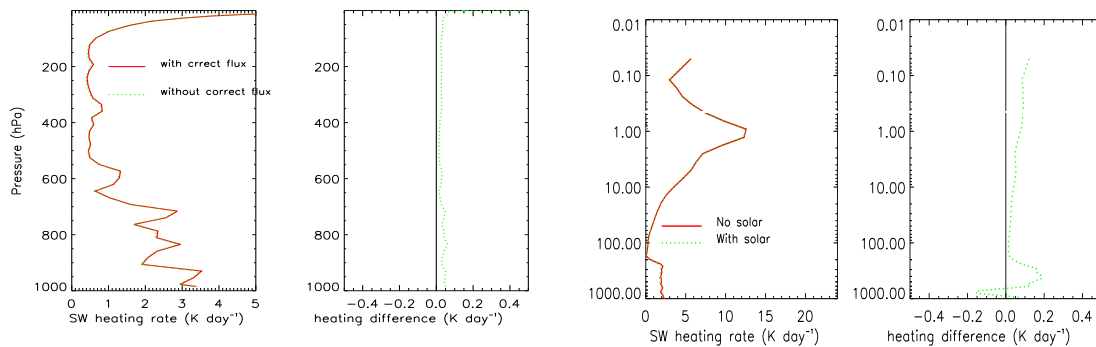
The oxygen collision induced continuum absorption cross-section data have been introduced in previous section. To implement this contribution to the SES2 broad-band model, the binary cross-section absorption data at 1.27 μm band are derived using the GENLN2 for three temperatures (200, 250, and 300 K). These data are sorted according to the position of the sorted spectrum for the key species in the band. The effect on the radiative transfer calculations is then considered in the same way as for the minor species. Again, a linear interpolation is used to determine the temperature dependent cross-sections in the model. The same procedure is applied to the other two spectral bands except that they have no temperature dependence.

10.5 Solar source function

Five solar source functions as mentioned in previous section are implemented into the SES2. The spectral distributions of these functions are also sorted according to the position of the k -distribution of the key species in a band. Instead of using a band averaged solar source at the

top of the atmosphere as used in the Edwards-Slingo model, the fraction of solar source fluxes in each g interval is worked out and used in the radiative transfer calculations.

Figure 28. The left two panels show the longwave heating rates and difference with and without solar source at the top of the atmosphere. The right panels show the heating rate and difference with and without adding solar tail flux to the last near infrared band.



10.6 Treatment of overlapping absorption of the solar and infrared

It is traditionally defined the solar spectrum as a region from 2500-50000 cm⁻¹, and the infrared spectrum from 0-2500 cm⁻¹. The spectral overlap between the solar and infrared is usually ignored because the fraction of solar flux in this region is small and its effect is not important (Liou, 1980). Such a division makes it possible to treat the radiative transfer and source functions separately for the two spectral regions and therefore simplify the solution in the radiative transfer. In the Edwards-Slingo code, this fraction of the solar energy is added to the last near-infrared band. This only makes the input total solar flux right at the top of the atmosphere. Since the absorption of the solar energy is spectral dependent, add this part of the energy to the other spectral region may not solve the problem. The solar flux in the overlap region 0-2500 cm⁻¹ is about 12 W m⁻², which is about 1% of the total solar energy. Li and Barker (2005) have discussed the effect of this issue. They included the effect of the solar energy in this region by imposing the additional solar flux in 0-2500 cm⁻¹ onto the downward flux for the appropriate infrared bands. This treatment is simple and natural and therefore adopted in the SES2. This is the reason that the longwave spectral file in SES2 scheme also contains the block of the solar source function. The influence of including this part of solar energy in both the longwave and shortwave radiation calculations is examined using SES2 and the results are shown in Figure 28. It is seen from the left two panels that adding the fraction of the solar energy to the last near-infrared band has a negligible effect on the heating rate. However, adding this fraction of energy to the longwave calculations has a noticeable effect on the heating rate, especially in the lower troposphere where extra heating rate is about 0.2 K day⁻¹.

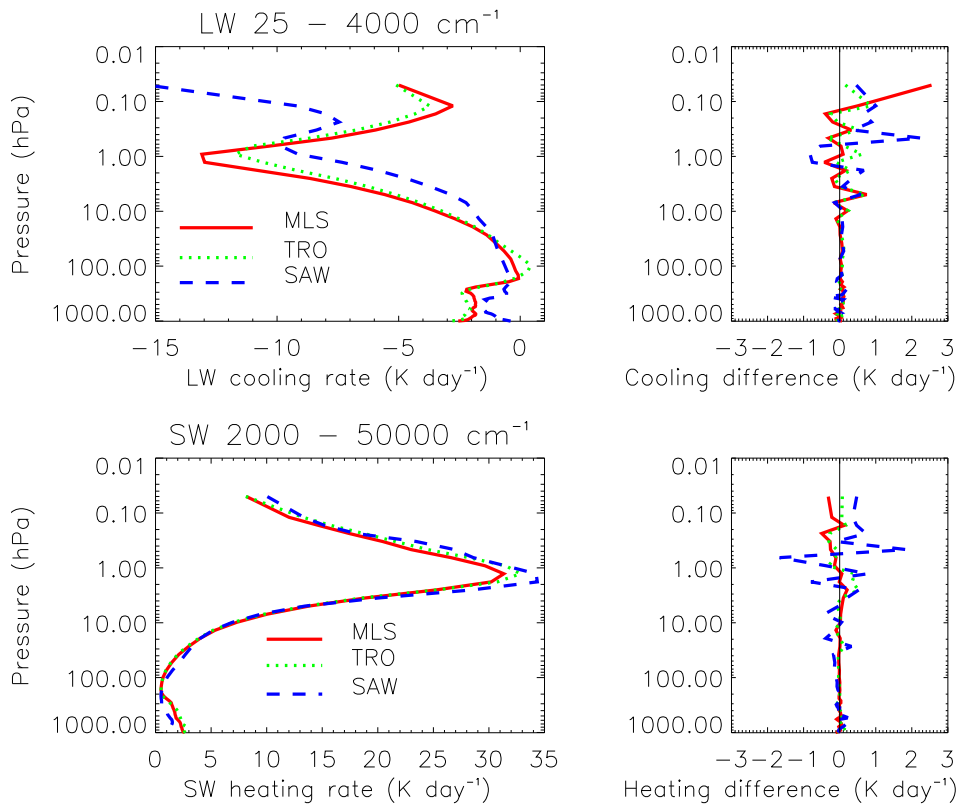
11. COMPARISONS OF SES2 WITH GENLN2, SES1 AND UKMO ES SCHEMES

The radiative flux and heating rates determined using the SES2 radiation scheme are compared with the reference results determined using the GENLN2, SES1 and the UKMO version of Edward Slingo radiation schemes. Figure 29 shows a comparison of longwave cooling and shortwave heating rates determined by SES2 and LBL. The calculations were performed for three atmospheres (mid-latitude summer, tropical and sub-arctic winter). In the shortwave calculations, a solar zenith angle of 30° and a surface albedo of 0.2 are used. The EAR version of the Kurucz solar source function is employed. The upper panels show the longwave results and the lower panels give the shortwave results. The left column presents the heating/cooling rates for the three atmospheres determined by the LBL scheme and the right column shows the errors of SES2 relative to LBL. It is seen that the SES2 produces more accurate heating/cooling rates in troposphere for the pressure level below 10 hPa with the errors being less than 0.5 k d^{-1} . The errors of less than 1 k d^{-1} occur above 10 hPa for the mid-latitude summer and tropical atmospheres. The errors at upper levels for the sub-arctic winter atmosphere are slightly large, reaching to about 2 k d^{-1} . This reveals a possible problem when using the equation 12 to determine the representative k values in each interval based on the calculations for the mid-latitude summer atmosphere only. A further investigation will be conducted to find out the reason why the errors for the cold atmosphere are relatively large. Nevertheless, the results are still considered as accurate at this pressure level because the absolute heating/cooling rates are very large here and therefore the relative errors are still very small.

The shortwave comparison of SES2 with SES1 and LBL is shown in Figure 30. Note that the absorptions due to O_2 , CH_4 , and N_2O are included in the GENLN2 and SES2 calculations but not in the SES1 and therefore this comparison actually reveal the contributions of these species to the radiative transfer in the atmosphere. It is seen that neglect of these three species in the SES1 calculation leads to an overestimate of the downward solar flux at the surface by about 6 W m^{-2} and an underestimate of the solar heating rate in stratosphere by about 2 k d^{-1} . This result indicates that the radiative effects of these species are important and should be included in the shortwave calculations.

The results determined by SES2 are further compared with those from Edwards-Slingo schemes and the shortwave results are shown in Figure 31. It is seen that both the downward and upward solar radiative fluxes generated by the Edwards-Slingo scheme are higher than those determined by LBL and SES2. The downward flux is overestimated by about 15 W m^{-2} and the upward flux overestimated by 5 W m^{-2} . The heating rate above 10 hPa, however is underestimated. There are a couple of reasons for these discrepancies. One of them is the omission of absorption by CH_4 , N_2O and water vapour continuum which are all included in the LBL and SES2 schemes and these can reduce the downward flux at the surface by about 2 W m^{-2} . The second reason may attribute to neglecting the absorption of solar radiation in the spectral region between $100 \sim 2000 \text{ cm}^{-1}$, which causes a difference of about 6 W m^{-2} . The third fact may be due to the use of different ozone absorption cross-section data. The fourth fact may be due to the difference in the treatment of transmission calculation. It may be worth to note that the shortwave absorptions due to CH_4 and N_2O have been absent from the all shortwave radiation schemes participated to the IPCC AR4 assessment and it has been suggested that they should be included in the IPCC fifth assessment (Collins *et al.*, 2006). This indicates that the

Figure 29. Comparison of radiative heating/cooling rates determined by LBL and SES2 radiation schemes for three atmospheres. The shortwave calculations assume a solar zenith angle of 30° and a surface albedo of 0.2. The left panels show heating/cooling from LBL calculations and the right panels show the errors of SES2 relative to LBL.



SES2 has been well ahead of most shortwave radiation codes in this regard and already meet the need for the next IPCC assessment. Figure 32 shows a longwave comparison. It is seen that the agreement between SES2 and Edwards-Slingo schemes is better than the shortwave. The upward flux determined by the Edwards-Slingo scheme is even better than SES2 although the downward flux and cooling rate are still slightly worse.

Figure 30. Comparison of the shortwave results determined using the SES2 with those from the LBL and SES1 for mid-latitude summer atmosphere. The calculations assume a solar zenith angle of 30° and a surface albedo of 0.2.

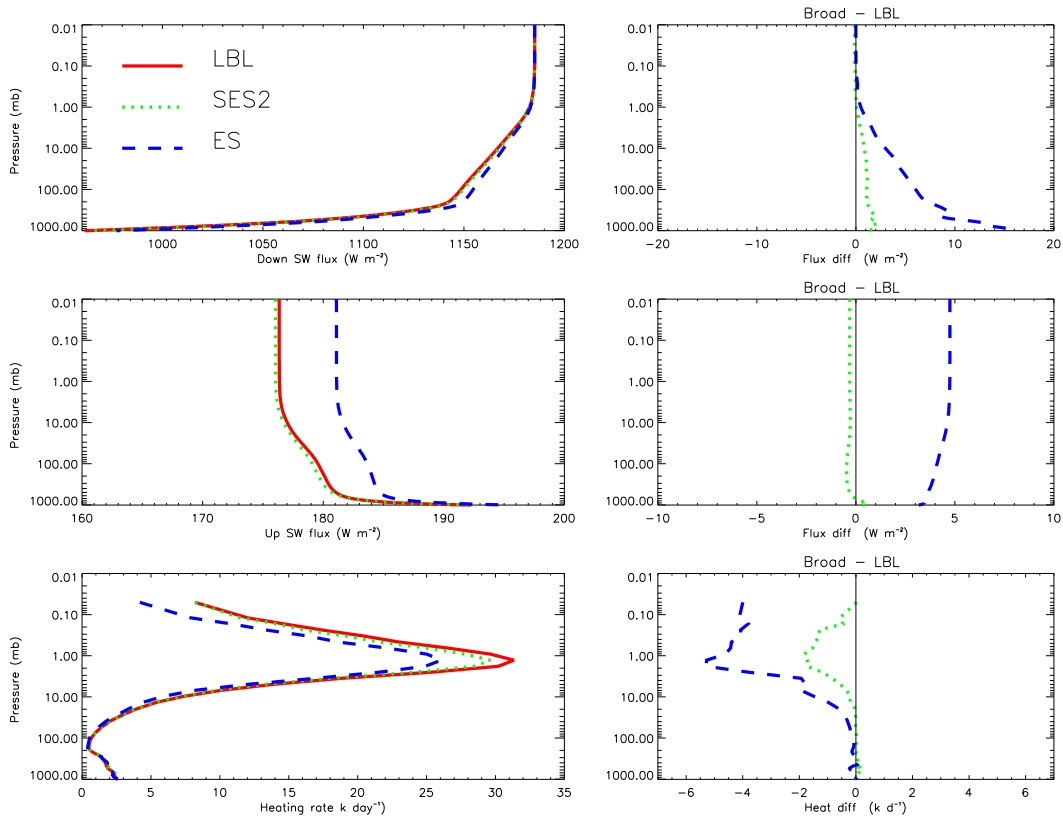


Figure 31. Comparison of shortwave results determined by LBL, SES2 and Edwards-Slingo radiation schemes. The calculations use MLS atmosphere with a solar zenith angle of 30° and surface albedo of 0.2.

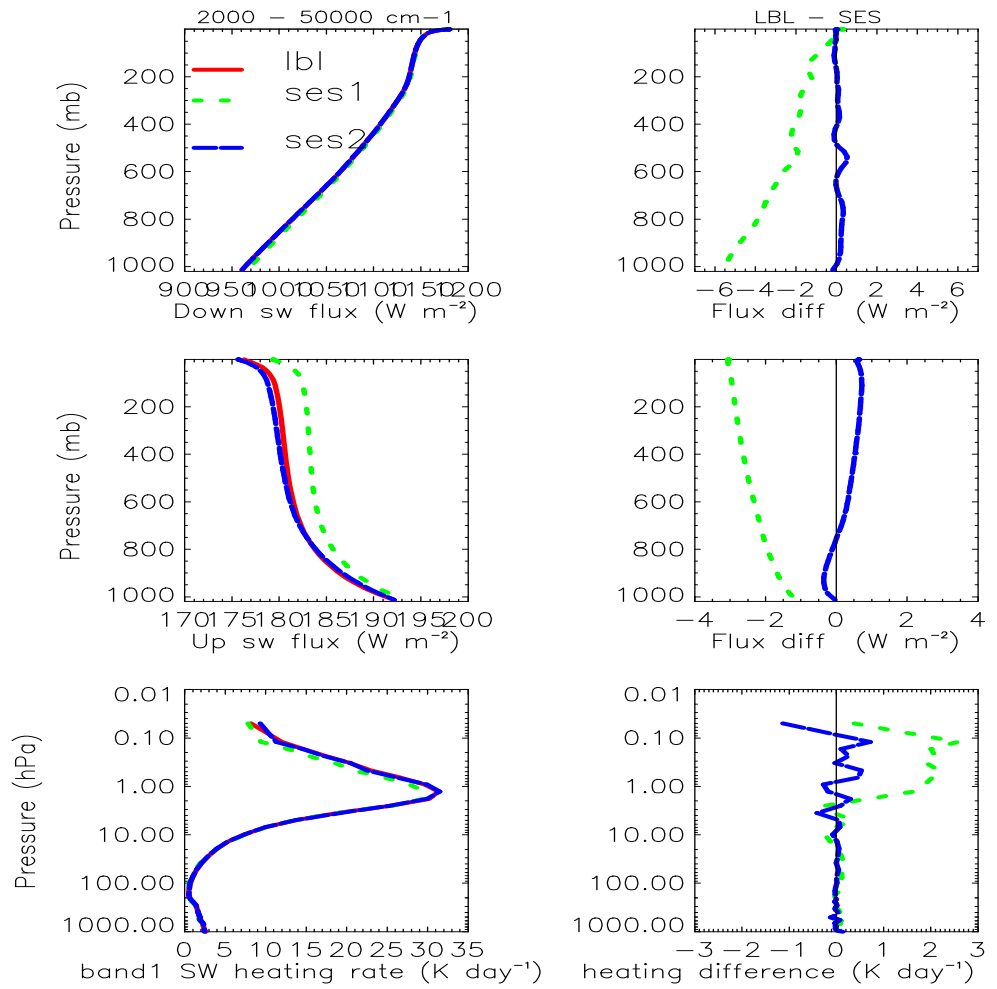
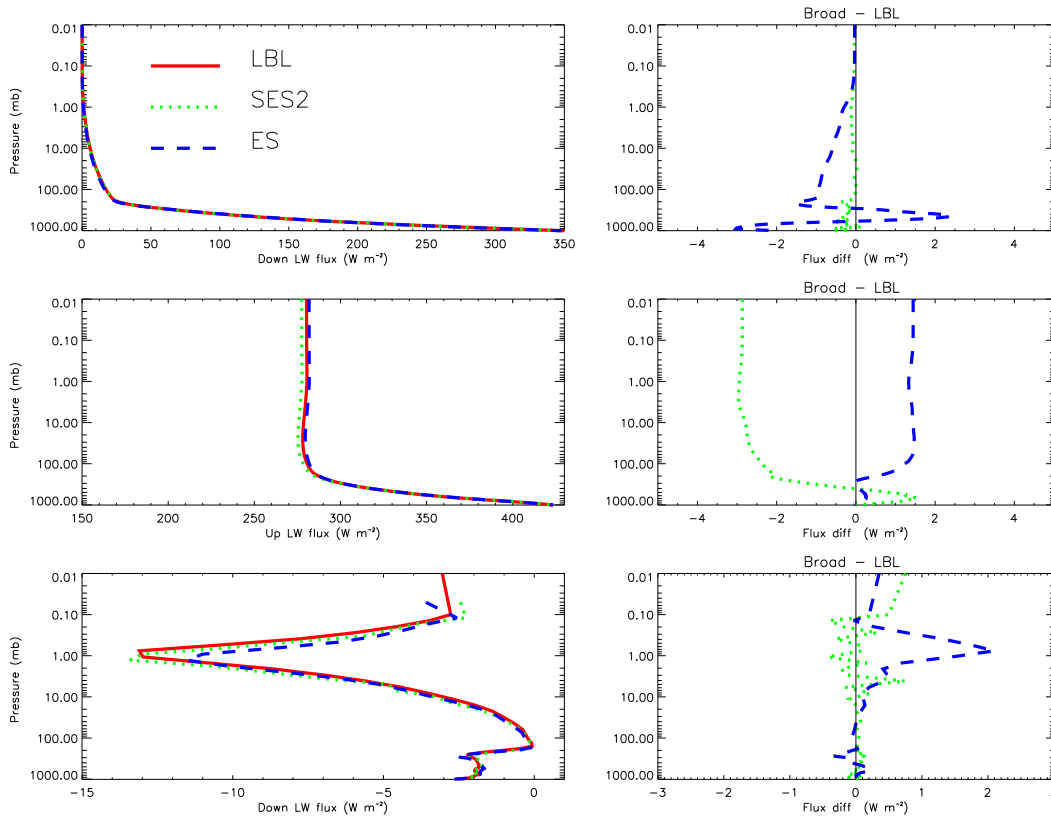


Figure 32. Comparison of longwave radiative results determined by LBL, SES2 and Edwards-Slingo schemes for MLS atmosphere.



12. FAST SCHEME FOR SURFACE RADIATION BUDGET (SURFLX)

A Fast scheme for determining global and net solar radiation at the Surface (SURFLX) is under development based on SES2 scheme. The reason for developing such a scheme is to enable the surface radiation budget calculation to be carried out at each model integration time step in order to improve the model land surface process. The radiation is computationally time-consuming to model and therefore its calculation in most NWP and climate models is only performed at very low frequency. The model integration time step is usually in the range 450 to 720 seconds but the radiation frequency is often set to a 2-3 hour interval. The radiative heating in the atmosphere and radiation budget at the surface are therefore not updated between the two radiation time intervals. This is an unsolved problem and may lead to incorrect land surface processes. Apart from the radiative heating/cooling effect in the atmosphere, the important

influence of radiation on convection and precipitation is its impact on the surface processes. The radiation absorbed by the earth surface is transformed to the sensible, latent and soil heat fluxes. If the diurnal cycle of the absorbed solar energy at the surface is not well represented in the model simulations the sensible and latent heat flux calculations will not be correct, which in turn will influence the development of convection and precipitation. In order to improve the model surface processes, the radiation budget at the surface between the two radiation time steps should be corrected to allow for variation between radiation calculations. However, it is hard to do this by a simple interpolation because there are usually rapid changes in atmospheric conditions, especially when there are clouds present. Therefore it may be desirable to develop an appropriate method that can be used to accurately determine the surface radiation budget at a high temporal frequency (e.g. each model time-step).

Such a scheme is currently under development based entirely on the SES2 full radiation calculations. The reason is twofold. First, the scheme is used in the global model and the results must be consistent with those determined using the full radiative transfer model. Second, such a scheme can be easily validated using most available field observations and therefore provides inherited validation back to the SES2 scheme.

The development has been completed for the clear sky condition and the details can be found in Sun *et al.*, (2007).

13. EVALUATIONS OF SES2 IN BMRC ATMOSPHERIC MODEL (BAM)

13.1 Comparison of radiation fields with satellite measurements

The performance of SES2 in the BAM model is first assessed by comparing the modeled radiation fields with satellite measurements for the clear sky condition. The monthly mean clear sky radiation fields at the TOA determined by CERES satellites for January 2001 are used as a benchmark. The BAM 5.0 model was run in the climate mode for three cases:

- Control run: operational radiation codes (Fels-Schwarzkopf longwave and Lacis-Hansen shortwave) were used and the results are represented as FS.
- Experiment 1: SES1 was used
- Experiment 2: SES2 was used

Figure 33 shows the clear sky upward shortwave radiative flux at TOA in January 2001 determined by the CERES satellites and BAM model. The distribution patterns of modeled

results are in a reasonable agreement with observations. But the results of SES2 are better than those of FS and SES1. This can be seen in the reflected flux in mid-high latitude regions in southern hemisphere where the results from the SES2 are closer to the observations whereas those from the FS and SES1 are overestimated. The improved results from SES2 can also be seen in South America and Australia.

Figure 33. Clear sky reflected shortwave flux at the top of atmosphere determined by CERES satellite and BAM model for January 2001. Top left panel: CERES; top right panel: FS; bottom left panel: SES1; bottom right: SES2.

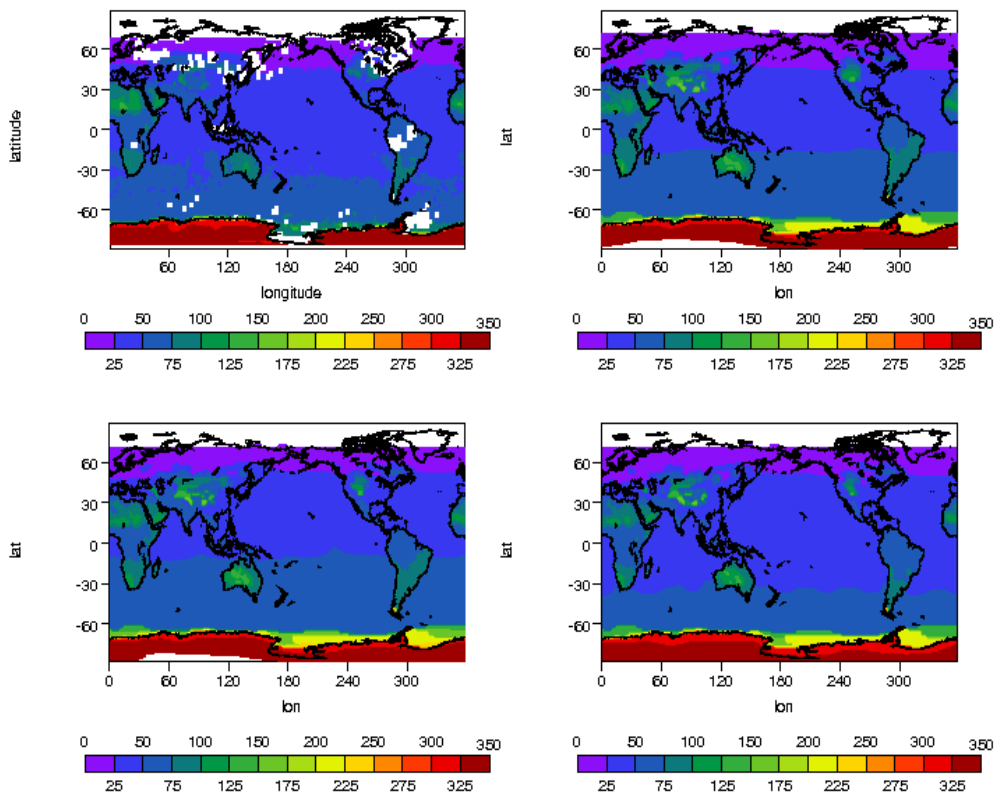
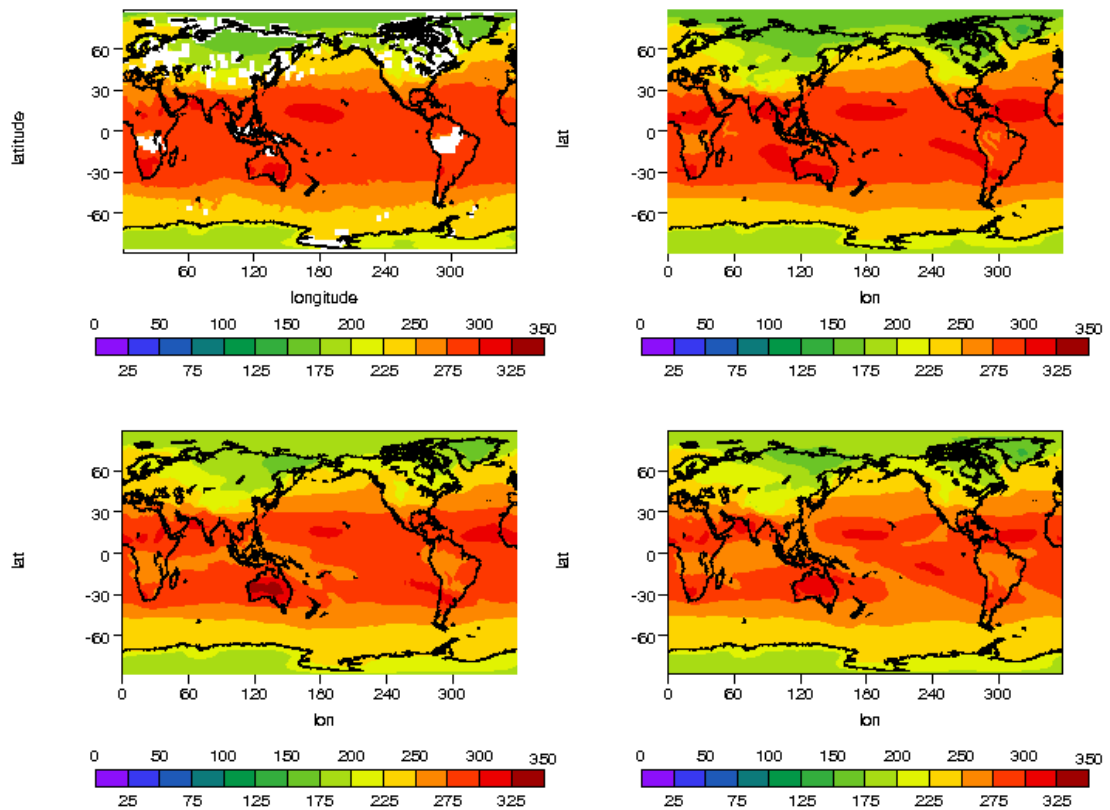


Figure 34 shows the comparison of clear sky OLR. It is seen in this figure that OLR determined by FS scheme is closer to the CERES observation. A low OLR belt is produced by both SES1 and SES2 schemes along convective regions such as ITCZ, Asia Monsoon region and South Pacific convective zone while the results from CERES satellite do not show this signature. These discrepancies raise a question on whether the errors are in the model or in the measurements. This question has been discussed by early studies carried out by other researchers. Slingo *et al.*, (1998) conducted model-satellite clear sky OLR comparison using the Edwards-Slingo radiation scheme with input data from 15-year ECMWF reanalysis and ERBE clear sky-OLR. Their results are very similar to what we found here, i.e. over convective regions such as the ITCZ the simulated clear-sky OLR is lower than that from ERBE by between 5 and 20 $W m^{-2}$. Their investigations have led to a conclusion that the problem is likely due to the ERBE scene identification. Collins and Inamdar (1995) also argued that the ERBE

bias results from problems with the scene identification algorithm. In particular, at high humidities the algorithm could incorrectly classify low values of the clear-sky OLR as originating in cloud and so exclude them from the clear-sky diagnostic. Since the convective zone due to the ITCZ cannot be seen from the CERES clear-OLR, the same bias may have also applied to this quantity. Thus, the poor comparison of clear-sky OLR between the CERES and SES2 simulation may be due to the uncertainty in the observations.

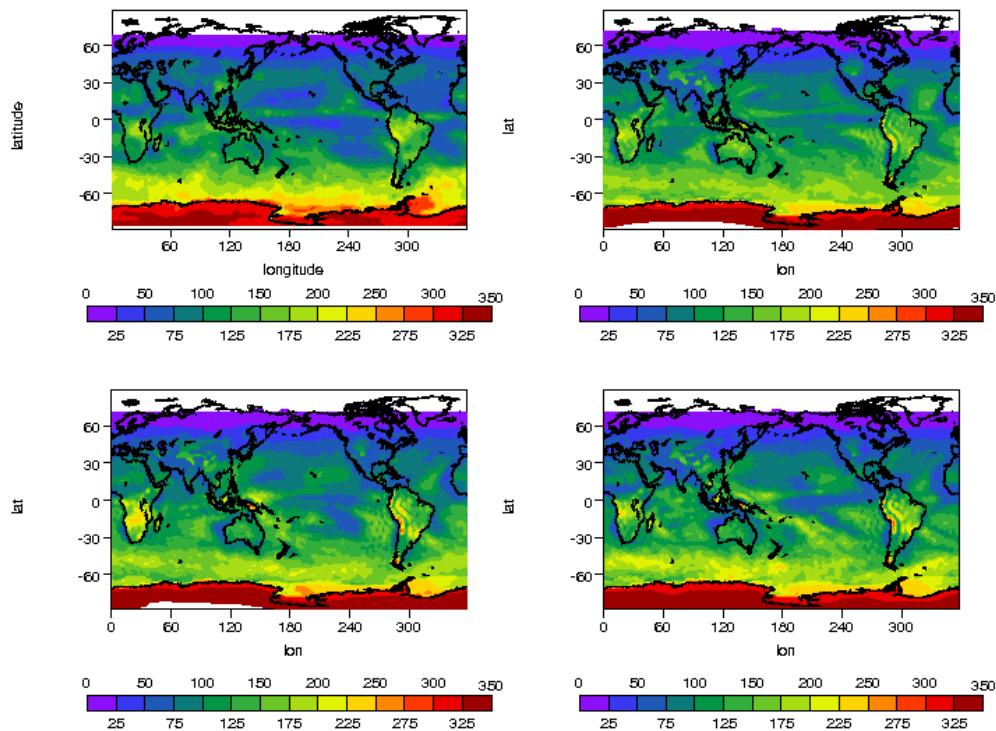
Figure 34. Clear-sky OLR determined by CERES satellite and Bam model for January 2001. Top left panel: CERES; top right panel: FS; bottom left panel: SES1; bottom right: SES2.



The monthly mean all-sky reflected shortwave flux at TOA determined by CERES satellite and BAM simulation is presented in Figure 35. Although the distribution patterns from three radiation schemes are all similar to that of CERES, some differences can still be identified. The modeled results by SES1 in the south America is higher than CERES. The results over the Central Pacific Ocean determined by both FS and SES1 schemes are overestimated. In general, the SES2 provides relatively better results compared with CERES observations.

The comparison for the monthly OLR is given in Figure 36. The distribution patterns of the OLR simulation from three radiation schemes are similar to that of the CERES observation. But the results over the convective regions, southern hemisphere ocean and South Africa from SES1 are lower than those of the CERES, indicating overestimate effect of clouds. The results from FS scheme, however, are opposite, i.e. the OLR in these regions are higher than the CERES observation. In contrast, the SES2 improves the simulations in these regions although the effects of cloud over the tropical region are still overestimated.

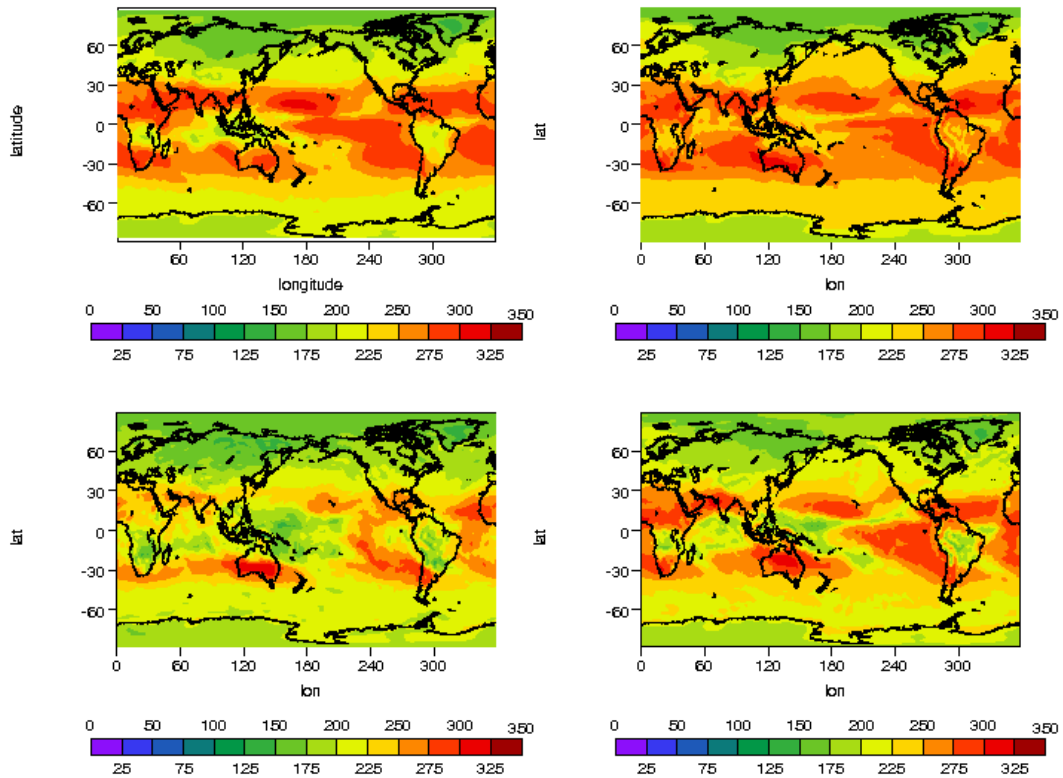
Figure 35. All-sky reflected shortwave flux at TOA determined by CERES satellite and BAM model for January 2001. Top left panel: CERES; top right panel: FS; bottom left panel: SES1; bottom right: SES2.



13.2 Ten year AGCM integration

The SES2 scheme is further assessed by performing 10 year Atmospheric Model Intercomparison Project (AMIP) experiment, commencing in January 1979, through until December 1988. An initial condition with 60 vertical levels in January 1979 is used. Prognostic cloud scheme developed by Rotstajn (1997), a new land surface scheme developed at ECMWF and a new convection scheme from ECMWF are used in the calculations.

Figure 36. All-sky OLR determined by CERES satellite and BAM model for January 2001. Top left panel: CERES; top right panel: FS; bottom left panel: SES1; bottom right: SES2.



13.2.1 Cloud radiative forcing

Figures 37 - 38 show the comparison of zonal mean distribution of longwave, shortwave and total forcing determined by the model and the Earth Radiation Budget Experiment (ERBE) observations. In both January and July, the model derived longwave forcing agrees well with the observations over the tropical regions, but the forcing is underestimated in middle-high latitudes. The modelled shortwave forcing compares well with observations too in both months except in higher latitudes regions around $\pm 60^\circ$ where the shortwave forcing is underestimated. This deficiency also occurs in the early experiments performed using BAM 3.0 (Colman *et al.*, 2005). Biases in the total forcing are very similar to that of the shortwave forcing, indicating domination of the shortwave forcing.

In the horizontal distribution (Figure 39-40), the model errors are very similar to those from the BAM 3.0 run (Colman *et al.*, 2005). However, improvements in certain areas can be seen from the error distributions. In January, for example, the negative longwave forcing errors in the Indian Ocean and over the maritime continents and the positive errors in the tropical Western Pacific are reduced. While the bias around the Northern hemisphere middle-latitude

are increased the bias further north around 60 degree are substantially reduced. In July, strong positive bias in the tropical Indian and Western Pacific Ocean in the BAM 3.0 model are significantly reduced, but again, the negative bias in middle-high latitudes are increased.

The negative bias in shortwave forcing over the tropical regions in both January and July (Figure 41-42) are much smaller compared with the results determined using BAM 3.0 (Colman *et al.*, 2005). But marked positive bias in high latitudes still exist which contribute significant zonal bias shown in Figure 37-38.

Figure 37. Comparisons of the ERBE and SES2 for zonal mean cloud longwave forcing (top panel), shortwave forcing (middle panel) and total forcing (low panel) in January.

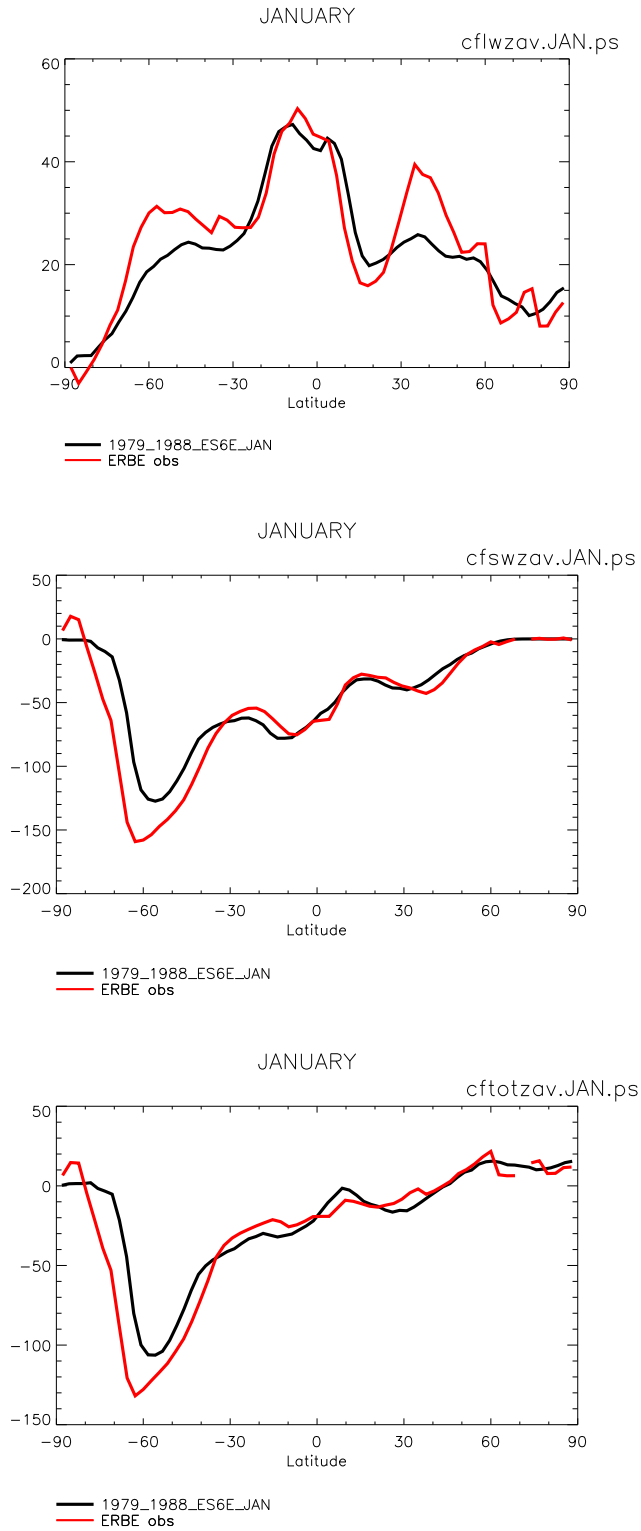


Figure 38. Same as Figure 37 but for July.

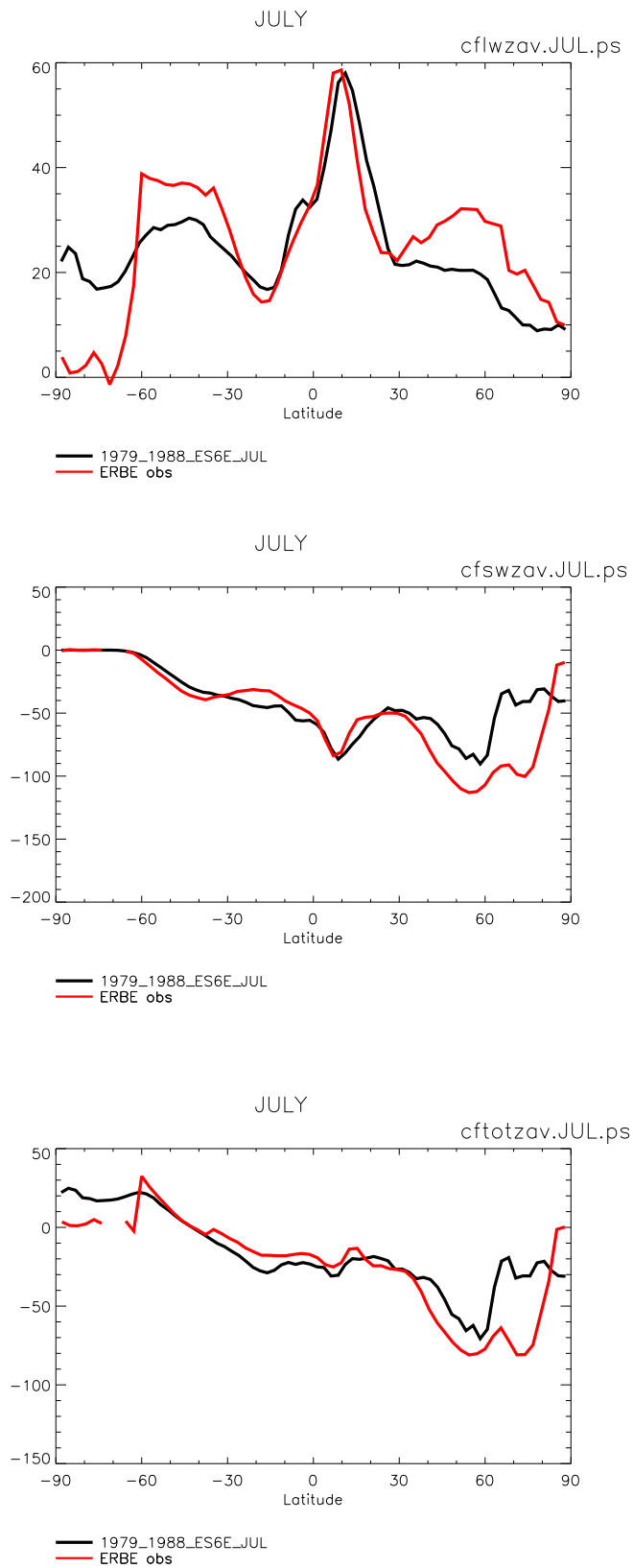


Figure 39. Horizontal distribution of cloud longwave forcing determined by ERBE and BAM model in January.

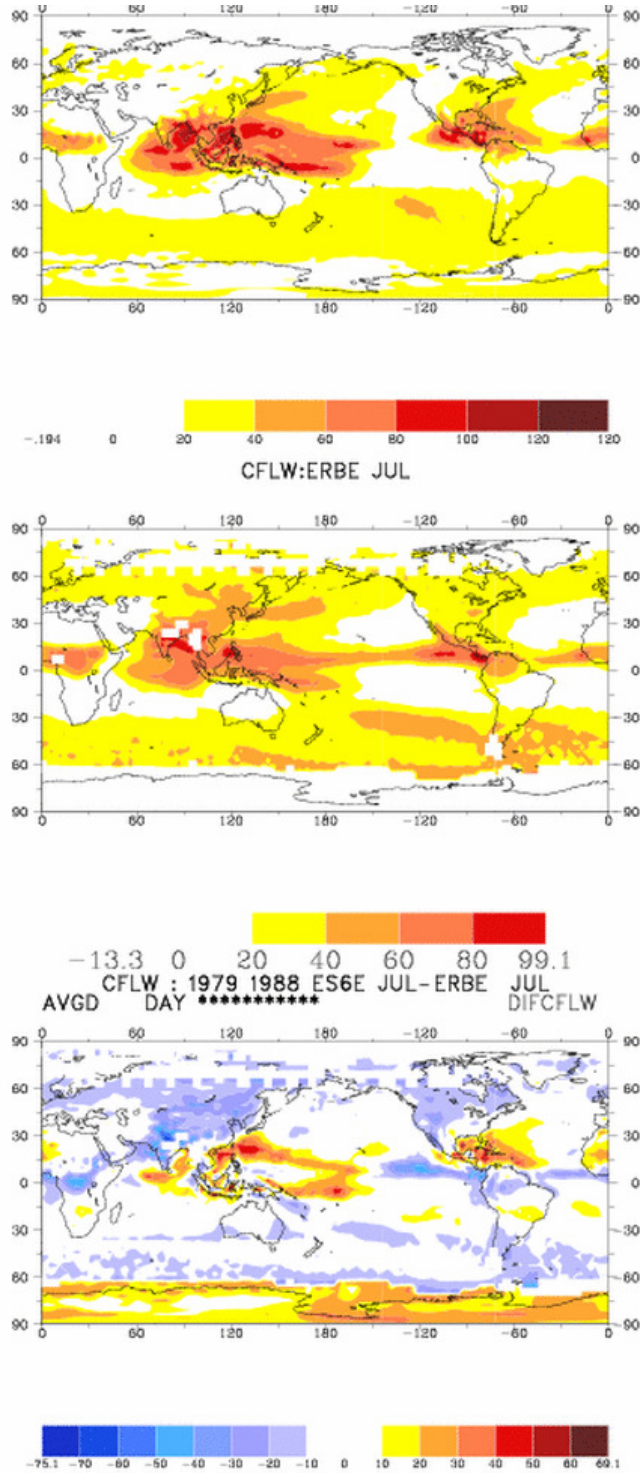


Figure 40. As for Figure 39, but for July.

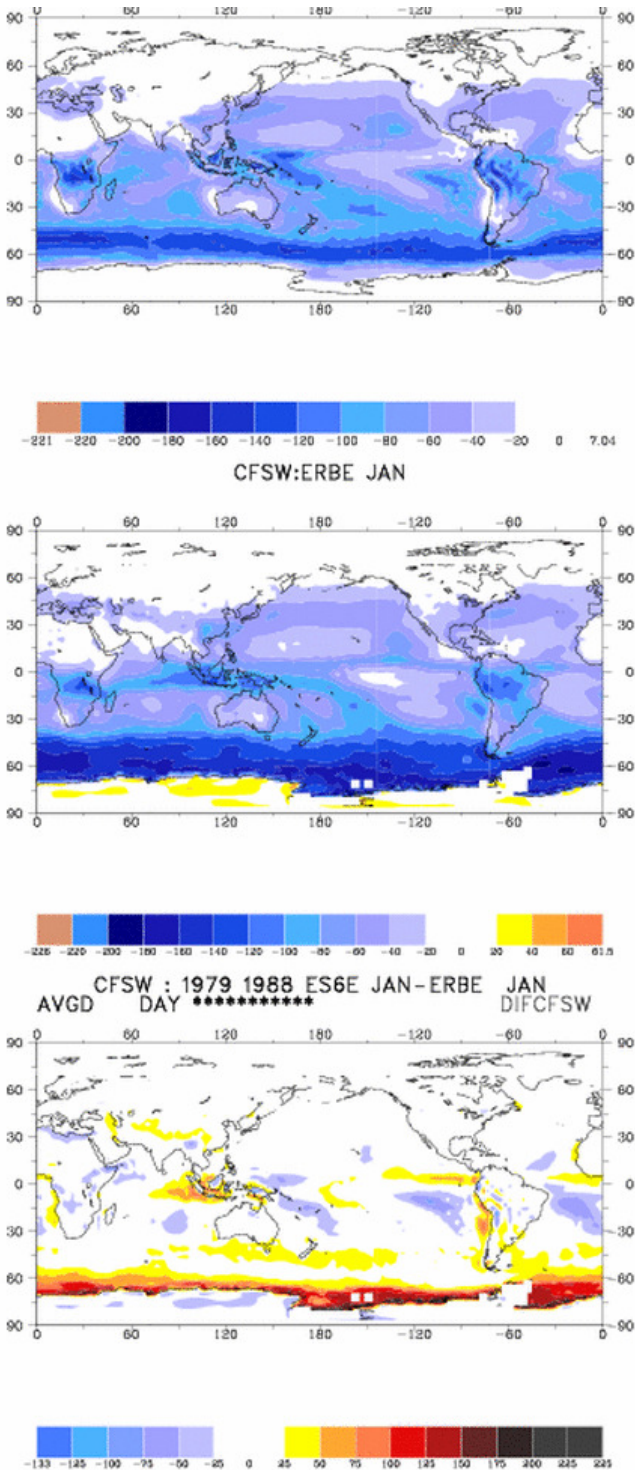


Figure 41. Horizontal distribution of cloud shortwave forcing determined by ERBE and Bam model in January.

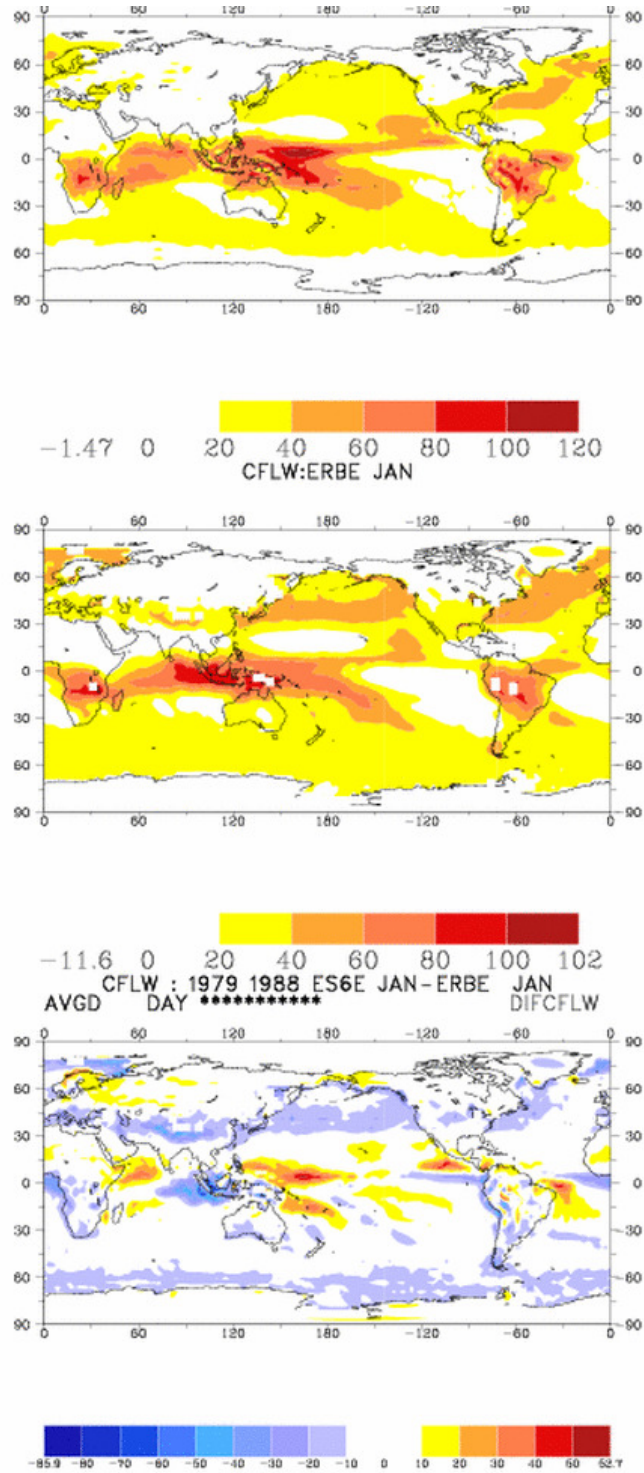
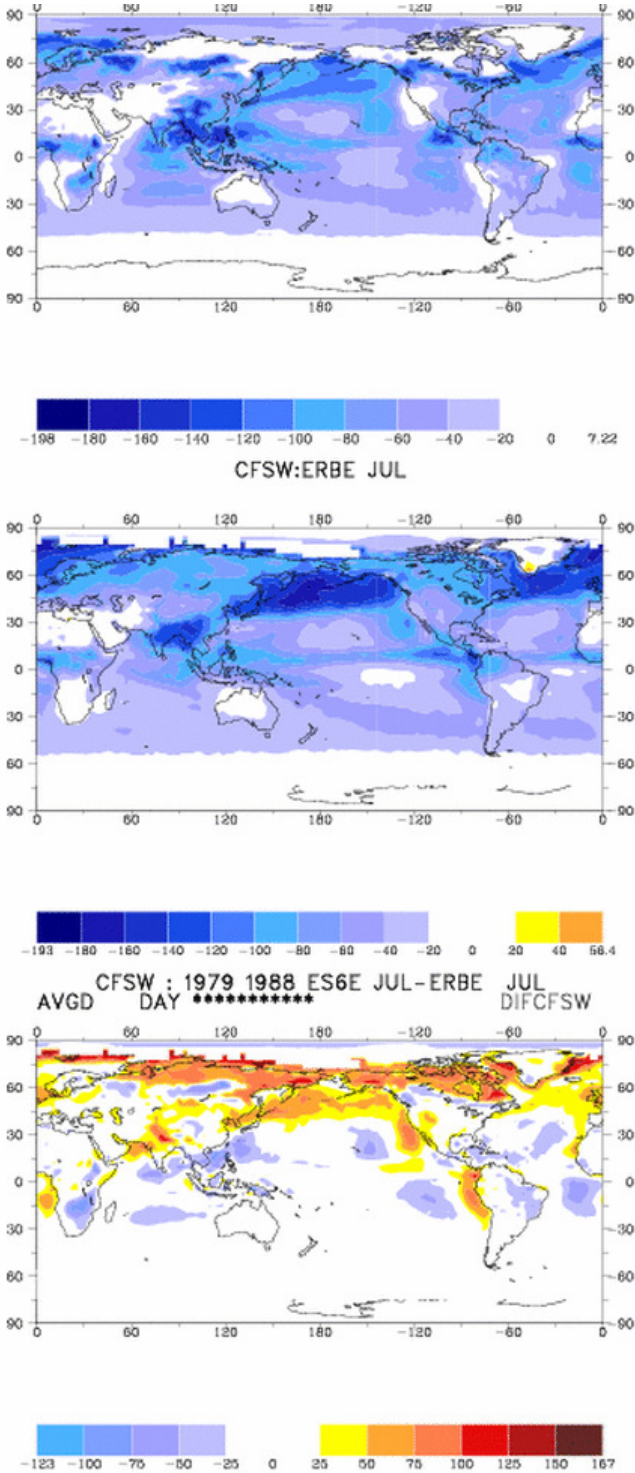


Figure 42. As for Figure 41 but for July.



13.2.2 Precipitation

Figure 43 – 44 show precipitation for two months. The observations of Xie and Arkin (1996) are used for comparison. For the zonal and horizontal distributions, the overall patterns in the model are generally good. All features captured by the BAM 3.0 (Figure 7.1 and 7.2 in Colman *et al.*, 2005) are maintained in current experiment. Furthermore, the positive bias along the ITCZ in January in the BAM 3.0 experiment are substantially reduced that lead to a much better zonal mean comparison over the tropical region. The improvement in July is also apparent, especially in the northern hemisphere. The slightly shift peak in the BAM 3.0 simulation has been corrected and a better comparison in the middle-high latitudes is obtained.

13.2.3 Zonal mean temperature

The modelled zonal mean temperature is compared with the National Centers for Environmental Prediction (NCEP) reanalysis. Figure 45 - 46 shows the results. The modelled temperature in January compares well with the NCEP data throughout the atmosphere over the tropic and sub-tropical regions except around 100 hPa where warm bias between 3 and 6 °C occur. Above 300 hPa, cold biases occur over the North Pole. Over the South Pole, cold biases occur in three vertical layers: from the surface to 600 hPa; 300 hPa to 150 hPa, and from 40 hPa to 10 hPa. In contrast, the bias patterns are very different in July. The cold biases occur below 150 hPa at northern high latitudes and pole region. Above 30 hPa level, another cold bias extends from the North Pole to the southern middle-latitudes. Strong warm bias occurs at the top level in southern high latitudes and it shifts toward mid-latitude downward. Another warm bias happens at low troposphere over the South Pole.

Compared with the BAM 3.0 simulations, the temperature fields from the current experiment have significant improvement in two areas. The warm biases in the upper tropical atmosphere disappear and large cold biases over the polar regions are reduced.

It must be emphasized that the improvements from the current experiment relative to the BAM 3.0 experiment are not only attributed to the new radiation but also other physical changes as well as changes in the vertical resolution. In order to make a clean comparison to assess the impact due to the change in radiation only, the same AMIP runs have been performed using the radiation schemes of FS and SES1. The results have shown some advantages from the SES2 schemes. But these comparisons are not included in this report for reduction of the paper length.

Figure 43. January precipitation for (a) model, (b) observations, (c) model minus observations and (d) zonal mean of model and observations. Units: mm/day

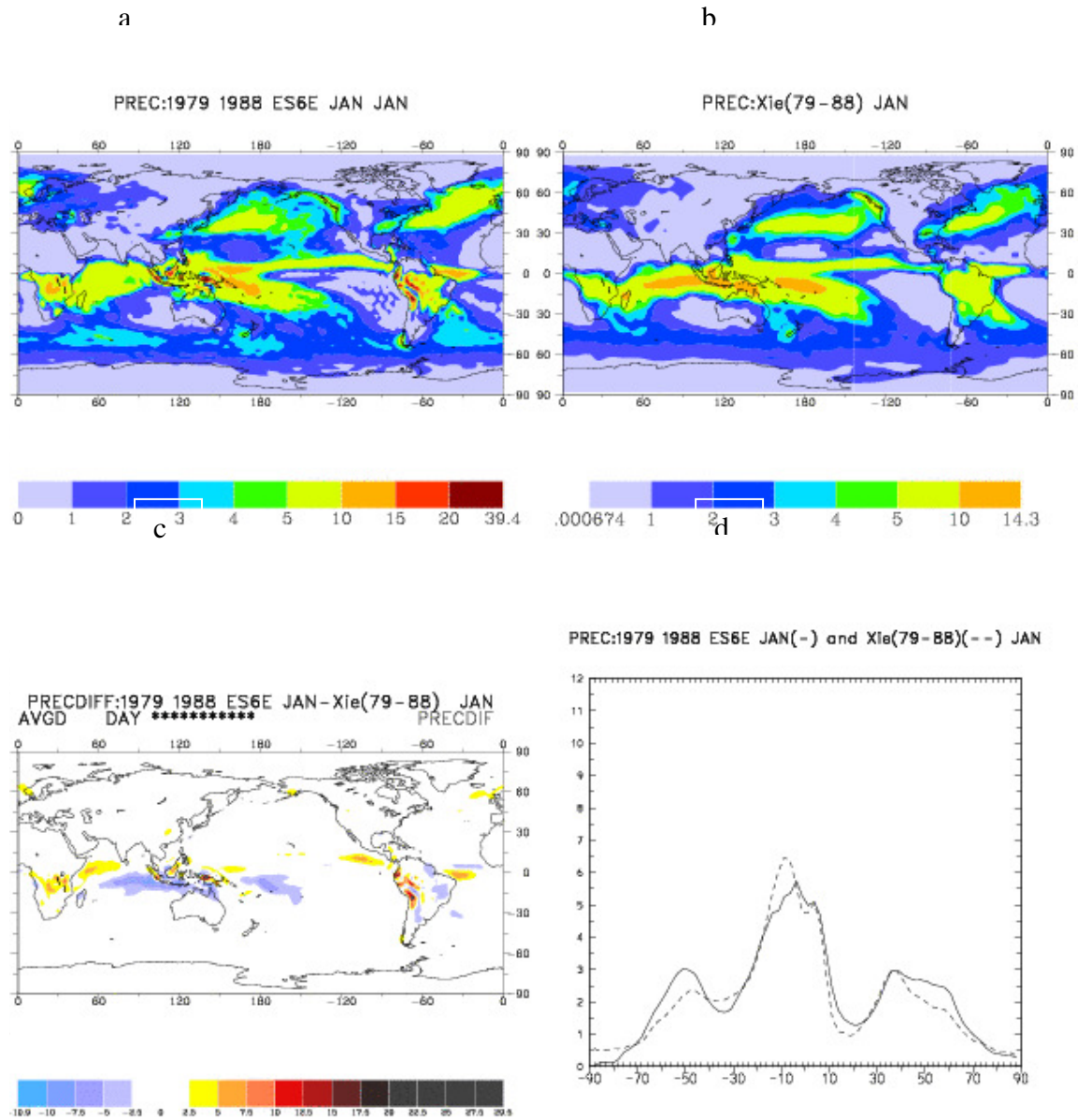


Figure 44. As for Figure 43, but for July.

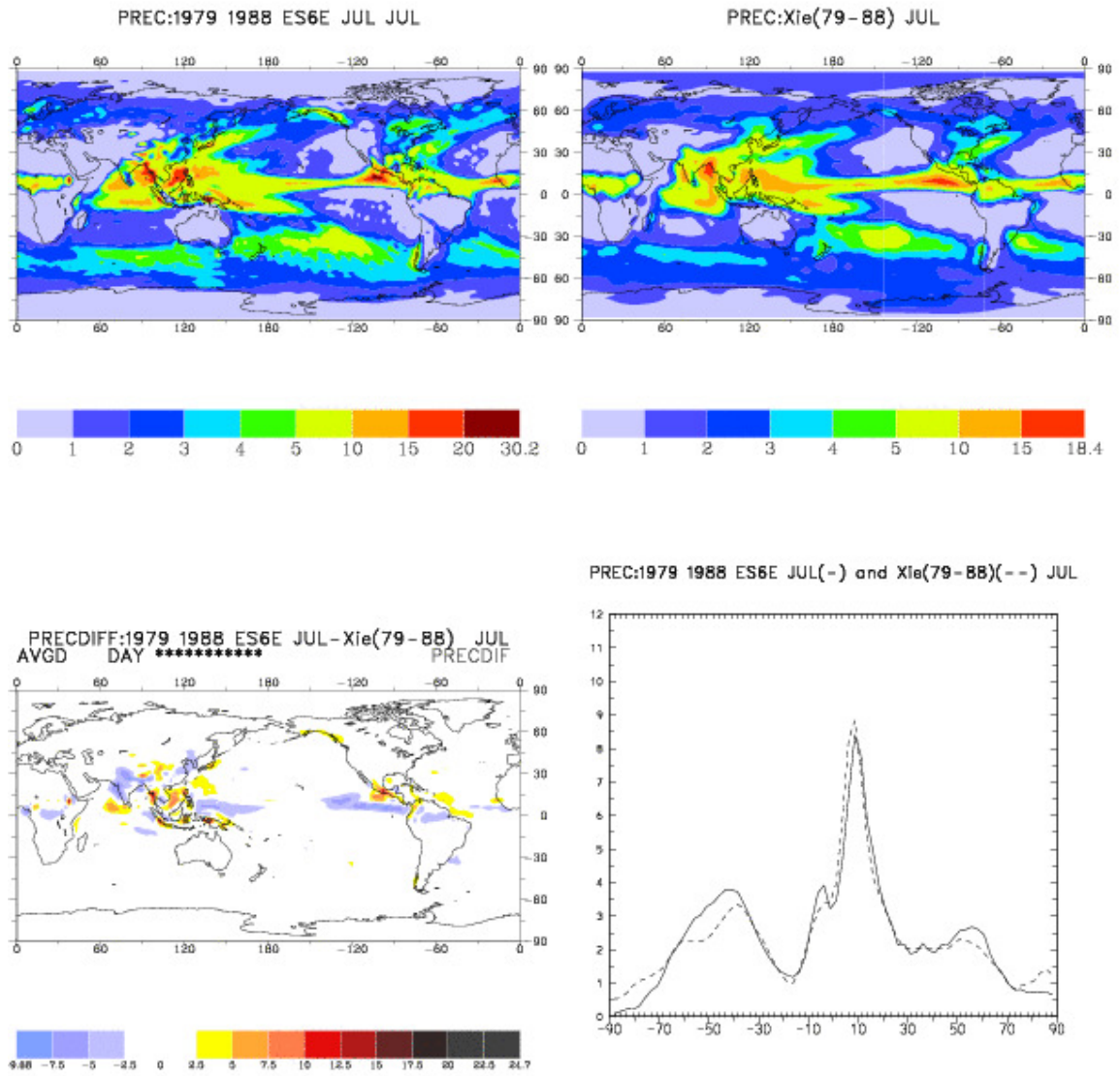


Figure 45. January, zonal mean temperature for: (a) model, (b) NCEP, and (c) model minus NCEP. Units: °C.

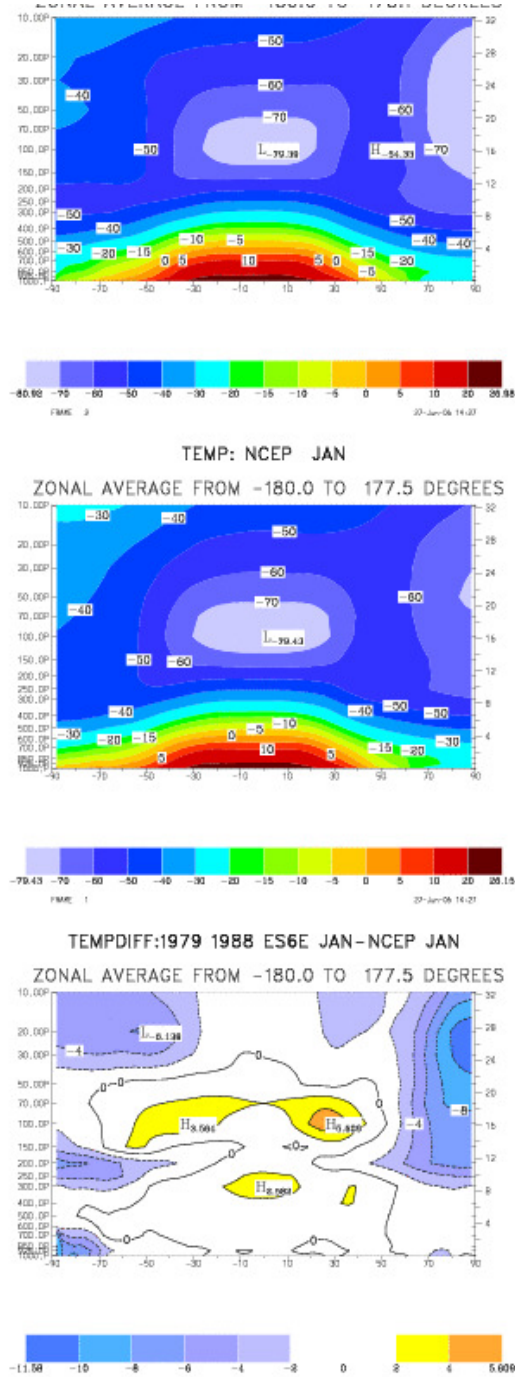


Figure 46. Same as Figure 45, but for July

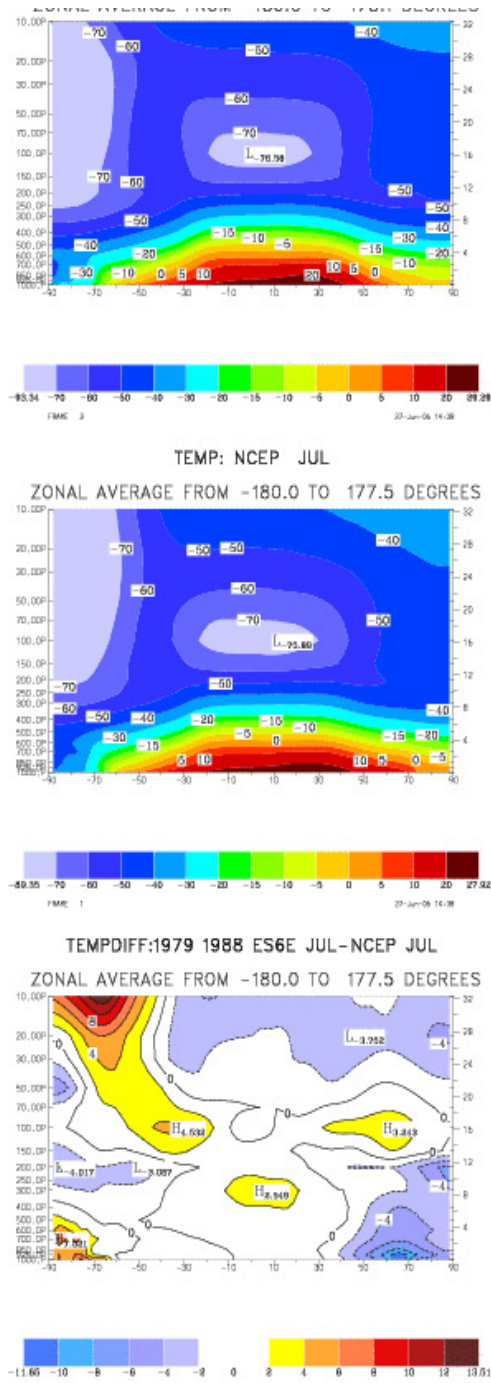


Figure 47. Verification of MSLP in tropics. Red curve is from the control run; green is from SES2 with cld93 scheme and blue is from the SES2 with prognostic cloud scheme;

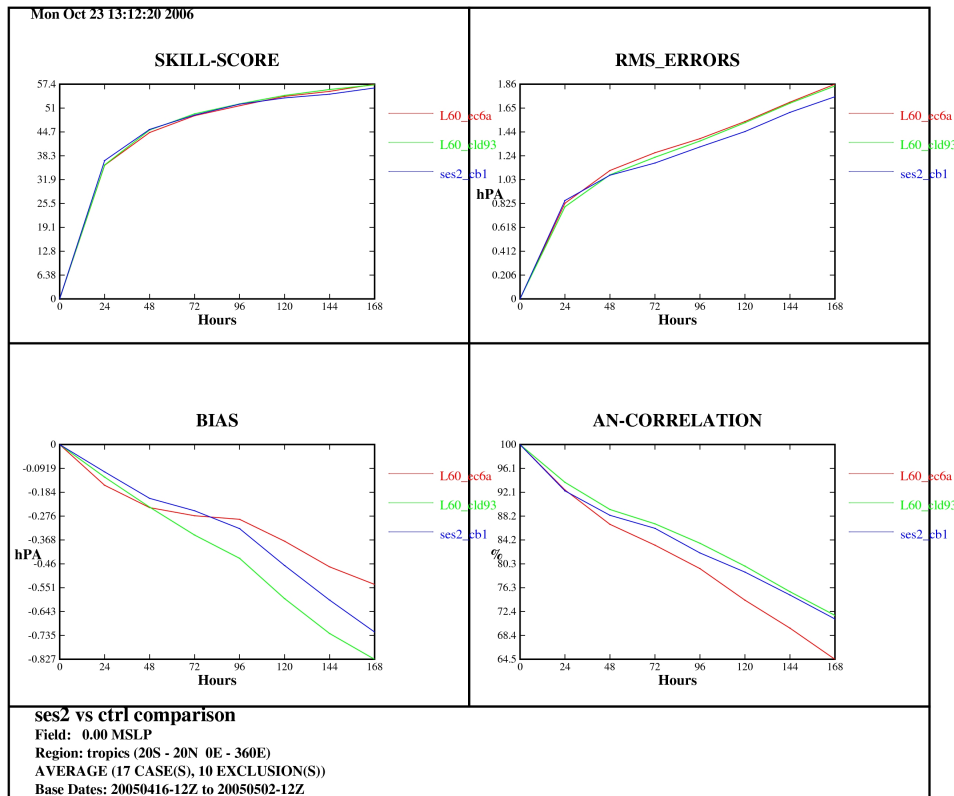


Figure 48. As for Figure 47, but for 850 hPa geopotential height of Southern Annulus.

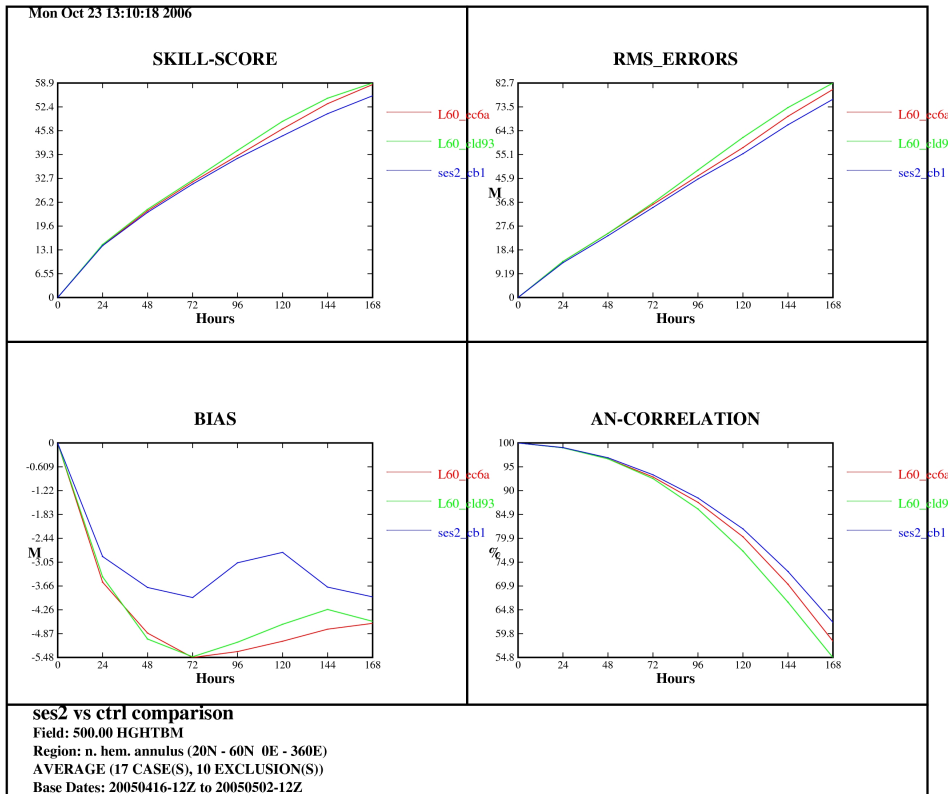


Figure 49. As for Figure 47 but for 500 hPa geopotential height of Northern Annulus.

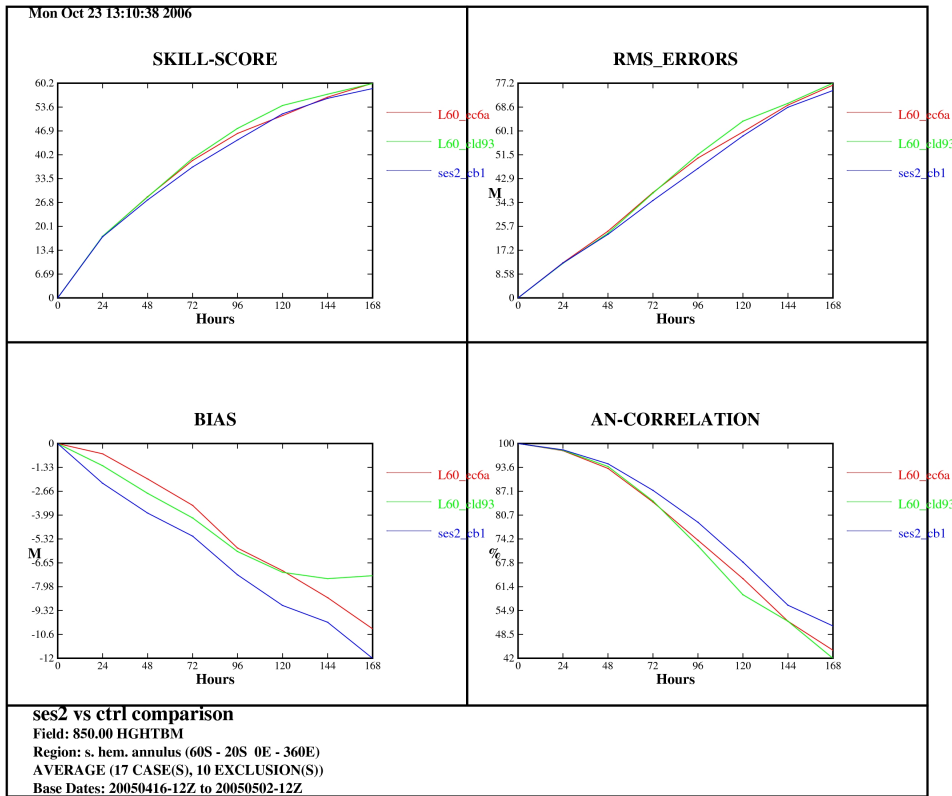


Figure 50. As Figure 47 but for 100 hPa geopotential height of Australia

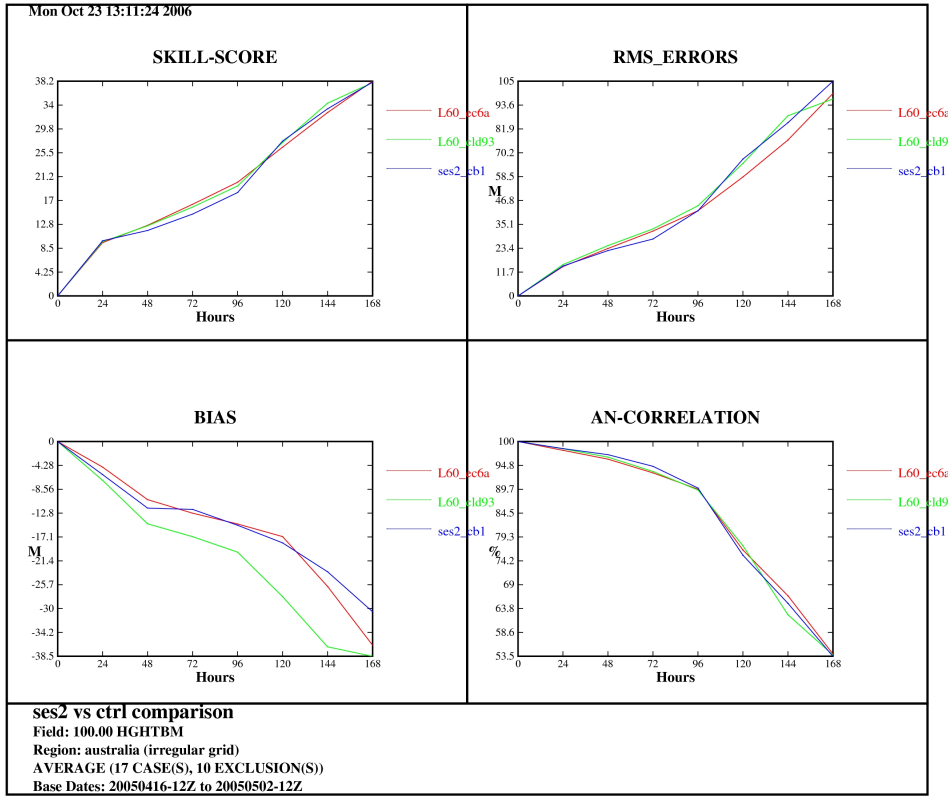
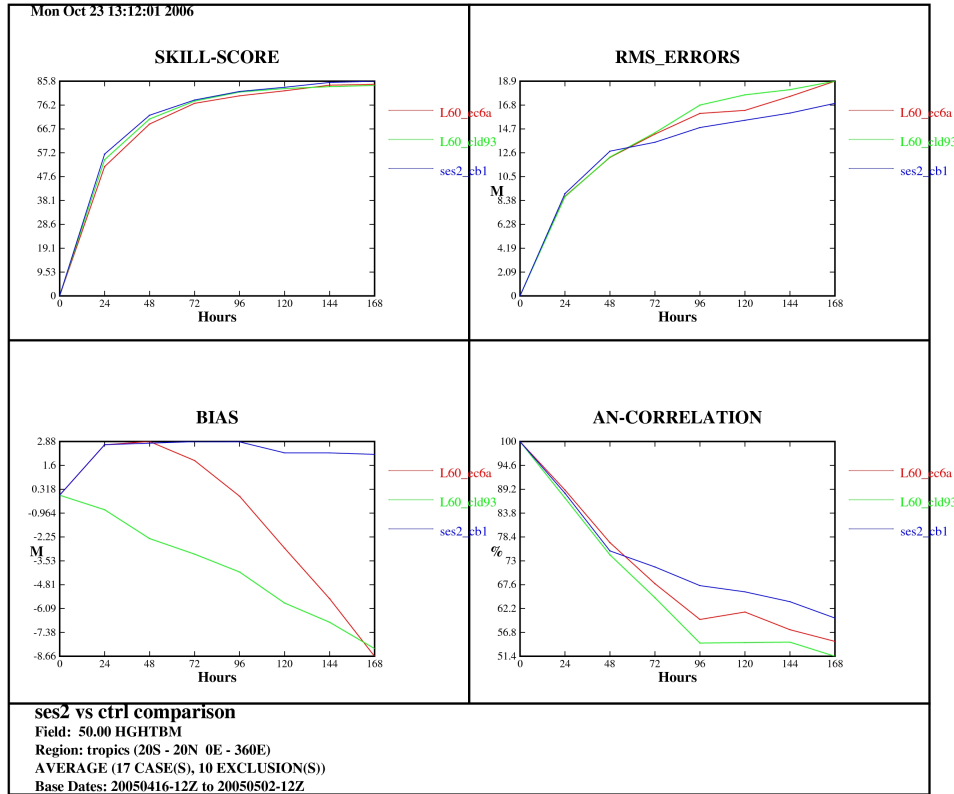


Figure 51. As for Figure 47 but for 50 hPa geopotential height of tropics



14. CONCLUSIONS

This report has documented development works relating to radiation carried out at BMRC. These include the modifications of Genln2 line-by-line radiation model, the development of SES2 radiation scheme and the development of fast surface radiation budget scheme. In line with these developments, a set of processing software has also been developed and become a useful tool for use in the future. The important outcome from the SES2 scheme is its capacity for most NWP and climate applications. This is particularly true for meeting with the requirement for the IPCC assessment. With the system as shown in Figure 3, implementing extra absorbing species to the SES2 in the future becomes a relatively easy task. The link between the SES2 and SURFLX schemes has extended the model validations to a wide range of atmospheric conditions. Such a validation is very important as it ensures that the models are accurate for general conditions that may occur in the atmosphere.

From the results presented in this report, the following conclusion marks can be drawn.

1. Compared with observations and other line-by-line radiation schemes, it has been shown that the modified Genln2 model is accurate and can be safely used as a tool and benchmark for development of broad-band radiation scheme. The model capability has been further strengthened with the implement of the new spectral absorption datasets.
2. A new correlated k-distribution method is developed for the SES2 radiation scheme. It has been shown that this method is successful in reduction of the computational cost while maintaining the calculation accuracy. Using this technique, the total number of monochromatic radiative transfer calculations in each radiation call in model integration is reduced from 121 required in Edwards-Slingo original scheme to 58 in the SES2.
3. SES2 has been tested against the Genln2 line-by-line and the flux bias is within 1 W m^{-2} at the surface and 2 W m^{-2} at the top of the atmosphere. The heating rate error is less than 0.5 k day^{-1} in troposphere and less than 2 k day^{-1} in stratosphere.
4. The global and net solar radiative fluxes determined using the SURFLX are compared with observations obtained from four different locations in the tropics, mid-latitudes, Arctic and Tibetan Plateau (results are not shown in this report). The mean relative errors of SURFLX scheme for these locations are between 4% and 8%. The agreement between the SURFLX and SES2 is excellent with bias being less than 0.5%. The accuracy of SURFLX indicates that it may be applicable to the SES2.
5. The SES2 is evaluated in BAM model in both climate and NWP modes. The model derived radiation fields at the TOA under clear sky condition are compared with CERES satellite observations. The results show that the modeled shortwave reflected radiation at the TOA is in a good agreement with the CERES observations. But discrepancies in OLR are found over the tropical convective zones. According to the early studies these discrepancies are likely due to the errors in the observations rather than in models. Further investigation may be needed to clarify this issue. Ten year climate integrations of AMIP experiment are performed and the results are compared with ERBE observations and NCEP reanalysis. Although there are many deficiencies in the model, the use of SES2 has shown some improvements in the cloud radiative forcing, precipitation and temperature fields compared with those determined using the early version of the model or using the old radiation scheme. One month assimilation and NWP forecasts were performed and the results were verified against analysis. It is seen that the use of SES2 has some positive impact on the forecast scores.

In general, the SES2 scheme can produce results compatible with observations and its performance in the BAM model is also encouraging. Unfortunately, the scheme was not used in the last version of GASP operational model because of the shift to work on the Australian Climate Community Earth Simulation System (ACCESS). Nevertheless, the results shown in this report are still useful document as the SES2 has been implemented in the ACCESS model and may be used as operational suite if it can lead to improvement in operational weather forecasts. The evaluation of the SES2 in the ACCESS is currently in the process.

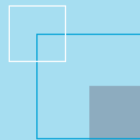
REFERENCES

- Chagas, J. C. S., D. A. Newnham, K. M. Smish, and K. P. Shine, 2002. Impact of new measurements of oxygen collision-induced absorption on estimates of short-wave atmospheric absorption. *Q. J. R. Meteorol. Soc.*, 128, 2377-2396.
- Chou, M., and K. Lee, Parameterizations for the absorption of solar radiation by water vapor and ozone, *J. Atm. Sci.*, 53, 1203-1208, 1996.
- Clough, S. A., Iacono, M. J. and Moncet, J. L. 1992. Line-by-line calculations of atmospheric fluxes and cooling rates: Application to water vapor. *J. Geophys. Res.*, **97**, 15761-15785.
- Collins, W. D., and A. K. Inamdar, 1995: Validation of clear-sky fluxes for tropical oceans from the Earth Radiation Budget Experiment. *J. Climate*, **8**, 569–578.
- Collins, W. D., V. Ramaswamy, M. D. Schwarzkopf, Y. Sun, R. W. Portmann, Q. Fu, S. E. B. Casanova, J-L. Dufresne, D. W. Fillmore, P. M. D. Forster, V. Y. Galin, L. K. Gohar, W. J. Ingram, D. P. Kratz, M.-P. Lefbvre, J. Li, P. Marquet, V. Oinas, Y. Tsushima, T. Uchiyama and W. Y. Zhong. Radiative forcing by well-mixed greenhouse gases: Estimates from climate models in the IPCC AR4. *J. Geophys. Res.* 111, D14317, doi:10.1029/2005JD006713.
- Colman, R., Deschamps, L., Naughton, M., Rikus, L., Sulaiman, A., Puri, K., Roff, G., Sun, Z., and Embery, G. 2005. BMRC Atmospheric Model (BAM) version 3.0: comparison with mean climatology. *BMRC Research Report No. 108, Bur. Met. Australia.*
- Cusack, S., J. M. Edwards, J. M. Crowther, 1999: Investigating k distribution methods for parameterizing gaseous absorption in the Hadley Centre Climate Model. *J. Geophys. Res.* 104, D2, 2051-2057.
- Edwards, D. P., GENLN2 A general line-by-line atmospheric transmittance and radiance model, *NCAR Tech. Note TN-367+STR*, Natl Cent. for Atmos. Res., Boulder, Colo., 1992.
- Edwards, J. M. and A. Slingo. Studies with a flexible new radiation code. I: Choosing a configuration for a large-scale model. *Quart. J. Roy. Meteor. Soc.*, 1996, 122 (531): 689-719.
- Goldman, A., Extended quantitative spectroscopy for analysis of atmospheric infrared spectra, Invited Letter, Fourier Transform Spectroscopy, *Opti. Soc. of Am.* --Tropical Meet., Santa Fe, N. M., 1997.
- Fu, Q., and K. N. Liou, On the correlated k -distribution method for radiative transfer in nonhomogeneous atmospheres, *J. Atmos. Sci.*, 49, 2139-2156, 1992.
- Goody, R. M. and Y. L. Yung, *Atmospheric Radiation: Theoretical Basis*, 2nd ed., 519 pp., Oxford Univ. Press, New York, 1989.

- Harrison, L., M. Beauharnois, J. Berndt, P. Kiedron, J. Michalsky, Q. Min, 1999. The Rotating Shadowband Spectroradiometer (RSS) at SGP, *Geophys. Res. Lett.* **26**, No 12, 1715-1718
- Labs, D., and H. Neckel, 1970. Transformation of the absolute solar radiation data into the international practical temperature scale of 1968, *Solar Phys.*, 15, 79-87.
- Lacis, A. A., and J. E. Hansen, 1974: A parametrization for the absorption of solar radiation in the Earth's atmosphere. *J. Atmos. Sci.*, 31, 118-133.
- Lacis, A.A., and V. Oinas, 1991: A description of the correlated k distributed method for modeling nongray gaseous absorption, thermal emission, and multiple scattering in vertically inhomogeneous atmospheres. *J. Geophys. Res.*, **96**, 9027-9063, doi:10.1029/90JD01945.
- Li, J. and H. W. Barker, 2005: A radiation algorithm with correlated k-distribution. Part I: local thermal equilibrium. *Journal of Atmospheric Science*, *Journal of Atmospheric Science*, 62, 286-309
- Liou, K.-N., 1980. *An Introduction to Atmospheric Radiation*. Int. Geophys. Ser., Academic Press, 392 pp.
- Kneizys, F. X., E. P. Shettle, L. W. Abreu, J. H. Chetwynd, G. P. Anderson, W. O. Gallery, J. E. A. Selby, and S. A. Clough, User's guide to LOWTRAN7, *AFGL Tech. Rep. AFGL-TR-88-0177*, Air Force Geophys. Lab., Bedford, Mass., 1988.
- Kurucz, R. L., 1992. Synthetic infrared spectra, *Infrared solar physics, IAU Syms.* 154, edited by D. M. Rabin and J. T. Jefferies, Kluwer, Acad., Norwell, Massachusetts.
- Malicet, J., D. Daumont, J. Charbonnier, and C. Parisse, 1995. Ozone UV spectroscopy. II. Absorption cross-sections and temperature dependence, *J. Atmos. Chem.*, 21, 263-273.
- Mlawer, E. J., Taubman, S. J., Brown, P. D., Iacono, M. J. and Clough, S. A. 1997. Radiative transfer for inhomogeneous atmospheres: RRTM, a validated correlated-*k* model for the longwave, *J. Geophys. Res.*, 102, 16,663-16,682.
- Mlawer, E. J., Clough, S. A., Brown, P. D., Stephen, T. M., Landry, J. C., Goldman, A., Murcary, F. J., 1998. Observed atmospheric collision-induced absorption in near-infrared oxygen bands. *J. Geophys. Res.* 103, 3859-3864, [10.1029/97JD03141](https://doi.org/10.1029/97JD03141)
- Mlawer, E. J., P. D. Brown, S. A. Clough, L. C. Harrison, J. J. Michalsky, P. W. Kiedron, and T. Shippert, 2000: Comparison of spectral direct and diffuse solar irradiance measurements and calculations for cloud-free conditions. *Geophys. Res. Lett.*, **27**, 2653-2656.
- Molina, L. T., and M. J. Molina, Absolute absorption cross section of ozone in the 185 to 350-nm wavelength range, *J. Geophys. Res.*, 91, 14501-14508, 1986.

- Neckel, H., and D. Labs, 1984, The Solar Radiation Between 3300 and 12500 A, *Solar Physics*, 90, 205-258.
- Newnham, D. A., and J. Ballard, 1998. Visible absorption cross-sections and integrated absorption intensities of molecular oxygen (O_2 and O_4), *J. Geophys. Res.*, 103, 28,801-28,816.
- Orphal, J., 2002. A critical review of the absorption cross-sections of O_3 and NO_2 in the 240-790 nm region, *ESA Technical Note MO-TN-ESA-GO-0302*, CNRS, Orsay, France
- Ramaswamy, V. and S. M. Freidenreich, Solar radiative line-by-line determination of water vapour absorption and water cloud extinction in inhomogeneous atmosphere, *J. Geophys. Res.*, 96, 9133-9157, 1991.
- Rothman L. S., A. Barbe, D. Chris Benner, L.R. Brown, C. Camy-Peyret, M.R. Carleer K. Chance, C. Clerbaux, V. Dana, V.M. Devi, A. Fayt, J.-M. Flaud, R.R. Gamache, A. Goldman, D. Jacquemart, K.W. Jucks, W.J. Lafferty, J.-Y. Mandin, S.T. Massie, V. Nemtchinov, D.A. Newnham, A. Perrin, C.P. Rinsland, J. Schroeder, K.M. Smith, M.A.H. Smith, K. Tang, R.A. Toth, J. Vander Auwera, P. Varanasi, K. Yoshino. 2003: The HITRAN molecular spectroscopic database: edition of 2000 including updates through 2001. *JQSRT*, 82, 5-44.
- Rotstajn, L., 1997: A physical based scheme for the treatment of stratiform clouds and precipitation in large-scale models. I: Description and evaluation of the microphysical processes, *Q. J. R. Meteorol. Soc.*, 123, 1227-1282.
- Schwarzkopf, M. D. and S. B. Fels, 1991: The simplified exchange method revisited: An accurate, rapid method for computation of infrared cooling rates and fluxes. *J. Geophys. Res.*, Vol. 96, 9075-9096.
- Slingo, A. and Schrecker, H. M. 1982. On the shortwave radiative properties of stratiform water clouds. *Q. J. R. Meteorol. Soc.*, 108, 407-426.
- Slingo, A., Pamment, J. A. And Webb, M. J. 1998. A 15-year Simulation of the Clear-Sky Greenhouse Effect Using the ECMWF Reanalyses: Fluxes and Comparisons with ERBE. *J. Climate*, 11, 690-708.
- Smith, K.M. and Newnham D.A., 2000. Near infrared absorption cross-sections and integrated absorptions of molecular oxygen (O_2 , O_2-O_2 , and O_2-N_2), *JGR*, 105, 7383-7396.
- Stokes, G.M., and S.E. Schwartz, 1994: The Atmospheric Radiation Measurement (ARM) Program: Programmatic background and design of the cloud and Radiation Testbed. *Bull. Amer. Meteor. Soc.*, 75, 1201-1221.
- Sun, Z. and Rikus, L., 2004: Validating model clouds and their optical properties using Geostationary satellite imagery. *Monthly Weather Review* 132 (8), 2006-2020.
- Sun, Z. and Rikus, L. 1999. Improved application of exponential sum fitting transmissions to inhomogeneous atmosphere. *J. Geophys. Res.*, 104, 6291-6304.

- Sun Z., Li Yunyan, Zeng Xianing, Luo Zhexian, Wu Jingang and Liu Jingmiao, 2007: Parameterization of solar radiation at the surface under cloudless conditions and its validation against observations. *Aust. Met. Mag.* 56, 81-92
- Voigt, S., Orphal, J., Bogumil, K. and Burrows, J. P. 2001. The temperature dependence (203-293 K) of the absorption cross-sections of O₃ in the 230-850 nm region measured by fourier-transform spectroscopy, *J. Photochem. Photobiol.*, A143, 1-9.
- Xie, P. and Arkin, P. A. 1996. Analysis of global monthly precipitation using gauge observations, satellites, and numerical model predictions. *J. Climate*, 9, 840-858.
- Zhang, H., and G. Y. Shi, 2005: A new approach to solve correlated *k*-distribution function, *Journal of Quantitative Spectroscopy & Radiative Transfer*, Vol. 96(2), 311-324.



The Centre for Australian Weather and
Climate Research is a partnership between
CSIRO and the Bureau of Meteorology.